

INFRARED ASTRONOMICAL INSTRUMENTATION AND POLARISATION STUDIES

A thesis submitted in partial fulfillment of the requirements
of the degree of

Doctor of Philosophy

by

ARCHITA RAI

(Roll No. 15330006)

Under the guidance of

DR. SHASHIKIRAN GANESH

Astronomy & Astrophysics Division

Physical Research Laboratory, Ahmedabad, India



Department of Physics

INDIAN INSTITUTE OF TECHNOLOGY GANDHINAGAR

2020

Dedicated to my beloved parents & didu

Declaration

I, Archita Rai, declare that this written submission represents my ideas in my own words and where others ideas or words have been included, I have adequately cited and referenced the original sources. I also declare that I have adhered to all principles of academic honesty and integrity and have not misrepresented or fabricated or falsified any idea/data/fact/source in my submission. I understand that any violation of the above can cause disciplinary action by the Institute and can also evoke penal action from the sources which have thus not been properly cited or from whom proper permission has not been taken when needed.

Archita Rai
(Roll. No. 15330006)

Date: 17/08/2020

Certificate

It is certified that the work contained in the thesis entitled Infrared Astronomical Instrumentation and Polarisation Studies by Ms. Archita Rai (Roll no 15330006), has been carried out under my supervision and that this work has not been submitted elsewhere for any degree or diploma.

(Shashikiran Ganesh)
Thesis Supervisor
Associate Professor
Astronomy & Astrophysics Division
Physical Research Laboratory
Unit of Department of Space, Govt. of India
Ahmedabad-380009, Gujarat, India.

Date: 17/08/2020

Acknowledgement

PhD is a journey - as frustrating & as rewarding at the same time!

A journey to self-fulfilment!

The 5 years spent during the course of my study had seen 10 batches going & coming before my eyes. A lot of experiences have been gained, personally & professionally witnessing the good and bad times. We grow as we learn from each other. Each PhD story has something unique to say, and here I gather all my memories together to thank all the people who have consciously or unconsciously been part of this exciting part of my life.

The foremost person to express my heartfelt thanks is my PhD supervisor, *Dr. Shashikiran Ganesh*. You have always been an ocean of patience and calmness for all of my naive activities and questions. I have been enchanted by your knowledge of the night sky and the 3D visualizations of the galaxy structure. The observational trip to Mt. Abu wouldn't have been so exciting and insightful, if you weren't there to instill within me all the knowledge of stars seen in the night sky. The love for watching night sky got deepened after meeting you and understanding more about its richness. I will also always remember the instrument fixing times, when we make multiple rounds at the telescope floor in the chilling weather. The most amazing memories being when you would come from the catwalk of the observatory & ask us - the 'half sleepy observers' to go out in the chill weather and witness something very interesting in the night sky. It did work to make us open-eyed and uptight for full night. The list is long to thank you for your continuous words of wisdom which have really kept me motivated for the years. I have learned a lot from you as a person & an academician, and will always try to instill those qualities within me. Apart from being my supervisor, you encouraged me to start my *Sitar* learning, and we joined together as students. Those times will always be a very special part of my life.

A very important mention to whom I owe my greatest of thanks is *Prof. K S Baliyan*. You have been a very dynamic leader who always kept the tribe (astronomy division) together. I have expressed my doubtful times in front of you, and couldn't argue more

to have got the best of advise from you. I have always seen you very active and supportive in all student matters. Being one of my DSC members, you have always given very apt suggestions for the work which made it more better. You are one of the most admirable person in my life. I had fun moments with your family, and the interaction with *Mam* has been full of happy story times. She had always been thoughtful for our well-being and it felt home to be around your family. I am also thankful to *A B Shah Sir* for his motivations and support towards me during my work. I am very thankful to *Mr. Sukamal Paul*, who have always helped me in my optical design work and managed to take time out of his very busy schedules. It means a lot to me.

I express my heartfelt gratitude to my 2nd DSc member, *Prof. Santosh Vadawale*. Your suggestions for my academic work has always been very fruitful and I have learnt a lot from them. I also express my big thankyou to the anonymous referees of the thesis, whose critical technical comments made me to appreciate the work more, and enhance my own knowledge. Thankyou to *Prof A N Ramaprakash* for reviewing my thesis with so much patience. I literally got overwhelmed with it, and a lot is to be learned from a mentor like you. I thank the current Chairman of Astronomy & Astrophysics division, *Prof. Abhjit Chakraborty* for his support towards the requirements of my research work. I am thankful to my course work project supervisor, *Dr. Mudit Srivastava* for his amazing way of teaching and explaining any difficult problem with simplicity. I also express my heartfelt thanks to another project supervisor, *Prof. Nandita Srivastava* for making me understand in detail the work I completed as my project, and been always present to clarify my doubts. I take this opportunity to thank all the faculty members & the technical staff of the Astronomy & Astrophysics division for their suggestions in the discussions during area seminars and at other platforms. I express my heartfelt thanks to the Mt. Abu observatory technical staff with special mention to *Rajesh Sir, Mathur Sir, Jain Sir*, canteen staff & the night assistants and TOTs, especially *Prashant & Mukesh* for their immense help during observation times. It was because of them that all the observations through the 1.2 m telescope have been taken smoothly. I am grateful to the current PRL Director, *Prof. Anil Bharadwaj* for his timely support and guidance in all matters regarding to my international travel & approval to hold a student conference at PRL. I also thank the former Directors at PRL *Prof. Utpal Sarkar & Shri Tapan Mishra* for their support to students and lending a helpful hand towards us during our research

work. I thank the former Dean, PRL, *Prof. Janardhan* for his support in academic matters during my PhD tenure & the current Dean, PRL, *Prof. D. Pallamraju* for thinking of the well-being of students while heading an authority position. I also thank the former Academic committee Chairman, *Prof. S Ramachandran*, current Academic committee chairman *Dr. B. K. Sahoo* & all the members of the Academic committee for doing the thankless job of reviewing our work with patience and providing us with ideas to improve the research work. I thank the head, Academic Services, PRL, *Dr. Bhushit* to manage our academic activities.

I get overwhelmed with the love and care of *Abirami Mam* towards me. A strong bond has been made in a span of 4 years, which will only get more stronger. My best wishes to *Gayatri* for her future endeavors, and I will always remember the fun we have had during the visits to Sir's place. The *Kids Day Out* time will be most cherishable. Times spend were always homely times. I want to thank few of the other faculties at PRL, *Dr. G. K. Samanta*, *Dr. Arvind Singh*, *Dr. Rajesh Kushwaha*, *Dr. Vineet Goswami* who have always welcomed us with joy and provided us with a homely environment in the midst of research work. The interactive time spent with your families has been a mood changer.

I express my heartfelt gratitude to *Richa Mam* for her out of the way support for us in times of need. I thank the Registrar office, PRL administration, accounts, transport & canteen staff at PRL for always been present to fulfil our requirements. I thank the Computer center, PRL for their timely help regarding any software or wifi issues and providing smooth internet access during my PhD time. I also express my thankfulness to *Nishtha Mam*, *Dr. Md Nurud Alam*, *Dr. Pragya* & other library staff and trainees at PRL for their assistance related to book grant and keeping us up to date with the new publishings, and also organising book fairs & managing subscriptions of all research scholar friendly journals and tools. I thank the house keeping staff at Thaltej for their untiring hospitality to us, and I express my deep gratitude to them.

Life in PRL has been so lively with the friendships made during the stay here. The person who has been the best of friends here, with whom I can share my food love, my unending stories, my philosophies towards life, my hangouts, my sadness etc is *Subir*. I will always cherish the times we have spent at PRL hostel and we waiting

to finish office hours and talk endlessly about our day. Another very special & dear friend to me, *Aarthy*, has been witness to all my crazy mind ideas and we have spent times as - late night deep chats, travel times to conferences and exploring the hotels and having full fun could never get drained out of my memory tank. We three have had multiple moments together and hope to make more in the years to come. I will always be happy to join in the Batch of 2015 which consists of the most zealous minds - *Shefali, Nidhi, Akanksha, Shivangi, Richa, Kaustav, Rahul, Varun, Ranadeep, Raju, Ashish, Harsh Oza, Harsh Raj, Balbeer, Naman, Arvind, Siddharth, Ritika & Prashant bhaiya*. Be it the crazy *dumb charades* moments with them at Udaipur, to sleepy lazy morning vibes with a few in the canteen, to dance parties, to *antakshari* at terrace; we have spend the best moments together with *fighting with each other* to *fighting for each other* transitions.

The seniors I met at the PRL Thaltej hostel, have made a deep place in my heart and have induced a lot of positives i.e a sense of responsibility, creativity, drama, holding student conferences etc. The night long chats at *Thinking tree* with *Priyanka di, Shweta di, Arko bhaiya, Tanmay bhaiya, Gaurava bhaiya, Deepak bhaiya* has been the memorable times. The times spent at *Shweta di* house has been an escape from the tight research schedules to get indulged in some constructive cooking & fun talks. The other seniors with whom I have made a lasting bond and will always be thankful are *Ikshu di, Bivin bhaiya, Kuldeep bhaiya, Prahlad bhaiya, Jabir bhaiya, Satish bhaiya, Rukmani di, Rupa di, Ali bhaiya, Subhanand Anna, Dipti bhaiya, Monojit bhaiya, Nijil, Vishnu, Niharika di*.

I express my deepest and warmest love to my two senior office colleagues and friends, *Navpreet di & Kumar bhaiya*. They have been there when I joined the group, and their constant support has helped me grow at different phases & stages of PhD life. The office sharing with *Navpreet di* and her warm and jolly nature led me to spend one of the best times in office with several memorable moments. You have been a soulful person and having deep life discussions with you were very good. I will always remember the *musical times* spend in the office with both of you. I also thank my new office colleague *Aravind* and junior in the group who became friend with me in no time, after his joining the group. I am thankful to you to always have been there for me at any time, and maintaining the joyful atmosphere of the office with your sense of humour. I will always treasure those times. I thank another junior addition to the group *Namita*, whose cute bubbly nature always adds charm to the place. Also , the interactions with the other

office group consisting of *Deekshya, Prashanth, Alka, Prachi, Prithish bhaiya, Devendra bhaiya, Janaka & Patwal Sir* has been full of encouragement and I extend my gratitude to them with full heart. I thank *Sandeep Kumar Rout* for the interactive talks we always had. We have some very great moments to cherish. I also remember *Somdutta*, and am grateful to her for her support & expressing a calm, jolly nature to fix up things. I thank all the other juniors in the Astronomy division - *Vipin, Neeraj, Sushant, Biswajit, Shawnlee, Abhay, Naval, Akanksha & Abhijit* for their encouragement during the course of my research. I extend my warm thanks to *Vaibhav bhaiya* for being there for any of my Zemax related doubts and helping me with full sincerity. I can't forget to thank the amazing juniors at the hostel, with whom jelling up and becoming friends had been one of the best times in PRL hostel. The chats we had on weekends, or during night walks and other times count substantially in my life. I want to mention to all of you - *Harish, Priyank, Abdur, Deepika, Nisha, Sushree, Surendra, Shivani, Anshika, Rituparna, Sana, Alka, Hrushikesh, Madhu, Ankit, Satyajeet, Yash, Pranav, Monika, Meghna, Tanya* my heartfelt gratitudes for being so good always.

The journey of PhD was possible due to the experiences gained in the previous times, as I take this opportunity to thank all of my friends who have made a great contribution in my life and because of whom the hardest of the times had silver lining. I want to thank the friends whom I met at the most innocent age and had the first hostel experience, *Suchana, Nikita, Anshul, Ruhi, Ipshita, Richa, Garima & Shyamalima*. I have always carried your memories at all the places I went and those memories had lit up my days. I also thank *Hreedish* for being a wonderful friend. I also want to thank few special people I have met in those times, *Amit bhaiya, Sunny bhaiya & Timakshi di*, who have always cared for me personally and taken full interest in my academic activities. You have been the best seniors anyone could get. I want to thank my other set of best people whom I met at BHU, and became best of friends for life - *Rajnish, Sudhir, Avinash, Abhay, Anupam, Pragati & Suman*.

I wish to thank a very special person to me *Gaurav*, whose constant support as a friend & as a mentor, has been there for me. A thank you shall be less to reward all the times you have been there for me and will still be. I have learnt a lot from you, and thank you

for keeping patience with me. I am overwhelmed to have the love from your family, and the care towards me during my stay in BHU and afterwards. I also thank, one of my teacher from BHU, who have guided and encouraged me to join Astronomy in my M.Sc days *Prof. Abhay Kumar Singh*. Your motivation has always brought the best in me and I am grateful to you for it, Sir.

Family is the most supportive of all, and seldom the least thanked one. I know expressing my gratitude will go on an endless list, because its long and probably so heartfelt that thanks won't do justice. I still express my sincere, loving, heartfelt, soulful thanks to my parents for giving me an education that I could always break the bounds to reach for higher. Nothing would have been possible without your constant hand on my head. I am indebted for all the sacrifices made for me. I am luckiest sister to have my elder sister always by my side in all moments of fun or grief. *Didi*, you have been the idol for me throughout my school to college and will continue to be so. I have learnt the best of things in life because of you being my coolest teacher. I love you from the bottom of my heart. I also am very grateful to have the best family, relatives and close cousins whose presence in my life makes it complete & worth living.

The thesis expresses its gratitude to all the teachers, mentors I have met throughout my journey of life and whose contributions lead to the completion of this most rewarding degree!

Abstract

The spectacular night sky with its vibrant stars is our own Milky Way Galaxy. The observations for the Galaxy dates back to the time when Galileo first used a telescope (1608-10) to observe the night sky. His conclusion was that the Milky Way is a vast collection of stars. Subsequently, many astronomers have worked extensively to bring up our current understanding of the Milky Way as a spiral galaxy.

Polarisation has been seen in the light from the stars in the Galaxy - particularly those close to the plane. Stars, being spherically symmetric, one does not expect the light to be polarised and certainly not in a coordinated (aligned) manner, hence it was realized that this was due to the medium through which the light had travelled. This was the discovery of interstellar polarisation. The current understanding is that the asymmetric dust grains in the interstellar medium get aligned in the Galactic magnetic field giving rise to interstellar polarisation. Hence, measurement of polarisation is a way to measure the Galactic magnetic field - both strength and direction, in some conditions.

The inner regions of the galaxy have always been obscured from our view at optical wavelengths, because of the intervening clouds of dust. Therefore, our knowledge of the Milky Way structure and how the different components have been formed and put together can only be enhanced by surveying the galaxy at near and mid-infrared wavelengths. But most of these large scale surveys, until recently, were confined to imaging and spectroscopic studies, leaving behind the polarimetric observations which demands a thorough study in the regions of heavy dust presence. By studying the polarization distribution, one can get additional information about the magnetic field (its geometry & strength) and study the dust present in the region. One expects that there should be a correspondence of the distribution of molecular clouds in different

directions with the distribution of dust (which causes extinction and polarization). A polarimetric instrument in the near infrared is therefore a very valuable means to study the polarization distribution along the line of sight (in combination with distance determined using different techniques - e.g. red clump method, parallax etc).

The science part of the thesis has addressed the interstellar polarisation phenomena using the PRL 1.2 m telescope with the NICSPol instrument. The observations of a dark Lynds cloud L1340 have been undertaken and polarisation measurements for stars part of the cloud have been reported in the J, H & K_s bands. The plane of the sky magnetic field strength has also been estimated for the RNO 8 cluster and cloud core, which is a part of the L1340 cloud. The observations were taken using a wire-grid module (WGP) as analyzer on the near-IR camera & spectrograph (NICS) instrument. This work underlines a very promising scientific approach and impresses on the need for a more versatile instrument with improved accuracy in polarisation measurements, and negligible thermal contribution from the optics. This is one of the major scientific goals which led us to develop NISP (Near-IR Imager, Spectrometer & Polarimeter) as a new multi-function near-infrared instrument for PRL's upcoming 2.5 m telescope at Mount Abu.

The major part of the thesis covers the instrumentation part and includes the optical design of NISP which has been completed with optimization of the design at each step. The instrument offers multimode capabilities of imaging, spectroscopy and polarimetry in a single package. The different modes in the instrument have been realised using components whose designs were custom made to achieve the specifications required in the instrument. Several options were explored with the manufacturers since the components would be fabricated at room temperature but used at cryo temperatures at NIR wavelength ($0.9 \mu m - 2.5 \mu m$). This posed various challenges and constraints. With several constraints of meeting instrument specifications, instrument size limit, performance at cryo temperature etc., the optical design had been completed. The collimator optics design is a F/8 system with a collimated beam width of 38 mm, and the camera design necessary for our instrument specifications is F/5. The design has achieved a full unvignetted imaging field of view of $10' \times 10'$, and a spectral resolving power ~ 2150

across all filters in the near-infrared. It implements single shot imaging polarimetry using wedged double Wollaston as an analyser. The dual beam polarimetry technique, will benefit many scientific projects with an improved precision in the observational data. The dual beam method helps in using the full light, by not wasting half of the orthogonal component of polarization. This also cancels the Earth atmosphere effects by the ratio of intensities taken amongst orthogonal components. Hence, this allows the observers to work on targets with low polarisation or sources with intrinsically variable polarisation behaviour on short time scales. Some example science programs are: polarisation study of the interstellar regions of the Milky Way, mainly involving polarisation study of larger molecular clouds, clusters, globules etc. & variability of AGN polarisation on short timescales, wherein polarisation variability has been noticed on short timescales (order of a few minutes) which need a simultaneous measurement mode, to obtain better polarisation accuracy. These will be addressed once the instrument is commissioned.

The thesis work illustrates the intricate details of the optical design of a near infrared multimode instrument and its fulfilment with robust attributes, in terms of the implementation of the various modules, in the NISP instrument for PRL's upcoming 2.5 m telescope.

Keywords : Optical design, multi-function infrared instrumentation, dual beam polarimetry, Interstellar polarisation, ISM, Lynds clouds

List of Publications

Thesis Related

1. **Rai A.**, Ganesh S., Paul S. K., Kasarla P. K., Prajapati P. V., Sarkar D. R., Singh A., et al., "Optical aspects of Near-Infrared Imager Spectrometer and Polarimeter instrument (NISP)", 2020, SPIE, 11447, 1144765. [doi:10.1117/12.2560988](https://doi.org/10.1117/12.2560988)
2. Kasarla P. K., Patwal P. S., Adalja H. K. L., Mathur S. N., Sarkar D. R., Singh A., **Rai A.**, et al., "Mechanical aspects of near infrared imager spectrometer and polarimeter", 2020, SPIE, 11447, 114476U. [doi:10.1117/12.2561339](https://doi.org/10.1117/12.2561339)

Contributory

1. Esakkiappan Aarthy, **Archita Rai**, Shashikiran Ganesh, Santosh Vadawale, "NIC-SPol : a near infrared polarimeter for the 1.2-m telescope at Mount Abu Infrared observatory", 2019, JATIS, Vol.5, Issue 3, <http://doi.org/10.1117/1.JATIS.5.3.035006>
2. Kumar Venkataramani, Shashikiran Ganesh, **Archita Rai**, Marek Husarik, K.S. Baliyan, U.C. Joshi, "Time and Phase resolved optical spectra of the potentially hazardous Near Earth Asteroid 2014 JO25", 2019, AJ, Vol 157, No.5, <https://doi.org/10.3847/1538-3881/ab0f26>
3. Ganesh S., **Rai A.**, Aravind K., Singh A., Prajapati P. V., Mishra A., Kasarla P., et al., "EMPOL: an EMCCD based optical imaging polarimeter", 2020, SPIE, 11447, 114479E., [doi:10.1117/12.2560949](https://doi.org/10.1117/12.2560949)
4. Roy Sarkar D., Shah A. B., Singh A., Patwal P. S., Kasarla P. K., **Rai A.**, Prajapati P. V., et al., "Electronics design and development of near-infrared imager, spectrometer,

and polarimeter", 2020, SPIE, 11447, 1144778, [doi:10.1117/12.2562113](https://doi.org/10.1117/12.2562113)

5. Shashikiran Ganesh, Aravind Krishnakumar, Kumar Venkataramani, **Archita Rai**, Kiran S Baliyan, Umesh Chandra Joshi, "Solar system studies with the Indo-Belgian telescopes", Bulletin de la Société Royale des Sciences de Liège [En ligne], Volume 88 - Année 2019, Actes de colloques, 2nd Belgo-Indian Network for Astronomy & Astrophysics (BINA) workshop - October 2018 - Brussels, Belgium, 65-69, <https://popups.uliege.be:443/0037-9565/index.php?id=8669>

Under Preparation

1. **Archita Rai**, Shashikiran Ganesh, "Infrared Polarisation Study of Lynds 1340: case of RNO 8", *To be re-submitted after addressing referee comments.*
2. **Archita Rai**, Shashikiran Ganesh, Sukamal Paul, "Imaging Design of NISP : A Near-IR Imager Spectrometer & Polarimeter" (*Under preparation for submission to Experimental Astronomy*).
3. **Archita Rai**, Shashikiran Ganesh, "Polarisation Design of NISP using a single shot device" (*Under preparation*).
4. **Archita Rai**, Shashikiran Ganesh, "Spectroscopic Design of NISP" (*Under preparation*).

Oral Presentations

Area Seminars

1. **Division Seminar**, entitled " Bayesian Inference : An approach in Astronomy", during February 2017, Astronomy & Astrophysics Division, Physical Research Laboratory, Ahmedabad, India.
2. **Division Seminar**, entitled "An Infrared study of Dark Cloud: LDN1340", during August 2018, Astronomy & Astrophysics Division, Physical Research Laboratory, Ahmedabad, India.
3. **Division Seminar**, entitled "Interstellar Polarisation: Grain alignment theories & polarisation study towards high opacity LDN clouds", on 25th July 2019, As-

tronomy & Astrophysics Division, Physical Research Laboratory, Ahmedabad, India.

4. **Division Seminar**, entitled "Optical Design of NISP : A Near-Infrared Imager, Spectrometer & Polarimeter", on 21st July 2020, Astronomy & Astrophysics Division, Physical Research Laboratory, Ahmedabad, India.

Other talks

1. **Conference talk**, on the topic "Near-Infrared Imaging Spectro-Polarimeter (NISP) instrument for PRL 2.5-m telescope", Astronomical Society of India conference, Hyderabad, India, February 5-9, 2018.
2. **Conference talk**, entitled "Polarization study of Lynds' Dark Nebulae", International Conference on Infrared Astronomy & Astrophysical Dust, held at IUCAA, Pune, India, October 22-25, 2019.

International Workshops/Conferences

1. **NARIT, Thailand** : I attended the "Optical Design Summer School", organised by NARIT, Chiang Mai, Thailand during July 31 - August 5, 2017.
2. **Asiago, Italy**: I attended a summer school "Looking at Cosmic Sources in Polarized Light", organised by University of Padova, Italy during June 18-26, 2018.
3. **Heidelberg, Germany**: I attended a summer school titled 'Instrumentation for ground based optical & infrared astronomy' organised by Max Planck Institute for Astronomy, Heidelberg, Germany during September 9-13, 2019.
4. **SPIE** : I attended the SPIE Astronomical Telescopes + Instrumentation conference held in 2020, online mode. I had presented a poster on the title "Optical aspects of Near-Infrared Imager Spectrometer and Polarimeter instrument (NISP)" in the *Ground based and Airborne Instrumentation for astronomy VIII*.

National Conferences

1. **IUCAA, Pune** : I got a chance to attend as an invited participant, an International Conference on the topic “Infrared Astronomy & Astrophysical Dust”, organised by IUCAA, Pune, India during October 22-25, 2019.
2. **IUCAA, Pune** : I attended a school on Computational Statistics & Astrostatistics, January 2-10, 2017.
3. **Jaipur** : I attended the annual meeting of the Astronomical Society of India held at Jaipur in 2017.
4. **Osmania University** : I attended the annual meeting of the Astronomical Society of India organized by Osmania university at Hyderabad in 2018.

Convener : Young Astronomers’ Meet 2018

A national level student conference “Young Astronomers’ Meet” was organised at Physical Research Laboratory during September 24-28, 2018. I had the pleasure to be the convener for this event, coordinated by the students and for the students. The meeting had seen a participation of 60 PhD scholars in astronomy from institutes and universities all over India. The funding support was received from PRL & Infosys foundation grant of Prof A N Ramaprakash of IUCAA, India. Organizing this event gave me an exposure to the administrative and managerial challenges in conducting such a large scale academic event.

Contents

Acknowledgment

Abstract	i
List of Publications	v
List of Tables	xiii
List of Figures	xv
1 Introduction	1
1.1 Interstellar polarization	4
1.1.1 Relation between extinction & interstellar polarization	4
1.1.2 Polarisation & wavelength dependance	7
1.1.3 Grain alignment & magnetic field	8
1.2 Aspects of polarization measurements	10
1.3 Polarimetry of dark Lynds clouds	12
1.4 Multi-mode infrared instruments	13
1.5 Motivation	15
1.6 Research objectives	17
1.7 Thesis outline	18
2 Infrared Polarisation study of Lynds 1340	21
2.1 Observations	22
2.1.1 Telescope and instrument	22
2.1.2 Observational procedure	23
2.2 Data reduction and analysis	23

2.2.1	Polarisation calculation	24
2.2.2	Polarisation calibration	26
2.2.3	IR polarization values and large errors	26
2.3	Supplementary Data	27
2.3.1	2MASS & GAIA	27
2.3.2	WISE data	28
2.4	Results & Discussion	29
2.4.1	Color & distance information	33
2.4.2	NIR polarimetry	34
2.4.3	The RNO 8 cloud core	36
2.5	Conclusions	43
Appendix 2.A	Error propagation of P & θ	55
2.A.1	σ_P	55
2.A.2	σ_θ	56
3	Instrument Design	57
3.1	Zemax - Introduction	59
3.2	Preliminary study based on existing instrument designs	60
3.2.1	NICS & MIMIR	60
3.2.2	NICSPol & its simulation	61
3.3	Alternative conceptual layout plans for NISP	67
3.4	Design Parameters	70
3.4.1	Lens material selection	70
3.4.2	Lens splitting	73
3.4.3	Optimization of design parameters	74
3.5	Design Structural Flow	80
3.6	Summary	83
4	Imaging Optics	85
4.1	Overview of the imaging optics	85
4.2	Collimator Optics	87
4.3	Stops & Pupils : Placement of Filter Wheels	91
4.4	Camera Optics	92

4.4.1	Cryostat Window	94
4.4.2	Imaging layout	95
4.5	Analysis of Imaging Optics	95
4.5.1	Spot diagram	96
4.5.2	Diffraction Encircled Energy	100
4.5.3	Effect of vignetting	100
4.5.4	Modulation transfer function (MTF)	102
4.5.5	Wavefront Map	104
4.5.6	Aberrations	105
4.5.7	Image Simulation	107
4.6	Limiting magnitudes from NISP	108
4.6.1	AR coatings	108
4.7	Thermal Analysis	109
4.8	Tolerancing	110
4.9	Stray light analysis	112
4.10	Summary	113
5	Spectroscopic Optics	115
5.1	Calculations of Grism parameters	116
5.1.1	Choice of Order	119
5.1.2	Blaze function & efficiency	121
5.1.3	NISP grism specifications	122
5.2	Grism design & analysis	122
5.2.1	Low resolution grism	124
5.2.2	Intermediate resolution grism	126
5.2.3	Spot diagram	126
5.2.4	Diffraction encircled energy	127
5.3	Summary	128
6	Polarisation Optics	131
6.1	Algebra of Polarisation	132
6.2	Choice of polarization optics & trade-offs	132
6.2.1	Dichroic Polarizers	133

6.2.2	Birefringent Polarizers	134
6.3	Wedged Double Wollaston (WeDoWo)	136
6.3.1	Design of a WeDoWo	137
6.3.2	Design of WeDoWo for NISP	140
6.4	Polarimetric Analysis	145
6.4.1	Design of Polarisation optics	145
6.4.2	Focal plane mask	146
6.4.3	Image plane	146
6.4.4	Spot diagram	147
6.4.5	Polarization pupil map	150
6.5	Statistics of polarization measurements	150
6.6	Summary	153
7	Summary & Future Work	155
7.1	Summary	155
7.2	Future work	157
	References	159

List of Tables

2.1	Observational results for the polarized standard stars. The standard value for p & θ are taken from NOT & UKIRT links. The observed values are listed as p_{obs} & θ_{obs} . The offset for position angles is given by θ_{off} .	24
2.2	NICSPol linear polarization measurements of the 17 stars detected in all three J, H, K _s band (p_J, p_H, p_{K_s}) & polarization position angle (θ). The JHK magnitudes and distances to individual stars from 2MASS & Gaia survey data are compiled together.	31
2.3	NICSPol linear polarization measurements (p_J, p_H, p_{K_s}) & polarization position angle (θ) of the RNO 8 stars. The JHK magnitudes and distances to individual stars from 2MASS & Gaia survey data are also included. The central star of RNO 8 (see section 2.4.3.3 for discussion) is shown in bold in this table.	32
2.4	The mean values of degree of polarization (P) & position angle (PA) for the measurements of all stars in J, H, K _s filter bands in the region of L1340.	42
2.5	Estimated values of linear polarization for 56 stars detected in the J band (p_J) and polarization position angle (θ). Additional columns contain the JHK magnitudes with errors from 2MASS and distances from the Gaia survey.	44
2.6	Estimated values of linear polarization for 76 stars detected in the H band (p_H), polarization position angle (θ). Additional columns are the JHK magnitudes and errors from 2MASS & distances from Gaia survey.	48

2.7	Estimated values of linear polarization for 33 stars detected in the Ks band (p_{K_s}) and polarization position angle (θ). Additional columns are the JHK magnitudes and errors from 2MASS and distances from the Gaia survey.	53
3.1	The design goals & specifications for the NISP instrument.	69
3.2	Properties of the materials for lenses used in NISP. The refractive index values for a few of the materials at the respective central wavelength are taken from https://refractiveindex.info	73
5.1	The required parameters for an $R = 2150$, KRS5 material grisms in the Y, J, H, K_s filters in the 1st order, with $F_{coll} = 339$ mm, and $\Delta_x = 0.097$ mm are tabulated.	123
6.1	The surface definition for the WeDoWo design in Zemax, with the parameter values for different surfaces.	142
6.2	The multi configuration editor data used to input the values for all the 4 beams in the polarization design using YLF.	144

List of Figures

1.1	The neutral points position in the principal plane of Sun. Image credit: from (Abayaratne et al., 2016)	2
1.2	Polarization vectors for the measurement of stars, (a) along the Galactic Plane with $\pm 60^\circ$ in latitude. The scales are marked for reference. Small circles are drawn for stars with $P < 0.08$, (b,c) correspond the measurements for the galactic poles. (From Mathewson & Ford (1970))	3
1.3	Interstellar polarization	5
1.4	Multi-wavelength Milky Way	13
2.1	Color magnitude diagram for L1340 with the detection in different filter bands marked with different symbols. The black open circles mark the positions of stars measured with NICSPol in all three NIR bands. The open squares denote the stars towards the core of RNO 8 in this and all other figures.	30
2.2	Color color diagram from 2MASS for L1340. Symbols are as in Figure 2.1.	33
2.3	2MASS $J - K_s$ colour vs Gaia distance. Different symbols show the stars for which polarization is measured. Stars of the RNO 8 area are shown as open squares. Vertical dashed line is at 825pc - the distance to the cloud as per Kun et al. (2016a).	34
2.4	Polarisation in the H band as a function of the corresponding 2MASS H magnitudes.	35
2.5	Position angle distribution in J, H and K_s bands. A gaussian fit is overlaid on each panel.	35

2.6	H band polarization vectors (thin solid lines) plotted on the H filter 2MASS image of L1340. The thick vectors are for stars corresponding to the RNO 8 area. The solid line at bottom left corner indicates a 10% degree of polarization value. The contours in red are from the WISE (band 4) image of the same area.	36
2.7	Wavelength dependence of NIR polarization towards LDN 1340. The dashed line at the top represents the polarization determined from mean Q and U of all stars (see text for further discussion).	37
2.8	H band polarization vectors overlaid for the RNO 8 stars on the RGB colour composite of the WISE 4,3,2 bands. The black circle marks the core of RNO 8. Further discussion is in the text.	38
2.9	Distance (in pc from Gaia) vs polarization percentage (lower panel) and polarization position angle (upper panel) for H band measurements. Stars in the vicinity of RNO 8 are shown with larger symbols. The central star of RNO 8 is shown with a green open circle.	39
2.10	Polarisation in the <i>H</i> band (percentage in lower panel and angle in upper panel) vs $J - K_s$ colour (from 2MASS). The symbols are as in Figure 2.9.	40
2.11	Normalized q-u plot for all the stars with measured polarization in L1340. Different symbols mark the respective filter detections. Stars part of the RNO 8 core are shown as open squares. The green open circle corresponds to the star discussed in section 2.4.3.3.	41
3.1	3D shaded model of the circular Wire Grid Polarizer as used in NICSPol.	62
3.2	The labelled, shaded model layout for the NICSPol module added above the cryostat window of NICS. The optics inside the white dotted box is maintained at cryo temperature $\sim 77K$	63
3.3	Polarization pupil map of the wire-grid polarizer at 4 modulation angles of the polarizer. The transmission percent for each of the orientation is seen in the bottom panel of each plot. The results are shown for $1.635 \mu m$ wavelength (H band central wavelength).	64
3.4	The spot diagram at the image plane for NICS instrument	65

3.5	The increase in the spot size upon addition of the WGP component in NICSPol is seen compared to Fig 3.4. The spot in the third field location (0, -9.273) is lost due to rays being blocked by the WGP support (vignetting).	65
3.6	The MTF plot for NICSPol. The black line is for the diffraction limited performance. Other colors are for the different field locations defined for NICSPol.	66
3.7	Vignetting plot for NICSPol. The fraction of unvignetted rays starts falling beyond 2' radius.	66
3.8	Different layouts considered at the the design planning stage for the NISP optical design	68
3.9	Refractive index variation with wavelength. Image by Bob Mellish, CC BY-SA 3.0, https://en.wikipedia.org/w/index.php?curid=11902841 .	72
3.10	Wavefront map for an aberrated image. Image credit : Margy Green . .	76
3.11	A compilation of the aberrations present in an optical system and the analysis tools present in Optic Studio, Zemax with proper representations. Image courtesy: Optic Studio	78
3.12	Aberrations and corresponding analysis tools in Zemax. Image credit : Margy Green	79
3.13	A snapshot of the Merit function editor of NISP imaging design.	81
3.14	The filter wheel assembly of NISP	82
3.15	Schematic detailed description of the different modes of NISP and their functionality	83
4.1	NISP instrument optical design as backend to 2.5 m telescope	86
4.2	Schematic of the collimator design approach.	88
4.3	Zemax window showing the collimator layout, aperture settings, wavelength settings done for the final design.	89
4.4	The design approach from a reversed input design (top) to NISP collimator design (bottom)	90
4.5	Footprint diagram where the different circles reveal individual fields, and the diameter denotes the width of the pupil.	92
4.6	NISP instrument optical layout showcasing the cryostat window placement before Cassegrain focal plane.	95

4.7	Labelled imaging optical design of NISP. The design will be referred as variant 1 for the top panel & variant 2 for the bottom panel.	96
4.8	Spot diagram for the variant 1 (top panel) and variant 2 (bottom panel) .	97
4.9	Spot diagram at the Cassegrain focus of the telescope, showing diffraction limited performance achievable by the telescope.	98
4.10	The footprint diagram showing all field points covering the diameter of circle	99
4.11	Diffraction encircled energy plot for variant 1 (top panel) and variant 2 (bottom panel)	101
4.12	Vignetting plot of NISP	102
4.13	The MTF plot for the imaging design of NISP for variant 1 (top panel) and variant 2 (bottom panel).	103
4.14	Wavefront map for the central and extreme field for NISP. <i>Top panel:</i> On-axis & off-axis maps from variant 1, <i>bottom panel:</i> on-axis & off-axis maps from variant 2.	104
4.15	Plot showing the field curvature and distortion values for the two variants 1 & 2, top and bottom panels, respectively	106
4.16	Image simulation tool of zemax, showing the source (left) & final image (right) from the NISP optics for the two variants 1 & 2, top and bottom panels, respectively.	107
4.17	Magnitude vs Exposure time plot for SNR =5 at the central wavelength for each filter band in NISP.	108
4.18	Optical layout for NISP for different thermal configurations.	110
5.1	Schematic for grism design. Credit : Deen et al. (2017)	117
5.2	A schematic representation of the different orders from a transmission grating surface.	120
5.3	Grism design	124
5.4	An optical design layout for a low resolution, $R \sim 560$ grism for NISP. . .	125
5.5	The footprint diagram shows the simultaneous coverage of different wavelength bands on the detector plane for the low resolution grism. . .	125
5.6	Layout of the Y, J, H, K_s grisms for NISP with $R \sim 2150$ for $m = 1$ using KRS 5 material.	126

5.7	Spot diagram for on-axis field for the Y (top left), J (top right), H (bottom left), K_s (bottom right) filters.	127
5.8	Matrix spot diagram for the Y, J, H, K_s grisms of NISP defined as different configurations in Zemax.	128
5.9	Diffraction encircled energy for the Y, J, H, K_s grisms at their central wavelength.	128
6.1	Comparison showing the extinction ratio for different types of polarizers available in the VIS-IR wavelength range. (From 'Edmund optics' https://www.edmundoptics.com/knowledge-center/application-notes/optics/polarizer-selection-guide/)	136
6.2	<i>Left:</i> The schematic design of WeDoWo showing the pupil plane beam being split into the components from up and down Wollastons. <i>Right:</i> Work concept of WeDoWo. The image is from Oliva (1997).	138
6.3	<i>Left :</i> A block diagram of the WeDoWo with different angles which comprise its design. <i>Right :</i> The dependance of the required angles on the θ factor is shown for optical (MgF_2) & infrared (YLF) materials. The image is part of (Oliva, 1997).	139
6.4	Shaded design of YLF (left) & MgF_2 (right) WeDoWo for NISP designed with angle definition as mentioned in section 6.3.2. The orange color is the wedge and dark grey color are the Wollaston.	141
6.5	Layout of the imaging polarimetric mode of the NISP instrument. The different colors at the image plane are for the 4 angles consisting of two o-rays and e-rays respectively.	145
6.6	An isometric layout of the NISP polarimetric design. The starting is from the left side, where the rectangular aperture seen is the focal plane mask.	145
6.7	The focal plane mask to display 4 non-overlapping images.	146
6.8	The image plane of the NISP imaging polarization mode showcasing the 4 strips as imaged by the system.	147
6.9	Vignetting plot for NISP imaging polarization mode. The plot for the imaging mode is shown in Figure 4.12	147
6.10	Spot diagram of o-ray showing the variation in spot pattern as a function of field angles. The colors denote the wavelengths defined for the system.	148

6.11 Matrix spot diagram for NISP imaging polarimetric mode with MgF_2 (left) & YLF (right) material. It shows a full matrix of individual spots for all the configurations. 149

6.12 The polarization pupil map for all the 4 configurations of NISP imaging polarization design. The maps are for the central field at $1.635 \mu\text{m}$. The first row defines the 0° input polarization state & the outputs for the 4 combinations from 2 Wollastons. Similarly the 2nd, 3rd & 4th row define the 90° , 45° & 135° input polarization respectively. 151

7.1 The design goals and achievements for NISP 157

Chapter 1

Introduction

The journey of our understanding of polarization from its dawn, some 200 years ago to its introduction to the domain of astronomy, is worth revisiting.

A few notable personalities have made valuable contributions to the field of polarization in the physical sciences. The field started with the discovery of birefringence of Iceland Spar by Erasmus Bartholinus (1669), investigated by Huygens (1690). This was followed by the famous Malus ' $\cos^2\theta$ ' law relating to flux of light transmitted from two crystals, whose principal axes are separated by an angle θ from each other (Malus, 1810). According to the Oxford English Dictionary, the coinage of the word 'polarization' was by Malus. Sir David Brewster formulated the property of polarization intensity present at a particular angle of the reflecting surface. The Royal Society awarded the Count Rumford Medal to Malus for his work on double refraction in 1810. Around the same decade, Thomas Young had established that light has a wave nature through his interpretation of Newton's rings. However, the significant advancement in the field awaited the merging of the behavior of polarized light and the principles of wave theory. Fresnel conducted an experiment in connection with a double-slit experiment, using polarized light. The results explained that if the slits were illuminated separately using beams of

polarized light with their planes at right angles, the interference phenomenon was not present. This was the key to a long-sought mystery. Hence, Fresnel (1824) concluded that the vibrations of the polarized beam must be perpendicular to the plane of polarization. Bernoulli and Thomas Hooke had stated similar ideas.

As the world of the physical sciences began to appreciate the importance of polarization, it was also welcomed in the field of astronomy. Arago took the first polarimetric observations in astronomy (1811), by directing his instrument to the Moon to see the properties of reflected sunlight, as it seemed to Malus. It was then that he discovered that the light of the daytime sky is polarized with its maximum occurring at 90° to Sun. He also found 'Arago's neutral point' (see Figure 1.1), which is light at 25° above the antisolar direction being unpolarized. Later, two other neutral points were found, the Babinet & Brewster point at 10° & 20° along the vertical circle through the Sun. With many other further contributions lined up to make their mark in the field, the introduction to stellar astronomy was made by Chandrasekhar (1946). He predicted that the radiation of early type stars should be polarized. This led to the challenge of discovering polarimetric variability in eclipsing binaries.

Struve & Zebergs (1962) commented, *The detection of interstellar polarization will always re-*

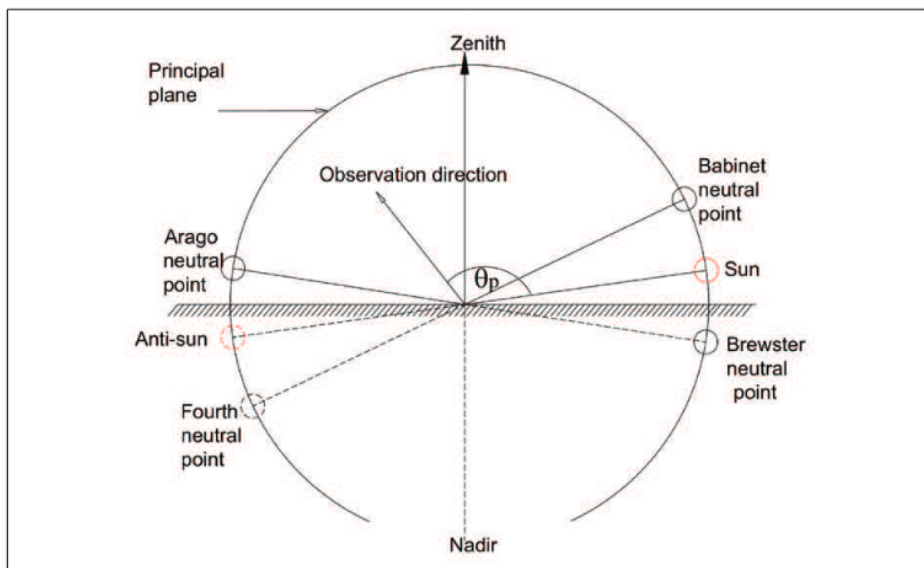


Figure 1.1: The neutral points position in the principal plane of Sun. Image credit: from (Abayaratne et al., 2016)

main one of the most striking examples of purely accidental discovery, such as Wilhelm Rontgens

discovery of X-rays in 1885. This referred to the serendipitous discovery of interstellar polarization. As a response to Chandrasekhar's prediction of starlight polarization, Hall had designed a photoelectric polarimeter to measure the constant interstellar polarization in 1948. Hiltner also carried out measurements of polarization for CQ Cep, Z Lac and HD211853 and provided substantial levels of polarization. Hiltner & Hall continued to make measurements to produce catalogues (Hiltner, 1951, 1954); Hall (1958)) mapping the variations in interstellar polarization across the Galaxy. The work was completed further by taking measurements of 1800 stars by Mathewson & Ford (Fig.1.2) (Mathewson & Ford, 1970). A very remarkable conclusion emerged, about the

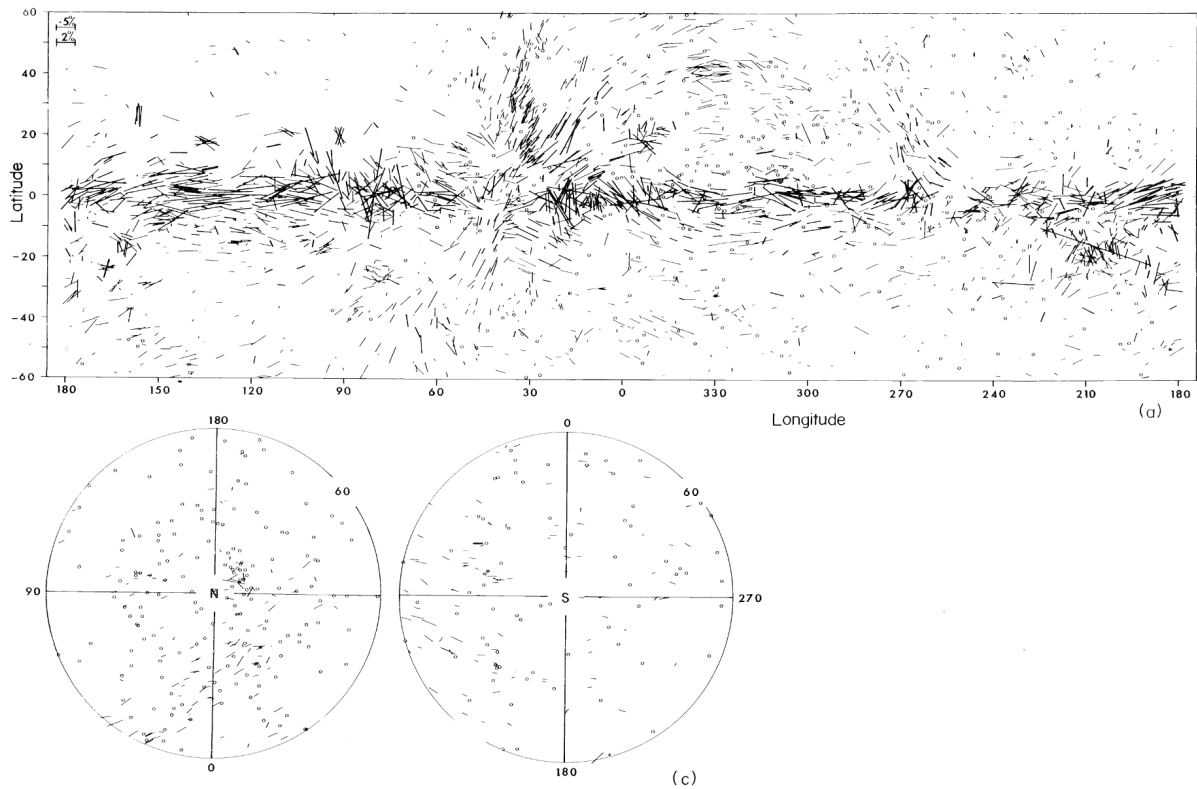


Figure 1.2: Polarization vectors for the measurement of stars, (a) along the Galactic Plane with $\pm 60^\circ$ in latitude. The scales are marked for reference. Small circles are drawn for stars with $P < 0.08$, (b,c) correspond the measurements for the galactic poles. (From Mathewson & Ford (1970))

wavelength dependence of interstellar polarization, in 1970 by Serkowski, an empirical formula which came to be known as Serkowski's law (Serkowski et al., 1975).

1.1 Interstellar polarization

The concept of interstellar polarization arose from the early results of a pattern seen in the position angles for OB stars, in the work done by Hall & Hiltner in 1949. Such consistent pattern in the position angle required a global mechanism which caused the angles to orient in the same direction for all the stars. The work further led to the conclusive recognition of the phenomena of *interstellar polarization*. Interstellar polarization, is a process in which starlight gets polarised when it passes through a dust cloud in the presence of magnetic field (see Figure 1.3). The dust particles in the cloud are hypothesized to be asymmetric and align preferentially with their short axis parallel to local magnetic field. Starlight passing through the dust cloud gets preferentially absorbed along the long axis of the asymmetric dust grains. This causes the starlight to be polarized along the shorter axis. Hence, the starlight polarization is parallel to the local magnetic field. This model is termed *linear dichroism*. Further description on the different processes which lead to grain alignment is discussed in section 1.1.3.

1.1.1 Relation between extinction & interstellar polarization

Two main conditions lead to the partial plane polarization of the unpolarized star light, as listed below :

1. The dust particles are anisotropic
2. Net alignment in the axes of anisotropy

It has been discussed (for example by [Whittet, 1992](#), and references therein), that the asymmetry in shape is crucial for the alignment of the grains. Since, the dust grains in the ISM have various asymmetric shapes, these are assumed to have a simplistic cylindrical shape for explaining the alignment mechanism. This helps in the calculation of their extinction cross-sections using an extension of the Mie theory. The approximations are restricted to a range of wavelength & particle sizes, hence other models were

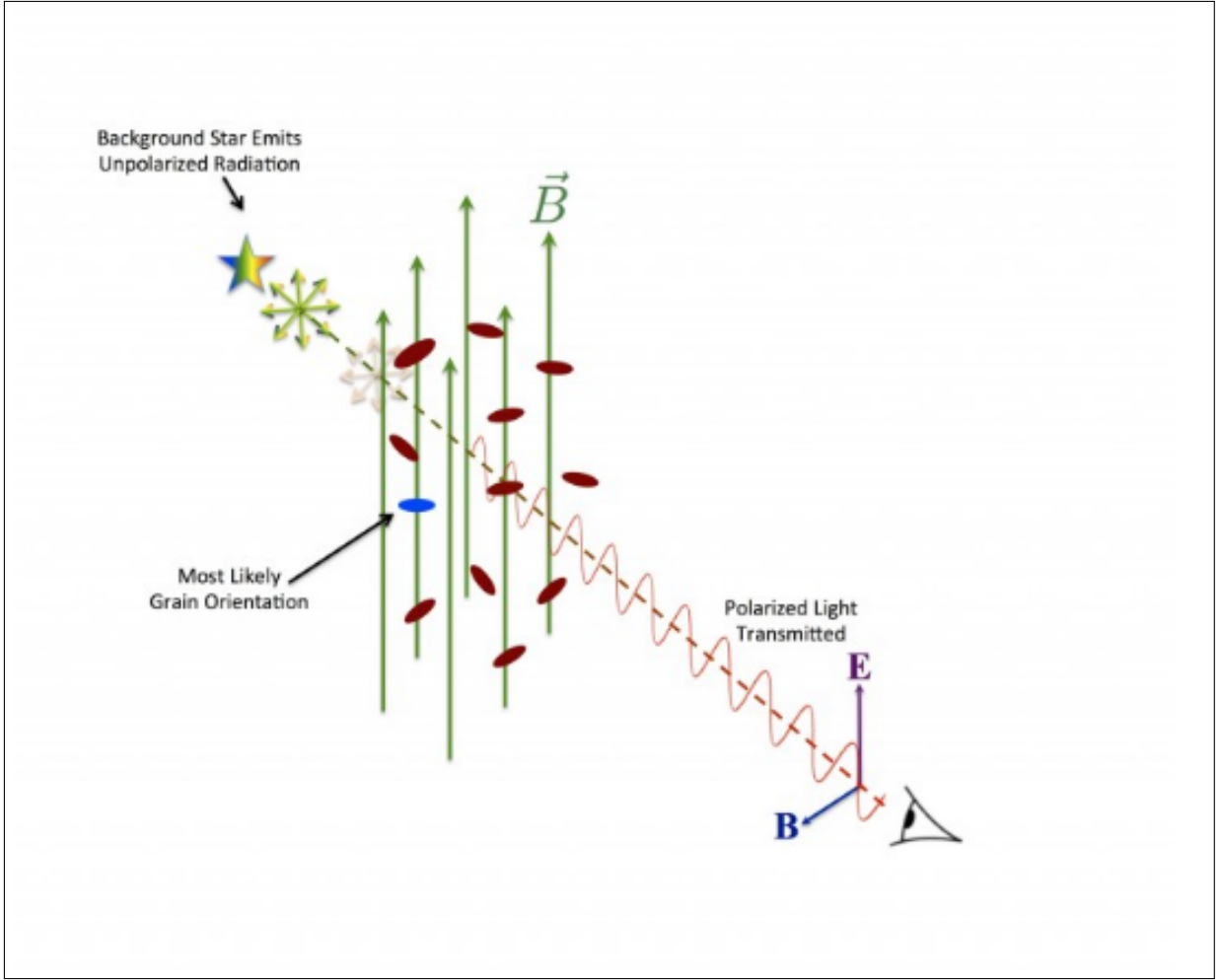


Figure 1.3: Schematic representation of the mechanism of interstellar polarization of the star light. Image credit : PASIPHAE survey.

also devised for more sophisticated approach, which is discussed in the further section. For spherical dust grains, the extinction coefficient κ is given as,

$$\begin{aligned}
 \kappa &= n_d(cm^{-3})C_{ext}(cm^2) \\
 &= n_d\pi a^2 Q_{ext} \\
 &= n_d\pi a^2(Q_{abs} + Q_{sca})
 \end{aligned}
 \tag{1.1}$$

where, C_{ext} is the cross-section for grain extinction,

n_d is the grain volume number density,

a is the size of grain (radius),

Q_{ext} is the extinction efficiency factor.

We assume the dust grains as elongated cylinders, with their long axes perpendicular to the axis of rotation, which is aligned with the magnetic field. If the long axis is perpendicular to the direction of propagation, the Q_{\parallel} & Q_{\perp} are defined as the extinction efficiency when the \vec{E} - vector is parallel & perpendicular to the long axis of the grain. The anisotropy in the shape leads to an anisotropy in the extinction, and the \vec{E} sees larger grain in parallel direction. This gives $Q_{\parallel} > Q_{\perp}$. The quantity we infer as $\Delta Q = Q_{\parallel} - Q_{\perp}$ is a measure of the polarization, for a given grain size. A theoretical upper limit is placed on the polarization efficiency for the visual wavelengths (Chapter 4 of [Whittet \(1992\)](#));

$$\frac{p_V}{A_V} \leq 0.3 \quad (1.2)$$

where, p_V refers to the polarization magnitude in the visual wavelength and, A_V refers to the extinction at the visual passband. The extinction at a given wavelength is connected to corresponding color excess, E_{B-V} through the extinction curve.

The observational upper limit for the ISM at visual wavelengths using a sample of field stars in the Milky Way galaxy is found as (Chapter 4 of [Whittet \(1992\)](#)),

$$\frac{P_V}{E_{B-V}} \leq 9.0\% \text{mag}^{-1} \quad (1.3)$$

Here, P_V is the polarisation efficiency at visual wavelength.

This tells that the ISM efficiency as a polarizing medium is non-uniform. The equation can be checked for an observational polarization efficiency, to compare with Equation 1.2, using the relation $P \approx 46.05p$. The observational polarization efficiency expressed

as ratio of polarization to extinction then becomes (Chapter 4 of [Whittet \(1992\)](#)),

$$\frac{p_V}{A_V} \leq 0.064 \quad (1.4)$$

This is a factor of 4 less than the theoretical limit set for a grain model consisting of grains as infinite cylinders with diameters comparable to wavelength & the long axis perpendicular to the direction of propagation (i.e. our line of sight).

1.1.2 Polarisation & wavelength dependance

The measured polarization for stars show a variation with the wavelength. The peak of polarization varies from star to star in the range $0.3 \mu\text{m} - 0.8 \mu\text{m}$, with mean peak at $0.55 \mu\text{m}$ wavelength. The dependance of polarization on wavelength, was given by an empirical formula by [Serkowski et al. \(1975\)](#),

$$P_\lambda = P_{max} \exp\left\{-K \ln^2\left(\frac{\lambda_{max}}{\lambda}\right)\right\} \quad (1.5)$$

The term P_{max} is the polarization fraction at the peak wavelength. The parameter K , defines the width of the spectral dependance curve of polarization & its value is considered a constant for visual wavelength bands, with $K = 1.15$. The significance of the Serkowski law is in the value for the λ_{max} term. This term relates to the physical size of the grain which is responsible for polarization. It is shown that for dielectric cylinders of radius a & refractive index n , efficient polarization is produced for,

$$\lambda_{max} = 2\pi a(n - 1).$$

Later an extension for the law in the NIR region concluded that K also has a functional dependance over λ_{max} . This came to be known as Wilking's law ([Wilking et al., 1979](#)),

$$K = c_1 \lambda_{max} + c_2 \quad (1.6)$$

where, c_1 & c_2 are constants. The values of these constants were determined from the fit to the data in the visible to NIR ($0.35\mu\text{m} < \lambda < 2.2\mu\text{m}$), which gives $c_1 = 1.66 \pm 0.09$ & $c_2 = 0.01 \pm 0.05$ (Whittet et al., 1992). The Wilking law is considered to be very accurate for NIR polarization, but underestimates the dependence in the UV wavelength band. For the lower wavelength range ($0.12\mu\text{m} < 0.55\mu\text{m}$), the better fit is found using $c_1 = 2.56 \pm 0.38$ & $c_2 = -0.59 \pm 0.21$ (Martin et al., 1999). Recent studies on interstellar polarization have shown a consistency with the Serkowski law, for example, (Messinger et al., 1997), (Hatano et al., 2013), (Wang et al., 2017), (Kwon et al., 2016), (Eswaraiah et al., 2019) and many more. Further work has been done towards the interpretation of Serkowski's law by Papoular (2018), who presents the spectral dependence of polarization within the wavelength range $0.3 \mu\text{m} - 0.8 \mu\text{m}$ to be caused due to the optical properties of the silicate grains, and not the size of the grains. He simulated the results based on different proportions of the forsterite & enstatite which resulted in a shift of the peak from $0.8 \mu\text{m}$ to $0.3 \mu\text{m}$. This leads to a new understanding of the Serkowski law considering the optical properties of the grains, as against the grain size, as leading to the position of the peak in the polarization spectrum.

1.1.3 Grain alignment & magnetic field

The polarization from unpolarized starlight is a result of the net differential extinction of the light due to interstellar dust grains aligned by the magnetic field present in the region. A very interesting discussion on grain alignment presented by Andersson et al. (2015) tells that the process of the alignment is dependant on the internal alignment & randomization. The randomization of the grains should not overcome the process of internal alignment. The randomization happens because of the gas-grain collisions (Draine & Lazarian, 1998). Internal alignment of the grains requires the angular momentum vector of the grains to be aligned with a main grain axis, which is the axis of maximum moment of inertia.

The initial theory for grain alignment depended on *ferromagnetic* dust grains, which get aligned in the presence of a magnetic field. But this theory couldn't get a strong

hold because the grains having temperature of the diffuse ISM needed a stronger interstellar magnetic field than present in our Galaxy, to align themselves. Hence, three main alignment paradigms were devised: paramagnetic relaxation (Davis & Greenstein, 1951), radiative torque alignment (RAT) (Dolginov & Mitrofanov, 1976) & mechanical alignment (Gold, 1952a,b).

The **Davis Greenstien (DG)** mechanism is based upon the paramagnetic dissipation of energy by the dust grains & its spin by collisions in the gas. It relies on the fact that the relaxation time t_{DG} is much smaller than the randomization time in gas t_{gas} due to collisions. A decade long comparative study has been done to conclude the mechanism of alignment in the interstellar dust grains, and the results have been tabulated in the annual review article by Andersson & Potter (2007). It shows that the observational evidence & theoretical understanding for the DG mechanism don't go in sync. Hence, though this mechanism has a widespread use to explain the alignment process happening in the diffuse ISM, it is mostly constrained towards the smaller grain sizes ($a \leq 0.1 \mu\text{m}$).

Radiative torque alignment (RAT) mechanism explains the alignment process considering the paramagnetic dust grains, in which a net alignment is caused due to asymmetry in the grain shape. The asymmetry leads to the formation of torque which leads to increased angular momentum. As per Barnett effect (Barnett, 1915), this rotation due to angular momentum component induced a net magnetization in the dust grains. In the presence of an external galactic magnetic field, the magnetized dust grains does Larmor precession around the field direction. This continuous action of torques on the dust grains, leads to a significant alignment of the grain with the magnetic field.

On the other hand, in the **mechanical alignment** mechanism, the grains will align perpendicular to a systematic gas particle flow. It is based upon an interaction of the grain with the gas particles. No observational evidence could match this theory.

The strength of the local plane of the sky magnetic field varies depending upon the

amount of dust present and the coherent orientation of these grains to produce a net magnetic field. The calculation of the magnetic field was formulated by [Chandrasekhar & Fermi \(1953\)](#). The paper describes the method to estimate magnetic field strength for the spiral arms in which we are located. The theory considered the velocity of a transverse magneto hydrodynamic wave, to build a relation between the magnetic field & other parameters needed to estimate it. The \vec{B} field strength came to be $7.2 \mu\text{G}$ using this method. The method helped to estimate the plane of the sky magnetic field strength in the molecular clouds. It is independent of the Zeeman effect which is difficult to detect in molecular clouds due to the smaller frequency splitting in the presence of weak magnetic fields in these regions. The estimation of the mean field strength was laid on the knowledge of the mean gas density, the line-of-sight velocity and the position angle dispersion (obtained from polarization measurements). The position angle dispersion is connected to the dispersion in the orientation of the magnetic field in the plane of sky. The estimated magnetic field strength using this method is found to be accurate with a value for multiplicative factor $Q \sim 0.5$, when the polarization angle fluctuations are small, typically $< 25^\circ$ ([Ostriker et al., 2001](#)). For dispersion in position angles greater than 25° , the method fails, and more comprehensive analysis needs to be undertaken.

1.2 Aspects of polarization measurements

Polarisation of light, being one of the most interesting techniques to be applied in astronomy, is actually very vulnerable to measurement errors due to multiple reasons. It is a very sensitive technique in which proper care is advised while taking observations and while reducing the data to get polarization values. The variable sky transparency, effects of telescope optics, instrument optics, thermal background are factors which can modify the incoming polarization of light. It will be worthwhile to get some insights into the polarization measurement approach & the ways to take care of the limitations in it.

1. A calibrator is very important in the polarimetric instrument to measure the polarization efficiency of an instrument. Efficiency tells us the response to an incoming polarization of the light as measured at the detector plane. It is dependant on the polariser optics and needs to be measured so as to be applied to each of the polarization measurement taken by the instrument. e.g. a 100% polarised light might get measured as 97% by our optical system. The factor of 0.97 will be divided from the measured degree of polarization to give correct number from our instrument.
2. The optics in the instrument may also cause some additional polarization, termed as the instrumental polarization. This factor needs to be accounted for while quoting the measured polarization. It is estimated by taking measurements of polarised standards i.e., polarised & unpolarised stars. The additional amount of polarization than the standard values, if present in our measurements, will tell us the instrumental polarization induced by the instrument. This instrumental polarization has to be removed in the Stokes Q-U space.
3. Cross polarization may also occur, due to the presence of 45° mirrors in the optics.
4. [Pancharatnam \(1955\)](#) discusses the wavelength dependence of the half-wave plates, and the combinations of achromatic half-wave plates to avoid it. This is a very important aspect to consider while making polarization measurements at multiple wavelengths.
5. The polarization measurements need intensities to be captured at different modulation angles. The sky variations at these time intervals between the different angles should be corrected. Separate sky frames should be taken for correcting the sky response & nullify the effect of any variations. It becomes better if we can use a analysing component which can simultaneously measure the four angles needed to deduce the degree of polarization & position angle.

[Jones \(2011\)](#) discusses the different techniques used in the near & mid- infrared polarimetric instruments.

1.3 Polarimetry of dark Lynds clouds

The dark nebulae, such as the ones described by Lynds (1962), have been relatively unexplored in the optical due to the large extinction towards these regions. Beverly Lynds catalogued these dark nebulae into opacity classes on the basis of their visual appearance in the National Geographic-Palomar Observatory Sky Survey images. The clouds catalogued were divided into opacity class 1 - 6, with visual opacity equal to 6 being the most extincted cloud. Polarimetry is a good way to probe the magnetic field structures (Davis & Greenstein, 1951) in the dark clouds (Joshi et al., 1985; Jones, 1989; Myers & Goodman, 1991; Andersson & Potter, 2007). Polarimetric observations of the stars in the line of sight through the dark nebulae/molecular cloud would help to probe the magnetic field structure in the cloud and along the line of sight (Lazarian, 2007). For example Eswaraiah et al. (2019) have studied the dark globule LDN 1225 using optical polarimetry and infrared photometry to understand the extinction and magnetic field properties of the region.

Infrared polarimetry would be even more appropriate in regions of high extinction. Earlier work (e.g. Wilking et al., 1979; Kwon et al., 2016) using infrared polarimetry have concluded that it is a valuable tool for measuring the dichroic polarization of the background stars and those embedded within the dense clouds.

Kwon et al. (2016) discuss the observations of GGD 27 in the Lynds 291 molecular cloud complex in the constellation of Sagittarius using the SIRPOL instrument on the IRSF telescope at Sutherland, South Africa. They study the complex structure of the magnetic field and derive the magnetic field strength based on their polarimetric observations.

Lynds dark nebula 1340 (hereafter referred as L1340), a cloud of opacity class 5, located at $\alpha = 2\text{h}32\text{m}$, $\delta = 73^\circ00'$ ($\ell = 130^\circ.07, b = 11^\circ.6$), has been studied using photometric and spectroscopic techniques in a series of papers (e.g. Kun et al., 1994, 2016a,b, and references therein) by M. Kun and collaborators. Kun et al. (1994) have studied L1340 as a starforming complex in Cassiopeia using optical photometry as well as radio (^{13}CO and C^{18}O) molecular emissions. Using objective prism spectroscopy they detected 13

$H\alpha$ emission line stars. Kun et al. (2016b,a) studied the region in the optical & infrared using the photometric data from SDSS, WISE and Spitzer surveys to determine the young stellar populations present in the region. They conclude that it is an isolated molecular cloud of $3700 M_{\odot}$ with an intermediate star formation efficiency $\sim 3\%$.

1.4 Multi-mode infrared instruments

Infrared wavelength band provides us with a boon of penetrating inside the vast and relatively unexplored dark regions of the Galaxy, which can be accessed from a ground based observatory. With a moderate aperture primary mirror, and a good site for operating in infrared wavelengths, the instruments can help us to probe many fascinating regions of the Galaxy and understand the phenomena happening there. The Figure 1.4 is a representation ¹ of our Milkyway galaxy in the optical to infrared wavelength bands. The dark patches seen in the optical wavelength are due to the gas and dust present in the region. The same regions in the infrared trace emissions throughout the galaxy from cool giant K type stars in the disk & bulge, red giant stars, planetary nebulae etc. The telescopes back-end instruments help us in studying the underlying phenomena

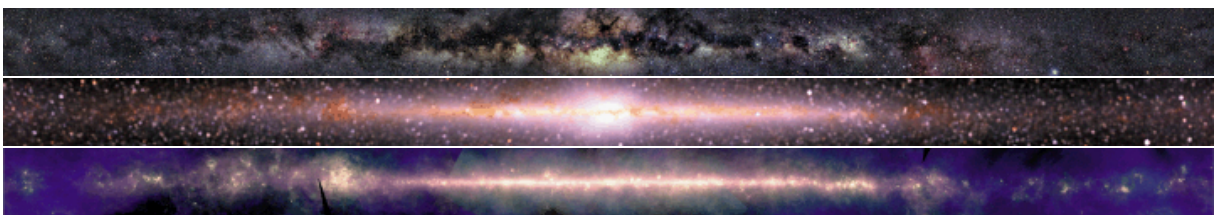


Figure 1.4: An image of the Galactic plane in the optical (top), near-infrared (middle) & mid-infrared (bottom) wavelength bands. Image credit : NSSDCA, NASA

in these regions. Since, one single technique cannot give us complete details about the properties of any astrophysical source, it is advantageous to gather information about the source from all available modes i.e. imaging, spectroscopy & polarimetry. One versatile instrument performing all functions is therefore a primary requirement and

¹https://asd.gsfc.nasa.gov/archive/mmw/mmw_images.html

such instruments are mostly available in all the big telescope facilities. One can study the same object in multiple functional modes and perform a thorough study of the underlying astrophysical phenomena. One of the important part of modern day observational astronomy is getting observation time with the telescope facilities, because data is required by the entire community & observation time is limited which needs to be utilised in a balanced way. To manage with the enormous demand for telescope time, it would be favorable for the observers to have instruments which can do multiple jobs.

Such multimode facilities have made their way to many ground based telescopes around the world. Examples of such instruments on 1-8 m class telescopes are: MIMIR (Clemens et al., 2020a), SIRPOL (Kandori et al., 2006), TRISPEC (Watanabe et al., 2005), NICS (Anandarao et al., 2008) and NICSPol (Aarthy et al., 2019), TIRSPEC (Ninan et al., 2014), EFOSC2 (Wiersema et al., 2018), FORS2 and many more.

MIMIR instrument has been involved in an infrared survey of the galactic plane called "Galactic plane polarization survey (GPIPS)" survey (Clemens et al., 2012a,b,c). This survey, using near-infrared polarimetry, mapped 76 deg^2 of the galactic plane ranging over $\ell = 18^\circ - 56^\circ$, $b = \pm 1$ in the H-band ($1.6 \mu\text{m}$). A recent data release DR4 (Clemens et al., 2020b) for the GPIPS survey provides polarization data for 13 million stars with the plane of the sky magnetic field orientations also listed for interstellar clouds at $A_v \sim 30$. Another survey called the "Large Interstellar Polarisation (LIPS)" survey, using spectropolarimetry technique has been performed in both the hemispheres in the wavelength range $0.3 \mu\text{m} - 0.95 \mu\text{m}$ to constrain the properties of dust from gas using the narrow band features from spectra. In the southern hemisphere, the survey utilised the FORS2 instrument on the VLT telescope to provide a public catalogue of 127 spectra for 101 stars (Bagnulo et al., 2017). In the northern hemisphere, they use the ISIS instrument at the William Herschel telescope. An optopolarimetric survey experiment, "Polar areas stellar imaging in polarization high-accuracy experiment (PASIPHAE)" (Tassis et al., 2018) is also under process which aims to map the polarization of millions of stars in both the Northern & Southern hemisphere with unprecedented accuracy. The results will be combined with the Gaia data to produce a 3D tomography of the

Galactic magnetic field.

1.5 Motivation

Located in the disk of the Galaxy, it is difficult to understand the structure of the Milky Way due to the enormous extinction caused by the dust in the galactic plane. As one goes towards longer wavelengths, one is able to detect the obscured stars. Multiple surveys of the Milky Way galaxy have been conducted in various wavebands but they chiefly focus on imaging and spectroscopy. The phenomena like polarization which depends upon the distribution of interstellar dust and the galactic magnetic field have been relatively less studied. The tools required are photo-polarimetry in optical (for low extinction regions) and the infrared bands. We would like to study the dust distribution in 3-D in order to know the distribution of matter in the galaxy. By studying the polarization distribution, we plan to get additional information about the magnetic field (its geometry & strength) and study the dust present in the region ([Chandrasekhar & Fermi, 1953](#); [Davis & Greenstein, 1951](#)). A polarimetric instrument in the near infrared is therefore a very valuable means to study the polarization distribution along the line of sight (in combination with distance determined using different techniques - e.g. red clump method, parallax measurements from *Gaia* etc). To this end, we have used PRL's 1.2m telescope with the NICSPol instrument ([Aarthy et al., 2019](#)), a polarimetric addition to the existing NICS instrument ([Anandarao et al., 2008](#)), to study near infrared polarization in the lines of sight towards an extincted region, a molecular cloud, Lynds 1340. The imaging polarimetry FOV with NICSPol is of circular diameter $3.9'$, with the polarization optics being warm (room temperature). The warm optics emits thermal noise at the edges particularly in the longer K_s band. However, results from this work underlines a very promising scientific approach and impresses on the need for a more versatile instrument with improved accuracy in polarization measurements, and no thermal noise from optics.

The Indian landscape is home to several telescope facilities for night-time astronomy. The telescopes are in a range of apertures from smaller ones till 3.6 m as the largest one. The different facilities are set up by PRL, IIA, IUCAA, TIFR, RRI etc. All of

them are equipped with instruments having good specifications, which perform their operations robustly. Mostly the instruments include imaging and spectroscopy modes in the optical and NIR wavelength bands, for example NICMOS, NICS (Anandarao et al., 2008), TIRSPEC (Ninan et al., 2014), TIRCAM-II (Baug et al., 2018), TANSPEC², HFOSC³, MFOSC (Srivastava et al., 2021), ADFOSC (Omar et al., 2019), IFOSC (Gupta et al., 2002). At PRL, the polarimetric instruments in the optical and NIR are PRL optical polarimeter (Deshpande et al., 1985), EMPOL (Ganesh et al., 2020) and NICSPol (Aarthy et al., 2019). High precision dual beam polarimetric instruments are available at ARIES "AIMPOL" (Rautela et al., 2004) & IUCAA "IMPOL" (Ramaprakash et al., 1998) in the optical wavelength. There are no dual-beam polarimetric instruments in the country at NIR wavelengths.

Near-infrared band is very important to look for fainter stars which are obscured behind dust clouds. They also possess polarisation on account of extinction from dust, which can not be seen and estimated in the optical waveband. But the degree of polarisation is very small, which requires a polarimetric instrument in the NIR with accuracy good enough to measure such low polarisation with precision. This motivated us to develop an instrument with multiple techniques included at the design stage itself. The different modes of NISP have been designed with all the requirements in mind and to make an attempt to fill the gap in capabilities with a larger aperture primary mirror. NISP (Near-IR Imager, Spectrometer & Polarimeter) is a new multi-function near-infrared instrument being planned and developed for PRL's upcoming 2.5 m telescope at Mount Abu. It will be the 1st infrared polarisation instrument in India, with 4 simultaneous beams considered.

The scientific rationale for this instrument mainly concentrates on using the lesser exploited role of polarimetry which demands a thorough study in the regions of heavy dust presence. This thesis is focused on designing the NISP optics which will cater to such scientific goals with improved precision and efficiency in determining polarization to much smaller levels with higher accuracy. NISP will be a general purpose instrument and multiple functional capabilities will need to be implemented. The optical design of NISP is done using physical principles to calculate the input parameters to the *Optic*

²<https://www.aries.res.in/sites/default/files/files/3.6-DOT/tanspec.pdf>

³https://www.iiap.res.in/iao/hfosc_details.html

Studio - Zemax software. The entire optics, detector and controlling ASIC assembly will be maintained under high vacuum at cryogenic temperature. The detector is a $2K \times 2K$ H2RG focal plane array from Teledyne Imaging Sensors. Our instrument, with its unvignetted FOV of $10' \times 10'$ in the imaging mode, provides for a reasonable area of sky to be imaged in the NIR filter bands Y, J, H, K_s . The imaging-polarization mode deals with providing *simultaneous* four position images with the use of Wedged Double Wollaston (WeDoWo) (Oliva, 1997). The four images shall be at 0° , 45° , 90° & 135° polarization orientations. The single shot polarization measurements are very effective in minimising the effect of varying sky background which leads to odd polarization values. It also simplifies the observational and data reduction processes. The spectroscopic mode with an intermediate resolving power ~ 2150 , is implemented with the use of gratings, alongwith broad band filters & low resolution grism for operations in single order mode & mixed mode respectively.

1.6 Research objectives

The basic objective is to have an overall understanding of the galactic structure, especially the inner regions i.e the highly extinguished galactic plane. By studying the polarization distribution, we hope to get additional information about the magnetic field and the dust present in the Galaxy. The current works have been carried out with the motivation to study the interstellar polarization of the galactic plane region in the IR bands by observing the dark clouds close to the plane of our Galaxy. Few of the Lynds clouds have been observed using NICSPol in the IR bands and another optical imaging polarimeter (EMPOL) on PRL's 1.2 m telescope. In this thesis, we cover the results for LDN 1340, a cloud in the northern sky easily observable from Mount Abu IR Observatory.

To enhance our observational capabilities towards the above mentioned science goal, a robust instrument NISP having larger FOV, better sensitivity with simultaneous polarization observations at 4 position angles, is being built for the upcoming 2.5-m telescope

at Mt. Abu infrared observatory. The thesis covers the optical design of NISP.

1.7 Thesis outline

The thesis consists of 7 chapters. These are briefly described below:

Chapter 1 : Introduction

This chapter starts with a summary of the concepts of extinction, interstellar polarization and its wavelength dependence. The infrared polarization study of the obscured molecular clouds tell us about the dust properties in the region, magnetic field geometry of the cloud and its strength. Towards the optical design of NISP, a few similar instruments available at telescopes around the world have been discussed briefly and the uniqueness of NISP is emphasized.

Chapter 2 : Infrared polarization study of Lynds 1340

This chapter describes the polarization study of a Lynds cloud, LDN 1340, $\alpha = 2\text{h}32\text{m}$ & $\delta = 73^\circ00'$ corresponding to galactic coordinates of $\ell = 130^\circ.07$ $b = 11^\circ.6$. The cloud has been observed using the 1.2 m telescope at Mt.Abu Infrared Observatory, in the infrared wavelength bands using Near-Infrared Camera, Spectrograph & Polarimeter (NICSPol) instrument. We combined our measurements with archival data from the 2MASS and WISE surveys. The *Gaia* data for the same region were used for distance information. Results from this work are discussed in the chapter.

Chapter 3 : Instrument Design

The chapter deals with the basics of optics design. It also provides a short introduction to the OpticStudio Zemax software. A tour through the learning stages of optical design with the description of various analysis tools present in Zemax, are covered. The flow of the NISP instrument is also described with details of the different functional modes.

Chapter 4 : Imaging Optics

The basic premise for the imaging optics of an instrument is explained. Using imaging optics to achieve the required scientific goals of the instrument is described sequentially. The collimator optics, camera optics, detector array and other parameters to be defined for an imaging system are also covered in this chapter. The analysis for the same is discussed in detail along with the Zemax results.

Chapter 5 : Spectroscopic Optics

This chapter explains the optics design of the NISP worked out for spectroscopic mode. The use of gratings for spectroscopy and the intricate calculations leading to the designing of these components have been described. The chapter further discusses the single mode & low resolution mixed mode of spectroscopy using different grating designs. The analysis for the same is discussed in detail along with the Zemax results.

Chapter 6 : Polarisation Optics

The polarization optics used in the NISP instrument is one of the most accurate components used in polarimetric instruments till date. It will be the 1st infrared polarisation instrument in India, with 4 simultaneous beams considered. The dual beam polarime-

ters, are considered to be accurate, as they compensate for atmospheric variations. The ratio of the orthogonal components taken simultaneously, gives an edge to such techniques employed in any instrument. World wide, there are very few instruments with similar capabilities. The design of, firstly, the WeDoWo component using calculations, and secondly its implementation in the optical path has been very challenging. The analysis related to the polarization design is also discussed using Zemax.

Chapter 7 : Summary & Future work

This chapter summarizes the major conclusions from the polarization study of a molecular cloud. It also summarizes the achieved specifications for NISP as against the targeted design goals. Potential goals and possibilities for future work is also discussed.

Chapter 2

Infrared Polarisation study of Lynds

1340

The dark molecular clouds are considered to be the precursors of protostars. They have been catalogued by [Lynds \(1962\)](#) from a study of red & blue photographic films at National Geographic - Palomar observatory sky atlas. The dark clouds were divided into opacity classes of 1- 6 based upon the star counts found in the respective films, with increasing relative obscuration. These estimates were done using neighbouring fields for the photograph on which a cloud is seen. The clouds visible in both the red & blue prints, with a small decrease in their surface intensity were designated as opacity class 1. The cloud not visible in the blue print, but having an average star count of 120 stars per square degree in the red print were designated as opacity class 6. The catalogue tabulates their coordinates, visual opacity, area obscured by the clouds etc. Similar catalogs have been prepared by [Lundmark \(1926\)](#) & [Barnard \(1927\)](#), mapping extensively 1500 and 369 dark nebulae in the Milky Way.

Considering their importance in understanding the magnetic field geometry in such

clouds, here we describe the polarization study of a Lynds cloud, LDN 1340, $\alpha = 2\text{h}32\text{m}$ & $\delta = 73^\circ00'$ corresponding to galactic coordinates of $\ell = 130^\circ.07$ $b = 11^\circ.6$, with emphasis on the RNO 8 area. This is a red and nebulous object, which consist of groups of fainter stars associated with them (Cohen, 1980; Larionov et al., 1999). The RNO 8 region is well studied photometrically & spectroscopically by Kun et al group. and one major result being that the central star is a candidate embedded intermediate-mass young star of the optical nebulosity RNO 8. They suggest it to be a young star of 2 - 2.5 M_\odot (Kun et al., 2016b). The cloud has been observed using the 1.2 m telescope at Mt.Abu Infrared Observatory, in the infrared wavelength bands using Near-Infrared Camera, Spectrograph & Polarimeter (NICSPol) instrument. The polarimetric observations were used to map the magnetic field geometry around the region. We combined our measurements with archival data from the 2MASS and WISE surveys. The Gaia data for the same region were used for distance information. The analysis of the data reveals areas with ordered polarization vectors in the region of RNO 8. The position angle measurements reveal polarization due to dichroic extinction which are consistent with the Galactic magnetic field. The magnetic field strength was calculated for the RNO 8 region using the Chandrasekhar-Fermi method and the value estimated is $\sim 42\mu\text{G}$.

2.1 Observations

2.1.1 Telescope and instrument

Physical Research Laboratory (PRL) operates a 1.2 m telescope at its Mount Abu Infrared Observatory (MIRO). MIRO is located at $24^\circ39'9''$ (N) latitude, $72^\circ46'47''$ (E) longitude at 1680 m altitude. The observatory location favours good conditions for infrared (IR) observations with a median seeing $\sim 1''$ in the visual band. PRL's 1.2 m f/13 telescope is equipped with a Near-IR Camera & Spectrograph (NICS) serving as one of the general purpose back-end instruments. The wavelength bands covered are J, H, Ks. The imaging detector is a Teledyne H1RG array. In imaging mode, the instrument

has a square FOV of $8' \times 8'$ with a spatial scale of $0.5''$ per pixel. The capabilities of the instrument were enhanced with the addition (Aarthy et al., 2019) of a polarimetric module (NICSPol), between the telescope optics & NICS. The technique of polarimetry is implemented using a $25.0 \text{ mm} \times 25.0 \text{ mm}$ wire-grid polarizer (WGP) module at room temperature fixed in a motorised rotator originally used as a field rotator for a small telescope (Pyxis LE field rotator model from Pyxis Instruments). With this arrangement, the wire-grid serves as both a modulator & an analyzer. The clear circular field of view at the image plane is $\sim 3.9'$ in diameter due to vignetting by WGP. Images are taken at 4 angular positions (0° , 45° , 90° & 135°) of the wire-grid polarizer.

2.1.2 Observational procedure

The observations of the L1340 with particular emphasis on the RNO 8 and surrounding area were fulfilled using NICSPol. All observations were completed during dark nights, and at multiple epochs in November 2017 with appropriate polarization standard stars done each night to facilitate the standardization procedure. The relatively small FOV of NICSPol ($3.9'$ diameter) meant that multiple pointings were required for a complete coverage of the field. We covered the region of L1340 from $\ell = 130.08^\circ - 130.24^\circ$ $b = 11.44^\circ - 11.60^\circ$, an effective field of $9.6' \times 9.6'$ with 6 positions (spread over different central coordinates) taken in succession for one waveband per night. For each of the Near-IR filter bands, images at 4 wire-grid position angles were acquired. With the individual exposure times of 50 sec, and three exposures per pointing per position angle, the effective exposure time was 150 sec per position angle per pointing. Standard polarized and unpolarized stars were observed at multiple times, in all filter bands, during the night, to get a coverage of redundant standards over the night.

2.2 Data reduction and analysis

The observed data were reduced and analyzed using standard IRAF routines. This involved a series of steps in the sequence of basic image reduction, astrometry, photom-

Table 2.1: Observational results for the polarized standard stars. The standard value for p & θ are taken from NOT & UKIRT links. The observed values are listed as p_{obs} & θ_{obs} . The offset for position angles is given by θ_{off}

Star	Date	Filter	p (percent)	θ ($^{\circ}$)	p_{obs} (percent)	θ_{obs} ($^{\circ}$)	$\theta_{off}=\theta_{obs}-\theta$ ($^{\circ}$)
HD204827	16/11/2017	J	2.83 ± 0.07	61.1	2.83	-3.19	-64.29
	16/11/2017	H			1.11	-1.19	-62.29
	17/11/2017	J			3.39	-16.72	-77.82
	17/11/2017	H			1.84	-4.94	-66.04
HD283809	16/11/2017	J	3.81 ± 0.07	57 ± 1	3.26	-13.09	-70.09
	16/11/2017	H	2.59 ± 0.07	58 ± 1	1.32	-6.27	-64.27

etry & polarimetry. We created sky frames for each pointing by median combining all the rest of the observed pointings for a given WGP position. The minor shifts in the 4 object frames for different WGP position angles were corrected using the `IMSHIFT` task. Astrometric solutions were fitted on the combined fits images using the `ASTROMETRY.NET` software¹. After fitting astrometric solutions, we used the 2MASS All-Sky Point Source Catalog for this region as input to the ‘sky2xy’ command² and obtained the image coordinates for further photometry. Photometry utilised `IRAF` routines making use of aperture photometry `PHOT` (Stetson, 1987) followed by psf photometry with `PSTSELECT`, `PSF`, & `ALLSTAR`.

2.2.1 Polarisation calculation

The measured magnitudes were converted to flux units for polarization calculations. After obtaining the intensity measurements of the stars at each position angle of the WGP, the polarimetric analysis was carried out using the Stokes method by applying

¹<http://nova.astrometry.net>

²part of the `wcstools` package

the formulae below (from source code of *linpol* task in IRAF):

$$I = \frac{F_0 + F_{45} + F_{90} + F_{135}}{4} \quad (2.1)$$

$$Q = \frac{F_0 - F_{90}}{2} \quad (2.2)$$

$$U = \frac{F_{45} - F_{135}}{2} \quad (2.3)$$

where F_0 , F_{45} , F_{90} and F_{135} are the fluxes at 0° , 45° , 90° and 135° position angles of the WGP.

Using the Stokes vectors, I, Q & U, we derived the degree of polarization (P) & position angle of polarization (θ), as formulated below:

$$P = \frac{\sqrt{Q^2 + U^2}}{I} \quad (2.4)$$

$$\theta = \frac{1}{2} \tan^{-1} \frac{U}{Q} \quad (2.5)$$

The error estimates for the P & θ were derived using the fundamental error propagation algorithms as (derivation is shown in [Appendix 2.5](#)):

$$\sigma_P = \frac{1}{I} \sqrt{\frac{Q^2 \sigma_Q^2 + U^2 \sigma_U^2}{Q^2 + U^2} + \frac{Q^2 + U^2}{I^2} \sigma_I^2} \quad (2.6)$$

$$\sigma_\theta = \frac{1}{2} \sqrt{\frac{Q^2 \sigma_U^2 + U^2 \sigma_Q^2}{(Q^2 + U^2)^2}} \text{ rad} \quad (2.7)$$

The resultant modulation curves for standard stars were then fitted with the following equation, theoretically derived from Mueller matrices for retarders,

$$I_j = \frac{1}{2} \{I_0 \pm Q \cos 2\theta_j \pm U \sin 2\theta_j\} \quad (2.8)$$

2.2.2 Polarisation calibration

The data are calibrated with observed polarization standards i.e. unpolarised & polarised standard stars. The unpolarised stars are used to account for any instrumental polarization, if present in the system. Since the NICSPol module is the first element after the telescope and before any asymmetric reflection in the instrument, we do not find any instrumental polarization. The observation of polarised standard stars allows for the conversion of our polarization position angles to celestial coordinates (Table 2.1). Several standards were observed in all filters (J, H, K_s) on the multiple nights of the observing runs. The standards were taken from the lists maintained by UKIRT³ & Nordic Optical Telescope⁴.

2.2.3 IR polarization values and large errors

From our analysis of the observational data, we have retained all the stars satisfying the criteria of $P/\sigma_P > 3$, and the degree of polarization $P < 30\%$. We have dropped sources with $P > 30\%$ since they were all faint or were at the edge of the circular field of NICSPol and the photometry would not be reliable. With this criteria, we present a data containing 69, 84 and 39 in J, H and K_s bands. Our coordinates were matched with Gaia2dis catalog (Bailer-Jones et al., 2018) published later which considered Bayesian approach for estimating distances from parallaxes. We also matched our data with 2MASS survey. A search radius of 2'' was used to match our coordinates with the surveys. The matched catalog with surveys had 56, 76 & 33 stars in the J, H and

³http://www.ukirt.hawaii.edu/instruments/irpol/irpol_stds.html#Unpolarized

⁴<http://www.not.iac.es/instruments/turpol/std/hpstd.html>

K_s bands respectively. We present a data set with larger degree of polarization than theoretically expected to arise from purely interstellar extinction at the IR wavelengths (Jones, 1989), for some of the stars. However, we note that at the individual source level, similar numbers are seen in the case of MIMIR (Clemens et al., 2020a) and SIRPOL (Hatano et al., 2013) data sets towards other directions. In the case of stars sitting in or towards reflection nebulae, one may see much higher degree of polarization (Jones, 1989). The large values may be attributed to a few observational limitations in our case: non-simultaneity of images at 4 angles, lower SNR and significant background for the K_s waveband (in particular) from the warm WGP. Of all these points, it appears that the varying infrared sky transmission between the multiple images (over the period of the observations of the 4 WGP angles) may be the most significant contributor to the uncertainty in the photometry in the individual frames. It has been mentioned by Simmons & Stewart (1985) that with low S/N, the derived polarization values tend to be overestimated. This would be especially applicable for the fainter stars. A correction has been suggested by them, for reducing the overestimated polarization values, expressed as

$$P_{corr} = \sqrt{(P_o^2) - \delta P^2} \quad (2.9)$$

where, P_o is the observed degree of polarization in our results. We considered the above correction and found that it did not make a significant change in our results and hence do not include this correction in the final tables and figures presented in this work.

2.3 Supplementary Data

2.3.1 2MASS & GAIA

The 2MASS & GAIA data have been used in this study to understand the variation of polarization with NIR color and with distances along the line of sight. The II/246/out,

2MASS All-Sky Catalog for Point Sources [Cutri et al. \(2003\)](#), has a total of 765 sources detected in the 10' search radius for the L1340 cloud. The photometric data from 2MASS has been utilised for studying the color and magnitude variation with polarization. In [Figure 2.1](#), we show the 2MASS colour-magnitude diagram(CMD) for all 2MASS stars in the region as a gray-scale. [Figure 2.2](#) represents the corresponding colour-colour diagram(CCD).

The Gaia DR2 data (Gaia2dis, catalog - I/347) [Bailer-Jones et al. \(2018\)](#) has been downloaded from the [Vizier⁵](#) database. The distance estimates from inverting the parallax has been dealt in a self-consistent manner in this data release, using a Bayesian Inference approach. A total of 975 Gaia sources were detected in the 10' search radius centered on LDN 1340. Of these, 678 sources are seen matched in both Gaia and 2MASS.

[Figure 2.3](#) uses this combined catalog to show the colour vs distance diagram for all the 2MASS and GAIA sources, again as a gray-scale. [Figure 2.6](#) shows the H band image (2MASS) of the field covered by our NICSPol observations in the equatorial coordinate system. The 2MASS image of the L1340 region was used after mosaicing of individual 2MASS tiles using `MONTAGE` tool. Our coverage of the field with NICSPol is incomplete due to the circular fields of the individual NICSPol tiles as discussed in the previous section. In all these [Figures \(2.1, 2.2, 2.3, 2.6\)](#), the individual stars measured for polarization are shown by separate symbols and will be discussed in the [Section 2.4](#).

2.3.2 WISE data

The WISE mission ([Wright et al., 2010](#)) maps the interstellar dust over the whole Galaxy. This is from the presence of PAH emission features in the W1 and W3 filters, 3.4 and 12 μm respectively. The other two filters, W2 and W4 (4.6 and 22 μm respectively) measure the continuum emission from the grains (small and large). We note that the 22 μm filter is expected to see both 'stochastic emission from small grains and the Wien tail of thermal emission from large grains' ([Wright et al., 2010](#)).

⁵<http://vizier.u-strasbg.fr/>

The WISE band images for the L1340 cloud at $3.4\ \mu\text{m}$, $4.6\ \mu\text{m}$, $12\ \mu\text{m}$ and $22\ \mu\text{m}$ were imported into ds9⁶ in RGB mode. The colour scaling and levels were chosen to bring out the dust features. This nebulosity is very nicely evident around the RNO 8 area (marked by a black circle in Figure 2.8) in the RGB colour-composite (with W2,W3 and W4 represented as blue, green and red colours). The $22\ \mu\text{m}$ band was also used to mark contours over the entire cloud (Figure 2.6), revealing the clumpy structure of the dust towards and in the L1340 region.

2.4 Results & Discussion

In the region covered by our NICSPol observations, we have 69, 84 and 39 stars in the J, H and K_s bands. We cross-identified the polarization measurements from these stars with the 2MASS & Gaia DR2 surveys to get a proper distance information and thence to characterize them. In total we have 56, 76 & 33 stars respectively in the J, H and K_s with 2MASS and Gaia counterparts. The cross-match of the different surveys was done in TOPCAT with the Sky algorithm, using a search radius of $2''$. This value in error is because of the pixel size defined in the 2MASS survey is $1''$. We had done a check over the data set of Gaia & 2MASS for shift in RA and Dec using histogram plot. The shift had spread till $0.5''$, with peak over zero shift. This reassured us to use the cross-match in TOPCAT with $2''$ error size. We find that 17 stars have NICSPol measurements in all the three bands (see Table 2.2). The estimated values of the degree of polarization (p) & polarization position angle (θ) with the 2MASS magnitudes and Gaia distances (*rest*) for all the stars are included in the Tables 2.5, 2.6, 2.7, individually for the J, H and K_s band observations.

⁶Data downloaded from <https://irsa.ipac.caltech.edu/Missions/wise.html>

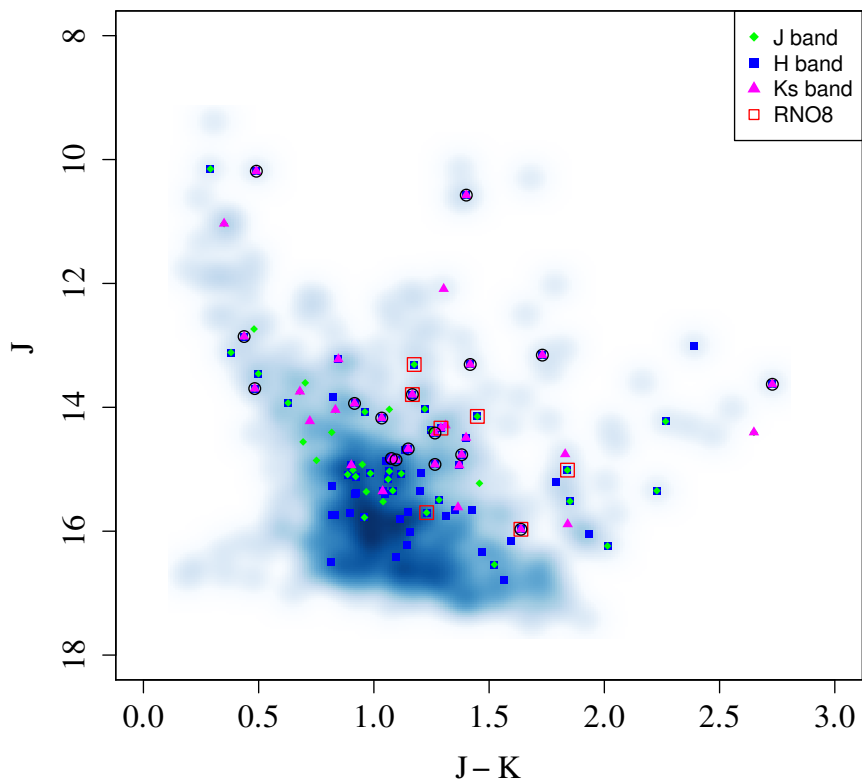


Figure 2.1: Color magnitude diagram for L1340 with the detection in different filter bands marked with different symbols. The black open circles mark the positions of stars measured with NICSPol in all three NIR bands. The open squares denote the stars towards the core of RNO 8 in this and all other figures.

Table 2.2: NICSPol linear polarization measurements of the 17 stars detected in all three J, H, Ks band (p_J, p_H, p_{K_s}) & polarization position angle (θ). The JHK magnitudes and distances to individual stars from 2MASS & Gaia survey data are compiled together.

RA (deg)	DEC (deg)	p_J (percent)	θ_J ($^\circ$)	p_H (percent)	θ_H ($^\circ$)	p_{K_s} (percent)	θ_{K_s} ($^\circ$)	Jmag (mag)	Hmag (mag)	Kmag (mag)	rest (pc)
37.63104	73.00655	24 ± 5	143 ± 5	13 ± 2	119 ± 5	21 ± 6	55 ± 7	15.97 ± 0.08	14.90 ± 0.06	14.33 ± 0.07	1090
37.54876	72.99906	23 ± 3	132 ± 4	13 ± 1	146 ± 3	20 ± 4	124 ± 5	14.85 ± 0.04	13.99 ± 0.04	13.75 ± 0.04	1110
37.57786	73.00077	13 ± 2	79 ± 5	11 ± 2	82 ± 4	29 ± 5	73 ± 5	14.83 ± 0.04	14.16 ± 0.04	13.75 ± 0.04	2212
37.55851	72.99121	23 ± 2	116 ± 3	7 ± 1	154 ± 5	15 ± 5	104 ± 8	14.92 ± 0.05	13.94 ± 0.04	13.66 ± 0.05	3164
37.74384	72.98866	7 ± 2	129 ± 9	6 ± 1	142 ± 6	13 ± 3	133 ± 6	14.77 ± 0.04	13.83 ± 0.04	13.38 ± 0.04	1494
37.76870	73.02041	13 ± 4	86 ± 6	6 ± 1	157 ± 6	16 ± 5	99 ± 9	14.67 ± 0.03	13.85 ± 0.03	13.52 ± 0.04	1154
37.72405	72.96484	7 ± 1	104 ± 4	9 ± 1	74 ± 3	28 ± 8	125 ± 8	14.17 ± 0.03	13.33 ± 0.03	13.14 ± 0.03	934
37.55281	72.97896	16 ± 3	97 ± 5	13 ± 1	129 ± 3	9 ± 3	128 ± 8	14.41 ± 0.03	13.44 ± 0.04	13.15 ± 0.03	2107
37.73381	72.98598	4 ± 1	112 ± 6	3 ± 1	128 ± 7	24 ± 4	129 ± 4	13.70 ± 0.03	13.25 ± 0.03	13.21 ± 0.03	819
37.83246	73.01491	6 ± 1	131 ± 8	11 ± 1	113 ± 4	14 ± 4	50 ± 9	13.94 ± 0.03	13.30 ± 0.04	13.02 ± 0.04	355
37.71886	72.99310	3 ± 0	86 ± 3	8 ± 1	148 ± 4	15 ± 4	128 ± 10	12.86 ± 0.03	12.52 ± 0.03	12.42 ± 0.02	736
37.67549	73.00384	4 ± 1	57 ± 7	10 ± 1	133 ± 5	12 ± 2	132 ± 4	13.79 ± 0.03	12.94 ± 0.03	12.63 ± 0.02	901
37.63532	72.98826	6 ± 1	57 ± 7	16 ± 1	94 ± 1	8 ± 1	104 ± 2	13.63 ± 0.03	12.23 ± 0.03	10.90 ± 0.02	5109
37.56753	72.99839	15 ± 1	124 ± 2	5 ± 1	134 ± 4	13 ± 2	88 ± 3	13.31 ± 0.03	12.34 ± 0.03	11.89 ± 0.02	3811
37.62266	73.02629	8 ± 1	107 ± 5	15 ± 1	79 ± 2	24 ± 2	99 ± 2	13.16 ± 0.03	11.92 ± 0.03	11.43 ± 0.02	3580
37.71638	72.99668	6 ± 1	106 ± 6	6 ± 0	145 ± 1	22 ± 1	133 ± 3	10.19 ± 0.03	9.77 ± 0.03	9.70 ± 0.02	232
37.92658	73.02211	8 ± 1	79 ± 3	9 ± 0	71 ± 1	10 ± 1	91 ± 3	10.57 ± 0.03	9.57 ± 0.03	9.17 ± 0.02	2300

Table 2.3: NICSPol linear polarization measurements (p_J, p_H, p_{K_s}) & polarization position angle (θ) of the RNO 8 stars. The JHK magnitudes and distances to individual stars from 2MASS & Gaia survey data are also included. The central star of RNO 8 (see section 2.4.3.3 for discussion) is shown in bold in this table.

RA	DEC	p_J	θ_J	p_H	θ_H	p_{K_s}	θ_{K_s}	Jmag	Hmag	Kmag	rest
(deg)	(deg)	(percent)	($^\circ$)	(percent)	($^\circ$)	(percent)	($^\circ$)	(mag)	(mag)	(mag)	(pc)
37.67549	73.00384	4 ± 1	57 ± 7	10 ± 1	133 ± 5	12 ± 2	132 ± 4	13.79 ± 0.03	12.94 ± 0.03	12.63 ± 0.02	901
37.65248	73.00647	14 ± 1	48 ± 2	4 ± 1	127 ± 7			14.15 ± 0.03	13.14 ± 0.03	12.70 ± 0.03	820
37.65338	72.99905	3 ± 1	48 ± 8	7 ± 1	122 ± 3			13.31 ± 0.03	12.51 ± 0.04	12.13 ± 0.03	898
37.60990	72.98741	25 ± 4	78 ± 5	5 ± 1	127 ± 7			15.01 ± 0.06	13.71 ± 0.05	13.17 ± 0.04	1358
37.65020	73.00396	15 ± 3	50 ± 6	13 ± 3	134 ± 5			15.70 ± 0.07	14.76 ± 0.07	14.47 ± 0.09	1034
37.63104	73.00655	24 ± 5	143 ± 5	13 ± 2	119 ± 5	21 ± 6	55 ± 7	15.97 ± 0.08	14.90 ± 0.06	14.33 ± 0.07	1090
37.64659	72.99383			9 ± 1	131 ± 4	8 ± 3	88 ± 6	14.34 ± 0.03	13.50 ± 0.03	13.04 ± 0.02	982
37.63532	72.98826	6 ± 1	57 ± 7	16 ± 1	94 ± 1	8 ± 1	104 ± 2	13.63 ± 0.03	12.23 ± 0.03	10.90 ± 0.02	5109

2.4.1 Color & distance information

The stars for which we have obtained polarimetric measurements have been marked with different symbols corresponding to different wavelengths in the CMD, see Figure 2.1. The grey scale density plot in this figure represents all of the 2MASS sources in a region of 10' search radius centered on L1340. Despite the irregular coverage due to the circular fields of the WGP, we see that a broad range of stellar types are covered and the measured stars represent, almost uniformly, all parts of the CMD.

The 2MASS two-colour diagram (CCD) is shown in Figure 2.2 as mentioned earlier. Here too we see that the measured stars cover all areas of the colour-colour space and there is no bias towards any specific part of the CCD indicating that the observed sample is a good representation of the region. Figure 2.3 shows the distribution of

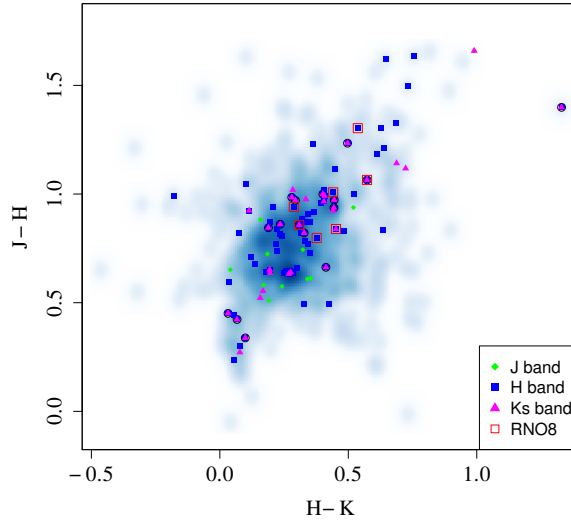


Figure 2.2: Color color diagram from 2MASS for L1340. Symbols are as in Figure 2.1.

the 2MASS colours and the corresponding Gaia distances. The distance to the cloud is quoted to be 825_{-80}^{+110} pc from the photometric and spectroscopic study of L1340 by [Kun et al. \(2016a\)](#). We show this by a dashed line in the figure. We see that this estimate is quite robust, since there is a sharp increase in the number of sources, along with a reddening in colour, beyond this distance.

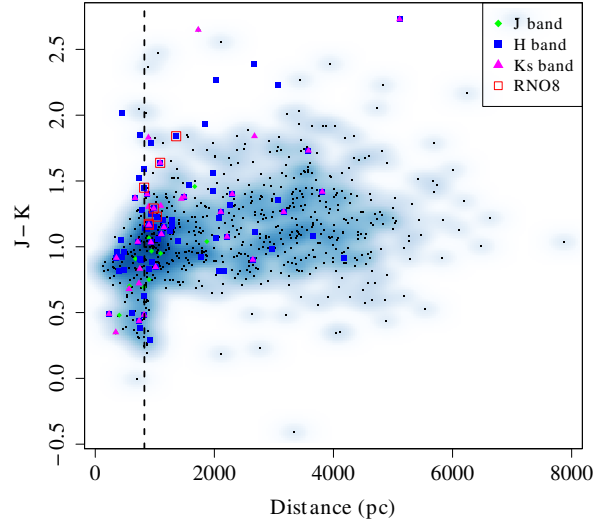


Figure 2.3: 2MASS $J - K_s$ colour vs Gaia distance. Different symbols show the stars for which polarization is measured. Stars of the RNO 8 area are shown as open squares. Vertical dashed line is at 825pc - the distance to the cloud as per [Kun et al. \(2016a\)](#).

2.4.2 NIR polarimetry

The polarization values are plotted as a function of the 2MASS H band photometry in Figure 2.4. The polarization values and the corresponding uncertainties for the fainter stars have been discussed in the section 2.2.3. To investigate the orientation of the magnetic field in the direction of the L1340 molecular cloud, we created linear polarization maps for the H wavelength band. The map in Figure 2.6 show a vector plot overlaying the polarization vectors (degree of polarization & position angle) for the H band on the 2MASS H filter image. The overall orientation of most of the polarization vectors is nearly aligned with the Galactic plane. There are large departures in some of the stars away from the nebulosity marked by the $22 \mu\text{m}$ WISE band 4 contours.

The mean values of the position angles in the 3 wavelength bands J, H, K_s are 100° , 116° , 135° respectively. These are tabulated in Table 2.4 with the mean degree of polarization for the three filter bands. They were derived from calculating the mean Q & U values

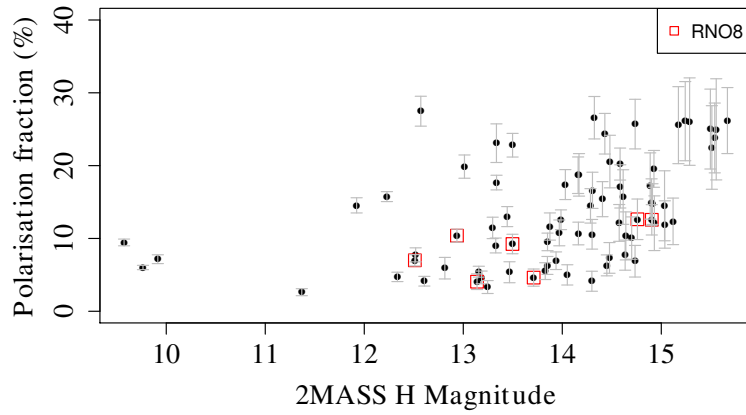


Figure 2.4: Polarisation in the H band as a function of the corresponding 2MASS H magnitudes.

for all the stars in the corresponding wavelength bands.

A histogram of the position angle for the three NIR bands is plotted in Figure 2.5. The vertical dashed line is for the mean value of the position angle from the gaussian fit applied over the histogram. We find that the resulting mean values are 97° , 107° & 101° in the J, H & K_s wavelengths. The dispersion in the position angles are consistent in the 3 bands with the values being 31° , 32° & 27° in the J, H & K_s respectively. Two dominant angles (PA= 130° and 70°) are seen in the H band histogram. These angles are marked in the position angle panels of Figure 2.9, 2.10 as horizontal lines. For the stars located at the distance of the L1340 cloud, there is a large scatter in the polarization position angle covering the extent of the two dominant angles. We have also plotted the varia-

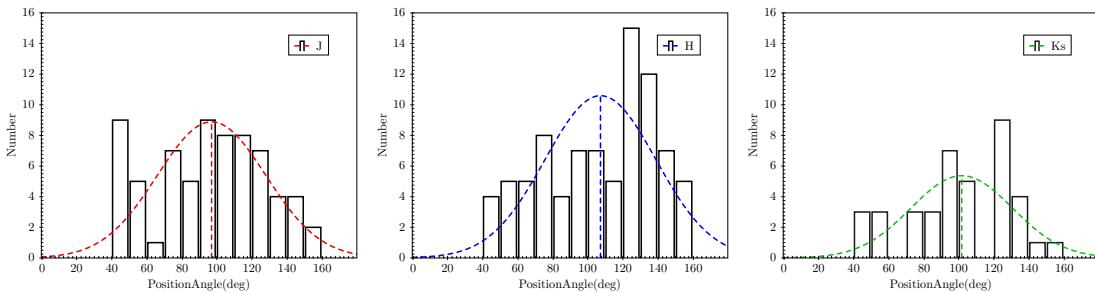


Figure 2.5: Position angle distribution in J, H and K_s bands. A gaussian fit is overlaid on each panel.

tion of degree of polarization with wavelength ($1.0 \mu\text{m} - 2.5 \mu\text{m}$) for the 17 stars (Table 2.2) which are detected in all the 3 wavelength bands (Figure 2.7). The values of the degree of polarization derived from the mean Q & U for all the stars in the data set, are

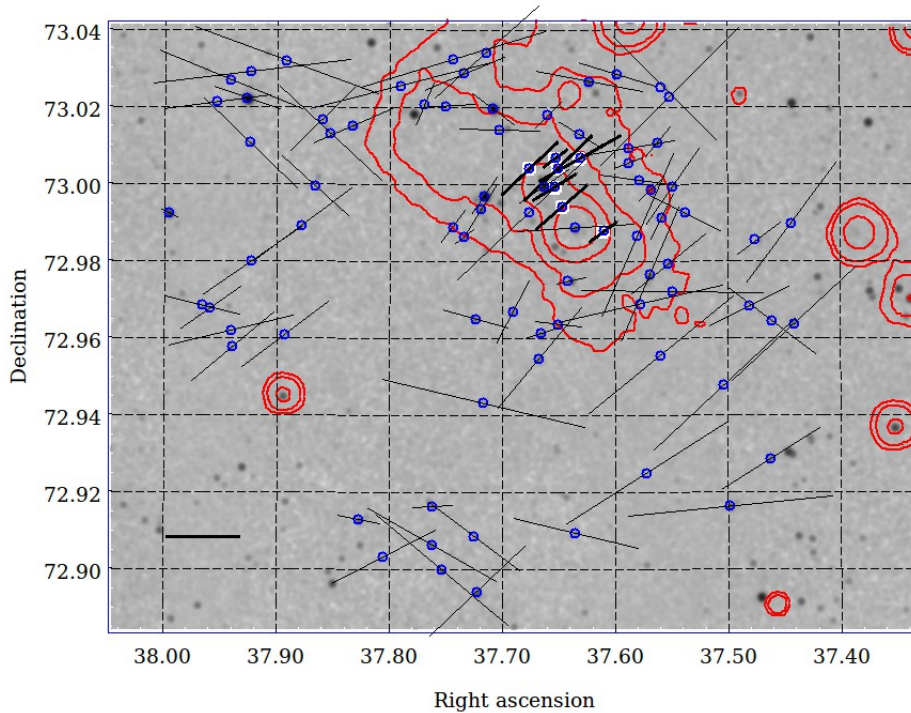


Figure 2.6: H band polarization vectors (thin solid lines) plotted on the H filter 2MASS image of L1340. The thick vectors are for stars corresponding to the RNO 8 area. The solid line at bottom left corner indicates a 10% degree of polarization value. The contours in red are from the WISE (band 4) image of the same area.

shown with a dotted line in this figure. There are a few cases where the K_s band polarization has gone up with correspondingly larger errors as compared to the J & H bands.

2.4.3 The RNO 8 cloud core

The Figures 2.6 & 2.8 show the RNO 8 stellar group between $\alpha = 37.60^\circ - 37.70^\circ$, $\delta = 72.98^\circ - 73.00^\circ$; $l = 130.12^\circ$ & $b = 11.51^\circ$. The position angles of this group around RNO 8 show a preferential direction along the Galactic plane, visible from their alignment nearly parallel to the grid lines in Figure 2.8, Table 2.3.

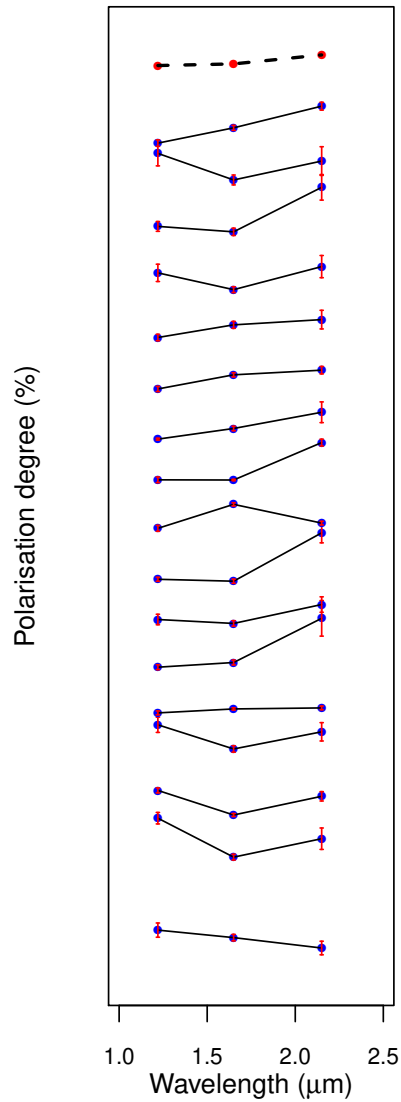


Figure 2.7: Wavelength dependence of NIR polarization towards LDN 1340. The dashed line at the top represents the polarization determined from mean Q and U of all stars (see text for further discussion).

2.4.3.1 Polarisation distribution with distance & colour

An indirect estimation for distances to the cloud can be devised from the polarimetric data. A uniform distribution of material along the line-of-sight will exhibit an increasing trend in extinction, from the relation $\langle A_v/L \rangle \approx 1.8 \text{ mag kpc}^{-1}$ (Whittet, 2005). The

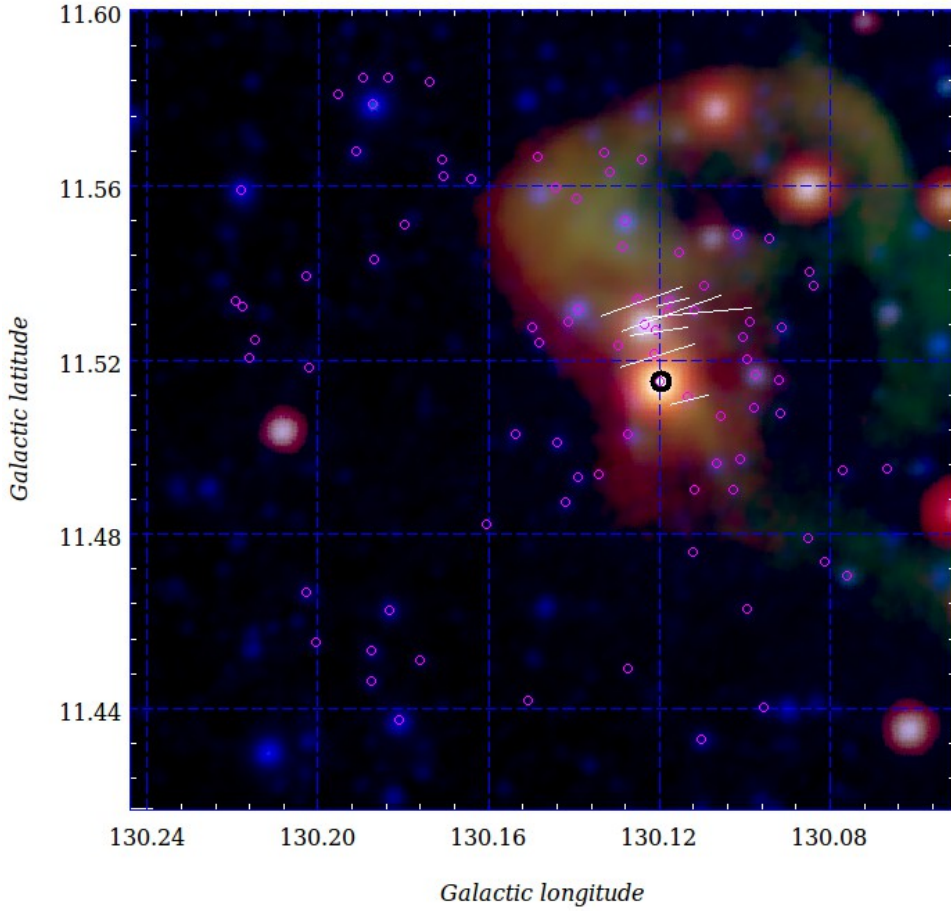


Figure 2.8: H band polarization vectors overlaid for the RNO 8 stars on the RGB colour composite of the WISE 4,3,2 bands. The black circle marks the core of RNO 8. Further discussion is in the text.

presence of a cloud, will enhance the number density of the material in the line-of-sight from which the background stellar light is passing. The starlight travelling through a medium will see a jump in the degree of polarization at the distance to the cloud (Eswaraiah et al., 2019). Looking at the lower panel in Figure 2.9, it seems that the stars part of RNO 8 (marked with red open squares) for which polarization is measured show an increase in degree of polarization with the distance in the cloud, assuming that the cloud starts just before the dotted line (at 825 pc) in the figure. These stars also have consistent angles, with very small dispersion, as seen in the upper panel of the Figure 2.9. We interpret this to mean that within the RNO 8 cloud core the magnetic field orientation remains uniform. In Fig 2.10, we have plotted the 2MASS $J - K_s$ colour vs degree of polarization in the lower panel. The upper panel shows the variation of position angle. We see that the stars in RNO 8 (marked by red open squares) do

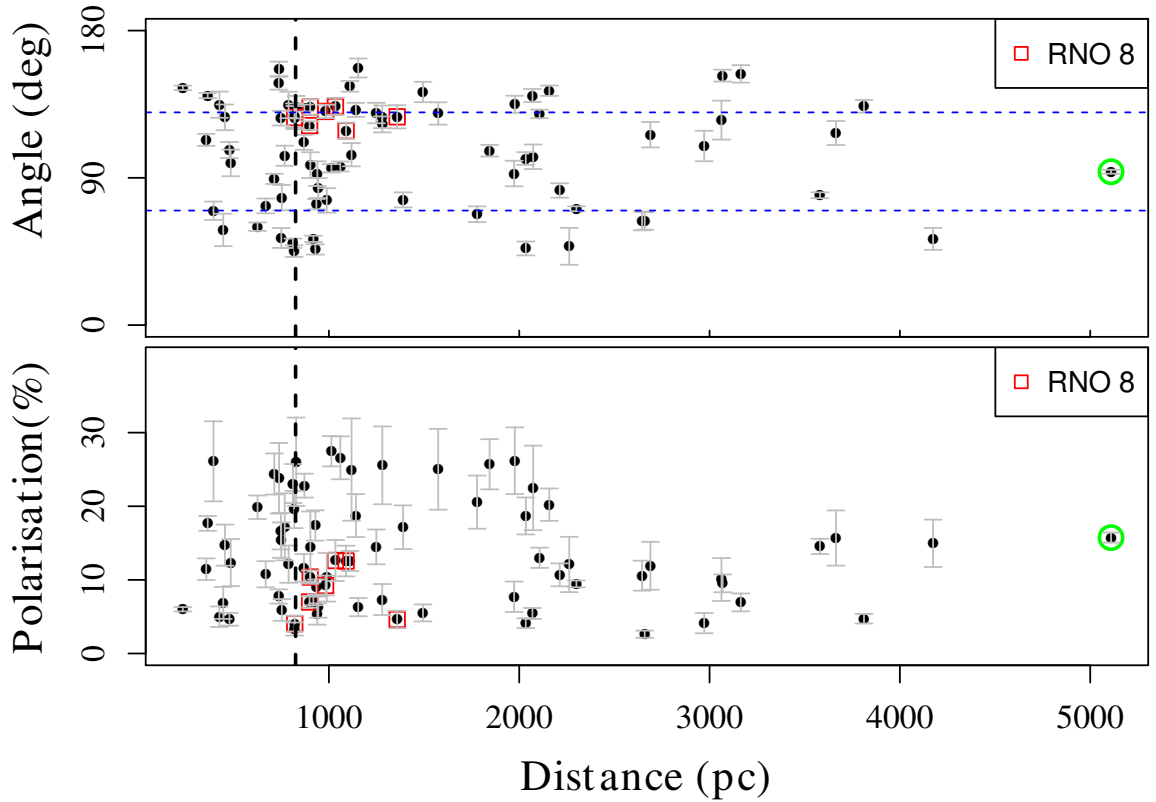


Figure 2.9: Distance (in pc from Gaia) vs polarization percentage (lower panel) and polarization position angle (upper panel) for H band measurements. Stars in the vicinity of RNO 8 are shown with larger symbols. The central star of RNO 8 is shown with a green open circle.

not show significant variation in the angle of polarization over a large range in colour. These stars must be pre-main sequence stars as identified in the work by [Kun et al. \(2016a\)](#). Since we do not see much variation in position angle for these stars it appears that they do not affect the overall magnetic field orientation despite being embedded in dust.

2.4.3.2 Q-U plot

Our normalized q-u plot (see [Figure 2.11](#)) shows a concentration of stars near the origin, with a little spread present within a value ranging between -0.5 to 0.5 in both axes. We note that stars surrounding the RNO 8 region (see [Figure 2.8](#)) are also clustered together in the q-u plot suggesting that they are physically associated with the RNO 8 cloud

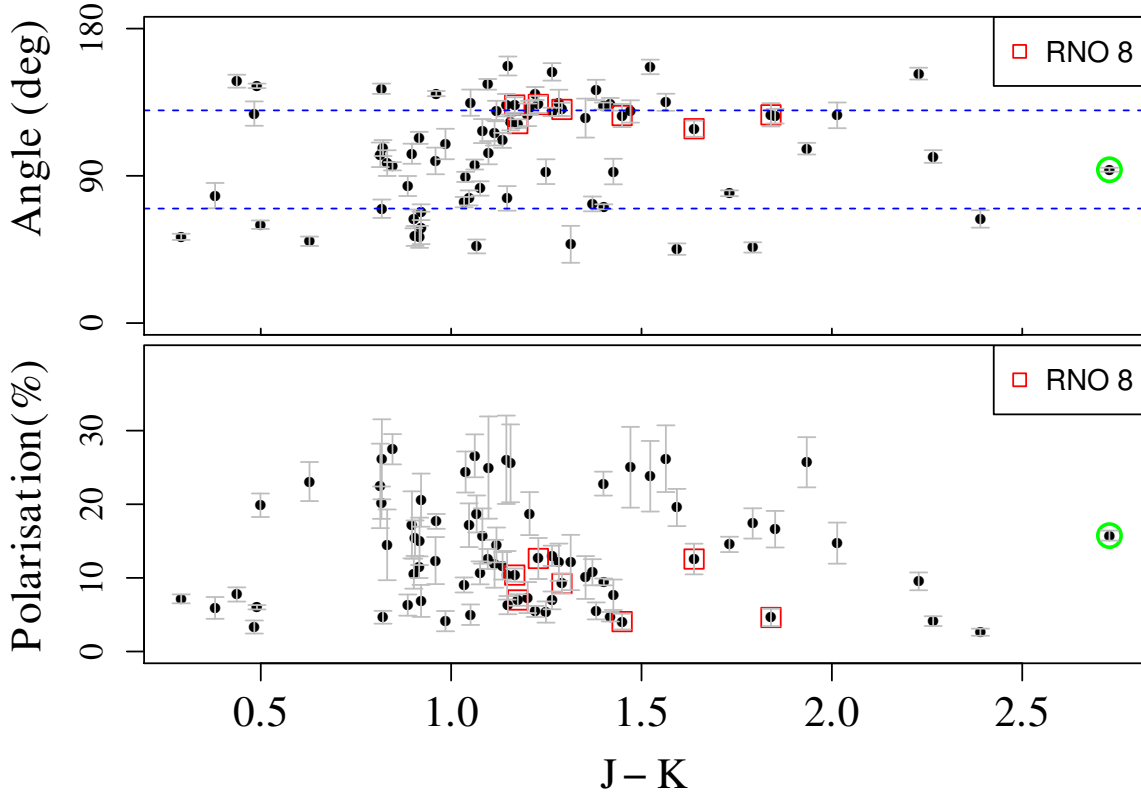


Figure 2.10: Polarisation in the H band (percentage in lower panel and angle in upper panel) vs $J - K_s$ colour (from 2MASS). The symbols are as in Figure 2.9.

core.

2.4.3.3 Central star of RNO 8

The star identified by [Kun et al. \(2016a\)](#) at the core of the RNO 8 nebulosity ($\alpha = 37.635$ & $\delta = 72.988$) is seen in Figure 2.9 (marked with green open circle) at a distance of 5 kpc. This star is at the centre of the bright WISE core marked with black circle in the Figure 2.8. This star does not show the same position angle of polarization as seen for the other stars surrounding it. The Gaia DR2 documentation includes a 'renormalised unit weight error' $ruwe$ parameter, whose threshold value for reliable astrometry is 1.4. The central star has $ruwe = 7.1$, which makes the data unreliable for this star. The uncertainty in the distance estimate also showed $r_{lo} = 3694$ pc, and $r_{hi} = 7064$ pc, for the star, which are large. For this star, and its neighbours, we also looked at the Gaia Data Release 2 catalog and the corresponding Gaia colour, $B_p - R_p = 1$, is a lot bluer than

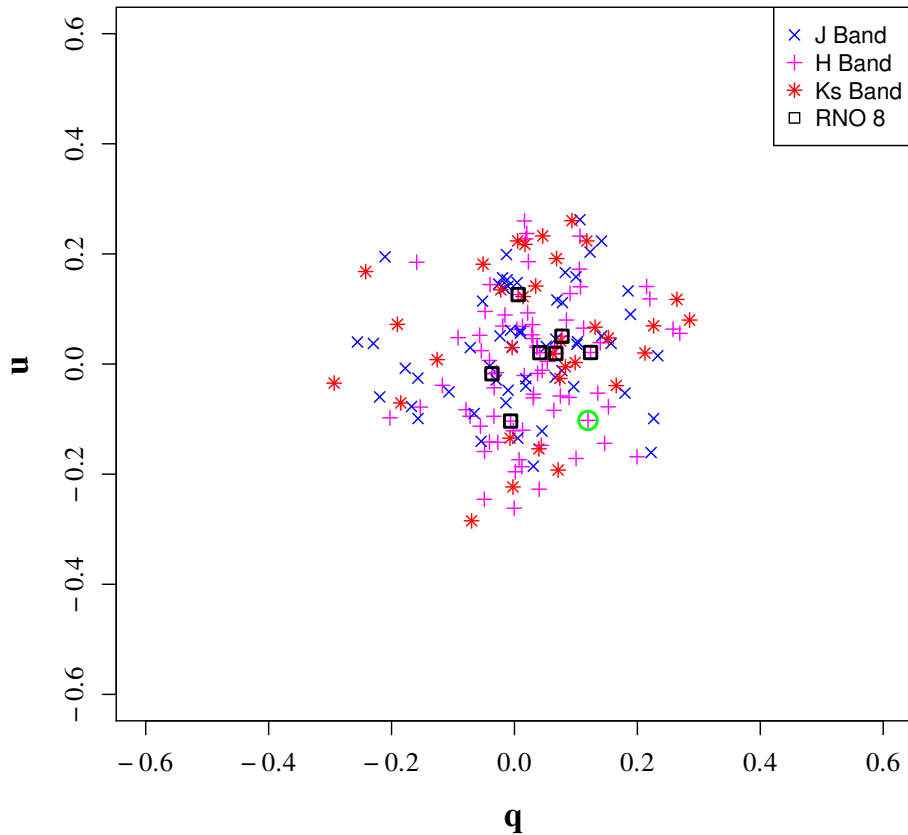


Figure 2.11: Normalized q - u plot for all the stars with measured polarization in L1340. Different symbols mark the respective filter detections. Stars part of the RNO 8 core are shown as open squares. The green open circle corresponds to the star discussed in section 2.4.3.3.

the colours for the other stars around it, while the $J-K_s$ is very red (> 2.5) (Figure 2.10). The star is also marked (green open circle) in the Figure 2.11. It is distinctly seen as displaced from the RNO 8 stars.

2.4.3.4 Estimation of magnetic field

The plane of the sky magnetic field can be calculated from the inclusion of polarimetric observations in addition to other parameters known from photometric data. The magnetic field strength as formulated by Chandrasekhar and Fermi (CF model) (Chandrasekhar & Fermi, 1953), depends on the mean local density of the cloud ρ ,

Table 2.4: The mean values of degree of polarization (P) & position angle (PA) for the measurements of all stars in J, H, K_s filter bands in the region of L1340.

Filter Band	Mean degree of polarization	Mean PA
J	2.8	100
H	3.5	117
Ks	7.3	135

the line-of-sight velocity dispersion δv and the dispersion in the position angle of polarization $\delta\theta$. The equation can be expressed as,

$$B_p = Q \sqrt{4\pi\rho} \frac{\delta v_{\text{los}}}{\delta\theta} \quad (2.10)$$

[Ostriker et al. \(2001\)](#) has performed numerical simulations for the estimation of magnetic field strength and compared it with the CF model. Based upon their results, they suggested a value $Q \sim 0.5$, for angle dispersion $< 25^\circ$. The values for $n(\text{H}_2)$ and velocity dispersion based upon the observations of C^{18}O from the earlier work of [Kun et al. \(1994\)](#) on this cloud will be used. They have quoted velocity dispersion and mean cloud density for three cores A, B and C within the L1340. Based upon the RNO 8 coordinates, we use the numbers for core B of the cloud, which contains the RNO 8 cluster. The estimated value for $n(\text{H}_2) = 830 \text{ cm}^{-3}$, and $\Delta v = 0.9 \text{ km s}^{-1}$. Using these values with our position angle dispersion of 5.17° , the \vec{B} strength in the plane of sky is calculated as $\approx 42 \mu\text{G}$ for the RNO 8 core. This value is in accordance with the magnetic field strength $\sim 20 - 200 \mu\text{G}$ in other molecular clouds ([Kwon et al., 2016](#)). The effect of the magnetic field strength can be seen from the aligned polarization vectors in Fig. 2.8 for the region.

If we consider the star in the direction of the center of RNO 8 core to be part of the cloud complex, the dispersion in the polarization position angle increases to 12° . From the equation 2.10, the calculated \vec{B} strength is found to be $18 \mu\text{G}$. In such a case, the mean magnetic field strength is decreased with the increase in the dispersion of the magnetic field vector direction due to varying cloud structure (or multiple clouds) in the line of sight giving rise to different position angles in polarization. The consequences of this

dispersion in the magnetic field direction has been discussed in [Ostriker et al. \(2001\)](#).

2.5 Conclusions

Near-Infrared polarization in the J, H, K_s bands over the L1340 molecular cloud has been presented for a field of $9.6' \times 9.6'$ using PRL's 1.2 m telescope with the NIC-SPol instrument. We conclude with a few important results for the RNO 8 region in particular.

1. NIR polarimetry was performed on a region within L1340, and measurements for a total of 56, 76 and 33 stars are reported in the J, H, & K_s bands for the first time, along with their 2MASS photometry and Gaia distance where available.
2. The distribution of the position angle of polarization is very consistent and are almost aligned with the Galactic magnetic field, which implies that the dichroic extinction is causing the polarization due to the dust grains which are aligned with the magnetic field permeating the galaxy.
3. The magnetic field strength for the RNO 8 region within the L1340 cloud was estimated without including the central star, using the Chandrasekhar-Fermi method. A $42 \mu\text{G}$ magnetic field was estimated which is similar to the strength present in such areas.
4. The central star in the RNO 8 is shown by Gaia to be at a strikingly different distance compared to the other stars around it. It is also seen that the position angle for this star differs significantly from other stars and the distance estimated from Gaia is 5 kpc. The rest of the stars are at a distance of 800-1300 pc. Considering this star as part of the RNO 8, reduces the magnetic field strength $\sim 18 \mu\text{G}$, due to the increase in position angle dispersion.

Table 2.5: Estimated values of linear polarization for 56 stars detected in the J band (p_J) and polarization position angle (θ). Additional columns contain the JHK magnitudes with errors from 2MASS and distances from the Gaia survey.

RA (J2000) (deg)	DEC (J2000) (deg)	p_J (percent)	θ ($^\circ$)	J (mag)	H (mag)	K (mag)	rest (pc)
37.84206	72.90256	20 ± 5	47 ± 8	15.02 ± 0.03	14.29 ± 0.04	14.11 ± 0.05	674
37.85020	72.89613	14 ± 2	118 ± 4	12.74 ± 0.03	12.29 ± 0.03	12.26 ± 0.02	403
37.80581	72.90274	29 ± 9	69 ± 8	15.35 ± 0.04	14.62 ± 0.07	14.26 ± 0.07	3664
37.82709	72.91257	6 ± 1	130 ± 6	13.12 ± 0.03	12.81 ± 0.03	12.73 ± 0.03	752
37.82650	72.90609	13 ± 4	57 ± 7	14.56 ± 0.04	13.91 ± 0.04	13.87 ± 0.05	816
37.76254	72.90605	15 ± 1	158 ± 2	13.46 ± 0.03	13.01 ± 0.03	12.96 ± 0.03	625
37.75398	72.89944	26 ± 2	119 ± 2	13.93 ± 0.03	13.34 ± 0.03	13.30 ± 0.04	811
37.76584	72.91756	26 ± 5	110 ± 7	15.36 ± 0.05	14.75 ± 0.06	14.40 ± 0.07	945
37.76202	72.91622	8 ± 2	86 ± 5	14.37 ± 0.04	13.47 ± 0.03	13.12 ± 0.04	939
37.66704	72.95444	4 ± 1	117 ± 8	14.07 ± 0.03	13.34 ± 0.04	13.11 ± 0.03	363
37.63890	72.97472	14 ± 1	47 ± 5	14.23 ± 0.03	12.61 ± 0.03	11.96 ± 0.02	2034
37.65085	72.96326	21 ± 3	127 ± 4	15.09 ± 0.05	14.45 ± 0.06	14.20 ± 0.06	944
37.55281	72.97896	16 ± 3	97 ± 5	14.41 ± 0.03	13.44 ± 0.04	13.15 ± 0.03	2107
37.55851	72.99121	23 ± 2	116 ± 3	14.92 ± 0.05	13.94 ± 0.04	13.66 ± 0.05	3164
37.56753	72.99839	15 ± 1	124 ± 2	13.31 ± 0.03	12.34 ± 0.03	11.89 ± 0.02	3811

Continued on next page

Table 2.5 – Continued from previous page

RA (J2000) (deg)	DEC (J2000) (deg)	p_J (percent)	θ ($^\circ$)	J (mag)	H (mag)	K (mag)	rest (pc)
37.57937	72.98655	27 ± 5	96 ± 5	16.54 ± 0.13	15.54 ± 0.11	15.02 ± 0.12	738
37.54876	72.99906	23 ± 3	132 ± 4	14.85 ± 0.04	13.99 ± 0.04	13.75 ± 0.04	1110
37.89303	72.91765	13 ± 3	46 ± 6	14.40 ± 0.03	13.83 ± 0.03	13.59 ± 0.03	403
37.87937	72.92706	19 ± 3	146 ± 4	14.86 ± 0.04	14.28 ± 0.04	14.11 ± 0.05	902
37.89399	72.94469	15 ± 5	47 ± 5	14.40 ± 0.04	12.74 ± 0.04	11.76 ± 0.02	1729
37.89349	72.96078	19 ± 4	130 ± 6	16.24 ± 0.09	14.91 ± 0.08	14.22 ± 0.07	453
37.93992	72.95743	11 ± 3	100 ± 11	15.07 ± 0.05	14.29 ± 0.04	13.95 ± 0.05	1249
37.87789	72.98929	11 ± 2	117 ± 6	15.52 ± 0.04	14.30 ± 0.03	13.67 ± 0.04	747
37.94118	73.02691	18 ± 4	91 ± 6	15.12 ± 0.04	14.48 ± 0.05	14.20 ± 0.06	1778
37.92658	73.02211	8 ± 1	79 ± 3	10.57 ± 0.03	9.57 ± 0.03	9.17 ± 0.02	2300
37.69065	72.96668	15 ± 3	148 ± 5	15.35 ± 0.06	13.85 ± 0.04	13.12 ± 0.04	3068
37.72405	72.96484	7 ± 1	104 ± 4	14.17 ± 0.03	13.33 ± 0.03	13.14 ± 0.03	934
37.71439	72.98301	19 ± 2	82 ± 3	14.92 ± 0.04	14.31 ± 0.06	13.97 ± 0.05	1097
37.74384	72.98866	7 ± 2	129 ± 9	14.77 ± 0.04	13.83 ± 0.04	13.38 ± 0.04	1494
37.73381	72.98598	4 ± 1	112 ± 6	13.70 ± 0.03	13.25 ± 0.03	13.21 ± 0.03	819
37.65339	72.98377	6 ± 1	72 ± 5	13.74 ± 0.03	13.22 ± 0.04	13.07 ± 0.03	567
37.64557	72.98241	11 ± 3	125 ± 8	15.23 ± 0.04	14.29 ± 0.05	13.77 ± 0.04	1670

Continued on next page

Table 2.5 – Continued from previous page

RA (J2000) (deg)	DEC (J2000) (deg)	p_J (percent)	θ ($^\circ$)	J (mag)	H (mag)	K (mag)	rest (pc)
37.63532	72.98826	6 ± 1	57 ± 7	13.63 ± 0.03	12.23 ± 0.03	10.90 ± 0.02	5109
37.60990	72.98741	25 ± 4	78 ± 5	15.01 ± 0.06	13.71 ± 0.05	13.17 ± 0.04	1358
37.65020	73.00396	15 ± 3	50 ± 6	15.70 ± 0.07	14.76 ± 0.07	14.47 ± 0.09	1034
37.65248	73.00647	14 ± 1	48 ± 2	14.15 ± 0.03	13.14 ± 0.03	12.70 ± 0.03	820
37.65338	72.99905	3 ± 1	48 ± 8	13.31 ± 0.03	12.51 ± 0.04	12.13 ± 0.03	898
37.71638	72.99668	6 ± 1	106 ± 6	10.19 ± 0.03	9.77 ± 0.03	9.70 ± 0.02	232
37.70193	72.99508	19 ± 3	74 ± 4	14.03 ± 0.03	13.29 ± 0.03	12.97 ± 0.02	901
37.71886	72.99310	3 ± 0	86 ± 3	12.86 ± 0.03	12.52 ± 0.03	12.42 ± 0.02	736
37.67549	73.00384	4 ± 1	57 ± 7	13.79 ± 0.03	12.94 ± 0.03	12.63 ± 0.02	901
37.70818	73.01942	23 ± 4	98 ± 4	10.15 ± 0.03	9.91 ± 0.03	9.86 ± 0.02	918
37.85284	73.01300	12 ± 3	103 ± 8	15.03 ± 0.04	14.16 ± 0.04	13.97 ± 0.05	2034
37.85967	73.01648	14 ± 3	120 ± 7	15.49 ± 0.07	14.57 ± 0.07	14.21 ± 0.07	788
37.83246	73.01491	6 ± 1	131 ± 8	13.94 ± 0.03	13.30 ± 0.04	13.02 ± 0.04	355
37.92304	73.02894	16 ± 3	95 ± 5	15.16 ± 0.04	14.32 ± 0.04	14.10 ± 0.06	1060
37.90825	73.03417	23 ± 6	85 ± 5	15.52 ± 0.07	14.64 ± 0.06	14.48 ± 0.07	1873
37.77859	73.01794	5 ± 1	129 ± 4	11.03 ± 0.03	10.76 ± 0.03	10.68 ± 0.02	344
37.75813	73.03537	18 ± 2	102 ± 3	13.61 ± 0.03	13.09 ± 0.03	12.90 ± 0.03	573

Continued on next page

Table 2.5 – *Continued from previous page*

RA (J2000) (deg)	DEC (J2000) (deg)	p_J (percent)	θ ($^\circ$)	J (mag)	H (mag)	K (mag)	rest (pc)
37.57786	73.00077	13 ± 2	79 ± 5	14.83 ± 0.04	14.16 ± 0.04	13.75 ± 0.04	2212
37.58790	73.00518	16 ± 3	49 ± 6	15.07 ± 0.05	14.30 ± 0.04	14.08 ± 0.05	2971
37.58771	73.00910	19 ± 5	143 ± 8	15.78 ± 0.07	15.12 ± 0.07	14.82 ± 0.10	484
37.63104	73.00655	24 ± 5	143 ± 5	15.97 ± 0.08	14.90 ± 0.06	14.33 ± 0.07	1090
37.56222	73.01055	28 ± 5	124 ± 5	14.03 ± 0.03	13.16 ± 0.03	12.81 ± 0.03	2069
37.61727	73.02386	10 ± 3	78 ± 7	14.04 ± 0.03	13.40 ± 0.05	13.21 ± 0.04	748
37.62266	73.02629	8 ± 1	107 ± 5	13.16 ± 0.03	11.92 ± 0.03	11.43 ± 0.02	3580

Table 2.6: Estimated values of linear polarization for 76 stars detected in the H band (p_H), polarization position angle (θ). Additional columns are the JHK magnitudes and errors from 2MASS & distances from Gaia survey.

RA (J2000) (deg)	DEC (J2000) (deg)	p_H (percent)	θ ($^\circ$)	J (mag)	H (mag)	K (mag)	rest (pc)
37.80581	72.90274	16 ± 4	117 ± 7	15.35 ± 0.04	14.62 ± 0.07	14.26 ± 0.07	3664
37.82709	72.91257	6 ± 1	78 ± 8	13.12 ± 0.03	12.81 ± 0.03	12.73 ± 0.03	752
37.76254	72.90605	20 ± 2	60 ± 3	13.46 ± 0.03	13.01 ± 0.03	12.96 ± 0.03	625
37.75398	72.89944	23 ± 3	50 ± 3	13.93 ± 0.03	13.34 ± 0.03	13.30 ± 0.04	811
37.76202	72.91622	5 ± 1	93 ± 8	14.37 ± 0.04	13.47 ± 0.03	13.12 ± 0.04	939
37.72523	72.90851	15 ± 2	53 ± 6	15.05 ± 0.05	14.41 ± 0.05	14.15 ± 0.07	749
37.49817	72.91608	27 ± 2	96 ± 3	13.22 ± 0.03	12.57 ± 0.03	12.38 ± 0.02	1013
37.63488	72.90934	17 ± 3	77 ± 5	15.39 ± 0.06	14.59 ± 0.07	14.35 ± 0.06	1389
37.66558	72.96096	5 ± 1	107 ± 5	13.83 ± 0.03	13.19 ± 0.03	13.01 ± 0.03	477
37.66704	72.95444	18 ± 1	140 ± 2	14.07 ± 0.03	13.34 ± 0.04	13.11 ± 0.03	363
37.57250	72.92450	26 ± 5	123 ± 5	16.01 ± 0.08	15.17 ± 0.08	14.86 ± 0.11	1280
37.56031	72.95492	25 ± 5	129 ± 7	16.33 ± 0.11	15.50 ± 0.11	14.86 ± 0.11	1574
37.63890	72.97472	4 ± 1	102 ± 4	14.23 ± 0.03	12.61 ± 0.03	11.96 ± 0.02	2034
37.65085	72.96326	6 ± 1	84 ± 6	15.09 ± 0.05	14.45 ± 0.06	14.20 ± 0.06	944
37.57782	72.96870	22 ± 6	103 ± 8	16.50 ± 0.11	15.51 ± 0.11	15.69 ± 0.22	2073

Continued on next page

Table 2.6 – Continued from previous page

RA (J2000) (deg)	DEC (J2000) (deg)	p_H (percent)	θ ($^\circ$)	J (mag)	H (mag)	K (mag)	rest (pc)
37.50386	72.94773	26 ± 6	133 ± 7	16.23 ± 0.09	15.29 ± 0.09	15.08 ± 0.12	827
37.44123	72.96358	23 ± 2	133 ± 2	14.49 ± 0.04	13.50 ± 0.03	13.09 ± 0.03	871
37.46095	72.96443	15 ± 3	53 ± 7	15.40 ± 0.06	14.90 ± 0.07	14.48 ± 0.07	4174
37.48141	72.96781	12 ± 3	116 ± 8	15.81 ± 0.06	15.04 ± 0.08	14.69 ± 0.08	2689
37.54910	72.97186	24 ± 3	89 ± 3	15.35 ± 0.04	14.43 ± 0.06	14.32 ± 0.06	713
37.55281	72.97896	13 ± 1	129 ± 3	14.41 ± 0.03	13.44 ± 0.04	13.15 ± 0.03	2107
37.55851	72.99121	7 ± 1	154 ± 5	14.92 ± 0.05	13.94 ± 0.04	13.66 ± 0.05	3164
37.56753	72.99839	5 ± 1	134 ± 4	13.31 ± 0.03	12.34 ± 0.03	11.89 ± 0.02	3811
37.57937	72.98655	24 ± 5	157 ± 4	16.54 ± 0.13	15.54 ± 0.11	15.02 ± 0.12	738
37.53776	72.99233	11 ± 2	64 ± 6	14.93 ± 0.05	14.30 ± 0.06	14.03 ± 0.06	2645
37.54876	72.99906	13 ± 1	146 ± 3	14.85 ± 0.04	13.99 ± 0.04	13.75 ± 0.04	1110
37.47221	72.98537	7 ± 2	127 ± 7	15.35 ± 0.04	14.48 ± 0.06	14.15 ± 0.05	1280
37.44314	72.98964	20 ± 2	143 ± 3	15.26 ± 0.05	14.58 ± 0.05	14.45 ± 0.07	2158
37.89349	72.96078	15 ± 3	127 ± 8	16.24 ± 0.09	14.91 ± 0.08	14.22 ± 0.07	453
37.93992	72.95743	14 ± 2	130 ± 6	15.07 ± 0.05	14.29 ± 0.04	13.95 ± 0.05	1249
37.95973	72.96766	10 ± 3	125 ± 12	15.66 ± 0.08	14.70 ± 0.08	14.31 ± 0.06	3062
37.94084	72.96166	17 ± 5	104 ± 6	15.71 ± 0.06	14.89 ± 0.07	14.81 ± 0.09	767

Continued on next page

Table 2.6 – Continued from previous page

RA (J2000) (deg)	DEC (J2000) (deg)	p_H (percent)	θ ($^\circ$)	J (mag)	H (mag)	K (mag)	rest (pc)
37.96600	72.96832	10 ± 3	76 ± 8	15.69 ± 0.07	14.64 ± 0.06	14.54 ± 0.08	988
37.99590	72.99227	3 ± 0	64 ± 5	13.01 ± 0.03	11.37 ± 0.03	10.62 ± 0.02	2659
37.87789	72.98929	17 ± 2	126 ± 4	15.52 ± 0.04	14.30 ± 0.03	13.67 ± 0.04	747
37.92366	73.01052	17 ± 2	46 ± 3	15.21 ± 0.04	14.03 ± 0.04	13.42 ± 0.04	928
37.95379	73.02107	14 ± 5	98 ± 8	15.74 ± 0.08	15.03 ± 0.08	14.91 ± 0.11	902
37.94118	73.02691	21 ± 4	68 ± 5	15.12 ± 0.04	14.48 ± 0.05	14.20 ± 0.06	1778
37.92658	73.02211	9 ± 0	71 ± 1	10.57 ± 0.03	9.57 ± 0.03	9.17 ± 0.02	2300
37.69065	72.96668	10 ± 1	152 ± 4	15.35 ± 0.06	13.85 ± 0.04	13.12 ± 0.04	3068
37.72405	72.96484	9 ± 1	74 ± 3	14.17 ± 0.03	13.33 ± 0.03	13.14 ± 0.03	934
37.74384	72.98866	6 ± 1	142 ± 6	14.77 ± 0.04	13.83 ± 0.04	13.38 ± 0.04	1494
37.73381	72.98598	3 ± 1	128 ± 7	13.70 ± 0.03	13.25 ± 0.03	13.21 ± 0.03	819
37.63532	72.98826	16 ± 1	94 ± 1	13.63 ± 0.03	12.23 ± 0.03	10.90 ± 0.02	5109
37.60990	72.98741	5 ± 1	127 ± 7	15.01 ± 0.06	13.71 ± 0.05	13.17 ± 0.04	1358
37.64659	72.99383	9 ± 1	131 ± 4	14.34 ± 0.03	13.50 ± 0.03	13.04 ± 0.02	982
37.65020	73.00396	13 ± 3	134 ± 5	15.70 ± 0.07	14.76 ± 0.07	14.47 ± 0.09	1034
37.65248	73.00647	4 ± 1	127 ± 7	14.15 ± 0.03	13.14 ± 0.03	12.70 ± 0.03	820
37.65338	72.99905	7 ± 1	122 ± 3	13.31 ± 0.03	12.51 ± 0.04	12.13 ± 0.03	898

Continued on next page

Table 2.6 – Continued from previous page

RA (J2000) (deg)	DEC (J2000) (deg)	p_H (percent)	θ ($^\circ$)	J (mag)	H (mag)	K (mag)	rest (pc)
37.71638	72.99668	6 ± 0	145 ± 1	10.19 ± 0.03	9.77 ± 0.03	9.70 ± 0.02	232
37.71886	72.99310	8 ± 1	148 ± 4	12.86 ± 0.03	12.52 ± 0.03	12.42 ± 0.02	736
37.67549	73.00384	10 ± 1	133 ± 5	13.79 ± 0.03	12.94 ± 0.03	12.63 ± 0.02	901
37.70818	73.01942	7 ± 1	53 ± 2	10.15 ± 0.03	9.91 ± 0.03	9.86 ± 0.02	918
37.86635	72.99945	12 ± 4	48 ± 11	15.76 ± 0.08	14.93 ± 0.07	14.45 ± 0.07	2263
37.85284	73.01300	19 ± 3	47 ± 4	15.03 ± 0.04	14.16 ± 0.04	13.97 ± 0.05	2034
37.85967	73.01648	12 ± 3	135 ± 8	15.49 ± 0.07	14.57 ± 0.07	14.21 ± 0.07	788
37.83246	73.01491	11 ± 1	113 ± 4	13.94 ± 0.03	13.30 ± 0.04	13.02 ± 0.04	355
37.89152	73.03192	26 ± 5	70 ± 6	15.73 ± 0.07	15.24 ± 0.08	14.92 ± 0.11	393
37.92304	73.02894	27 ± 3	97 ± 3	15.16 ± 0.04	14.32 ± 0.04	14.10 ± 0.06	1060
37.74975	73.01993	8 ± 2	93 ± 8	15.65 ± 0.06	14.63 ± 0.07	14.23 ± 0.06	1973
37.76870	73.02041	6 ± 1	157 ± 6	14.67 ± 0.03	13.85 ± 0.03	13.52 ± 0.04	1154
37.79042	73.02529	25 ± 7	104 ± 7	16.41 ± 0.11	15.55 ± 0.11	15.32 ± 0.15	1119
37.71368	73.03387	19 ± 3	132 ± 4	15.05 ± 0.04	14.17 ± 0.04	13.85 ± 0.05	1141
37.74331	73.03214	26 ± 3	107 ± 4	16.04 ± 0.08	14.74 ± 0.06	14.11 ± 0.05	1844
37.73367	73.02836	12 ± 2	112 ± 5	14.69 ± 0.05	13.88 ± 0.04	13.56 ± 0.04	869
37.57786	73.00077	11 ± 2	82 ± 4	14.83 ± 0.04	14.16 ± 0.04	13.75 ± 0.04	2212

Continued on next page

Table 2.6 – *Continued from previous page*

RA (J2000) (deg)	DEC (J2000) (deg)	p_H (percent)	θ ($^\circ$)	J (mag)	H (mag)	K (mag)	rest (pc)
37.58790	73.00518	4 ± 1	109 ± 9	15.07 ± 0.05	14.30 ± 0.04	14.08 ± 0.05	2971
37.58771	73.00910	12 ± 3	99 ± 8	15.78 ± 0.07	15.12 ± 0.07	14.82 ± 0.10	484
37.63096	73.01263	7 ± 2	58 ± 10	15.38 ± 0.06	14.73 ± 0.06	14.46 ± 0.07	445
37.63104	73.00655	13 ± 2	119 ± 5	15.97 ± 0.08	14.90 ± 0.06	14.33 ± 0.07	1090
37.56222	73.01055	5 ± 1	140 ± 4	14.03 ± 0.03	13.16 ± 0.03	12.81 ± 0.03	2069
37.59742	73.02819	11 ± 2	73 ± 5	14.94 ± 0.04	13.97 ± 0.04	13.56 ± 0.03	668
37.65965	73.01757	5 ± 1	135 ± 8	14.87 ± 0.04	14.05 ± 0.05	13.82 ± 0.04	424
37.62266	73.02629	15 ± 1	79 ± 2	13.16 ± 0.03	11.92 ± 0.03	11.43 ± 0.02	3580
37.55118	73.02235	26 ± 5	135 ± 5	16.79 ± 0.17	15.67 ± 0.14	15.22 ± 0.15	1976
37.55531	73.02481	20 ± 3	45 ± 3	16.16 ± 0.10	14.93 ± 0.08	14.56 ± 0.08	817

Table 2.7: Estimated values of linear polarization for 33 stars detected in in the Ks band (p_{K_s}) and polarization position angle (θ). Additional columns are the JHK magnitudes and errors from 2MASS and distances from the Gaia survey.

RA (J2000) (deg)	DEC (J2000) (deg)	p_{K_s} (percent)	θ ($^\circ$)	J (mag)	H (mag)	K (mag)	rest (pc)
37.49817	72.91608	30 ± 4	98 ± 4	13.22 ± 0.03	12.57 ± 0.03	12.38 ± 0.02	1013
37.44123	72.96358	19 ± 3	77 ± 6	14.49 ± 0.04	13.50 ± 0.03	13.09 ± 0.03	871
37.54910	72.97186	22 ± 6	135 ± 10	15.35 ± 0.04	14.43 ± 0.06	14.32 ± 0.06	713
37.55281	72.97896	9 ± 3	128 ± 8	14.41 ± 0.03	13.44 ± 0.04	13.15 ± 0.03	2107
37.55851	72.99121	15 ± 5	104 ± 8	14.92 ± 0.05	13.94 ± 0.04	13.66 ± 0.05	3164
37.56753	72.99839	13 ± 2	88 ± 3	13.31 ± 0.03	12.34 ± 0.03	11.89 ± 0.02	3811
37.53776	72.99233	29 ± 8	102 ± 8	14.93 ± 0.05	14.30 ± 0.06	14.03 ± 0.06	2645
37.54876	72.99906	20 ± 4	124 ± 5	14.85 ± 0.04	13.99 ± 0.04	13.75 ± 0.04	1110
37.42209	72.99238	25 ± 6	121 ± 7	15.61 ± 0.06	14.69 ± 0.06	14.25 ± 0.06	1445
37.41771	72.99391	20 ± 3	125 ± 5	14.29 ± 0.04	13.31 ± 0.04	12.98 ± 0.03	1101
37.48941	73.02334	16 ± 3	52 ± 6	14.76 ± 0.05	13.61 ± 0.03	12.93 ± 0.03	892
37.44314	73.02090	20 ± 3	80 ± 4	12.09 ± 0.03	11.07 ± 0.03	10.79 ± 0.02	893
37.89399	72.94469	29 ± 4	128 ± 4	14.40 ± 0.04	12.74 ± 0.04	11.76 ± 0.02	1729
37.99294	72.98201	30 ± 6	93 ± 5	15.89 ± 0.10	14.77 ± 0.06	14.05 ± 0.05	2674
37.92658	73.02211	10 ± 1	91 ± 3	10.57 ± 0.03	9.57 ± 0.03	9.17 ± 0.02	2300

Continued on next page

Table 2.7 – Continued from previous page

RA (J2000)	DEC (J2000)	p_{K_s}	θ	J	H	K	rest
37.72405	72.96484	28 ± 8	125 ± 8	14.17 ± 0.03	13.33 ± 0.03	13.14 ± 0.03	934
37.74384	72.98866	13 ± 3	133 ± 6	14.77 ± 0.04	13.83 ± 0.04	13.38 ± 0.04	1494
37.73381	72.98598	24 ± 4	129 ± 4	13.70 ± 0.03	13.25 ± 0.03	13.21 ± 0.03	819
37.65339	72.98377	7 ± 2	98 ± 8	13.74 ± 0.03	13.22 ± 0.04	13.07 ± 0.03	567
37.63532	72.98826	8 ± 1	104 ± 2	13.63 ± 0.03	12.23 ± 0.03	10.90 ± 0.02	5109
37.64659	72.99383	8 ± 2	88 ± 6	14.34 ± 0.03	13.50 ± 0.03	13.04 ± 0.02	982
37.71638	72.99668	22 ± 1	133 ± 3	10.19 ± 0.03	9.77 ± 0.03	9.70 ± 0.02	232
37.71886	72.99310	15 ± 4	128 ± 10	12.86 ± 0.03	12.52 ± 0.03	12.42 ± 0.02	736
37.69604	73.01434	22 ± 4	158 ± 7	14.22 ± 0.05	13.67 ± 0.05	13.50 ± 0.05	733
37.67549	73.00384	12 ± 2	132 ± 4	13.79 ± 0.03	12.94 ± 0.03	12.63 ± 0.02	901
37.83246	73.01491	14 ± 4	50 ± 9	13.94 ± 0.03	13.30 ± 0.04	13.02 ± 0.04	355
37.77859	73.01794	3 ± 1	49 ± 8	11.03 ± 0.03	10.76 ± 0.03	10.68 ± 0.02	344
37.76870	73.02041	16 ± 5	99 ± 9	14.67 ± 0.03	13.85 ± 0.03	13.52 ± 0.04	1154
37.57786	73.00077	29 ± 5	73 ± 5	14.83 ± 0.04	14.16 ± 0.04	13.75 ± 0.04	2212
37.63104	73.00655	21 ± 6	55 ± 7	15.97 ± 0.08	14.90 ± 0.06	14.33 ± 0.07	1090
37.59742	73.02819	21 ± 4	93 ± 4	14.94 ± 0.04	13.97 ± 0.04	13.56 ± 0.03	668
37.61727	73.02386	17 ± 3	83 ± 4	14.04 ± 0.03	13.40 ± 0.05	13.21 ± 0.04	748
37.62266	73.02629	24 ± 2	99 ± 2	13.16 ± 0.03	11.92 ± 0.03	11.43 ± 0.02	3580

2.A Error propagation of P & θ

2.A.1 σ_P

The Polarisation fraction is calculated as,

$$P = \frac{\sqrt{Q^2 + U^2}}{I} \quad (2.11)$$

Using Error propagation method, we can estimate the associated error in the measurement of polarisation fraction, P .

Using partial fraction,

$$\begin{aligned} \sigma_P^2 &= \left(\frac{\delta P}{\delta Q}\right)^2 \sigma_Q^2 + \left(\frac{\delta P}{\delta U}\right)^2 \sigma_U^2 + \left(\frac{\delta P}{\delta I}\right)^2 \sigma_I^2 \\ &= \left(\frac{\delta}{\delta Q} \frac{\sqrt{Q^2 + U^2}}{I}\right)^2 \sigma_Q^2 + \left(\frac{\delta}{\delta U} \frac{\sqrt{Q^2 + U^2}}{I}\right)^2 \sigma_U^2 + \left(\frac{\delta}{\delta I} \frac{\sqrt{Q^2 + U^2}}{I}\right)^2 \sigma_I^2 \\ &= \left(\frac{1}{I} \frac{2Q}{2\sqrt{Q^2 + U^2}}\right)^2 \sigma_Q^2 + \left(\frac{1}{I} \frac{2U}{2\sqrt{Q^2 + U^2}}\right)^2 \sigma_U^2 + \left(\frac{-\sqrt{Q^2 + U^2}}{I^2}\right)^2 \sigma_I^2 \\ &= \frac{1}{I^2} \left[\frac{Q^2 \sigma_Q^2}{Q^2 + U^2} + \frac{U^2 \sigma_U^2}{Q^2 + U^2} + \frac{Q^2 + U^2}{I^2} \sigma_I^2 \right] \\ \therefore \sigma_P &= \frac{1}{I} \left[\sqrt{\frac{Q^2 \sigma_Q^2 + U^2 \sigma_U^2}{Q^2 + U^2} + \frac{Q^2 + U^2}{I^2} \sigma_I^2} \right] \end{aligned}$$

2.A.2 σ_θ

The Position angle in terms of Stokes parameter, is formulated as,

$$\theta = \frac{1}{2} \tan^{-1} \frac{U}{Q} \quad (2.12)$$

Similarly, working for the error in the position angle, σ_θ ,

$$\begin{aligned} \sigma_\theta^2 &= \left(\frac{\delta\theta}{\delta U} \right)^2 \sigma_U^2 + \left(\frac{\delta\theta}{\delta Q} \right)^2 \sigma_Q^2 \\ &= \frac{1}{4} \left[\frac{Q^2}{(Q^2 + U^2)^2} \sigma_U^2 + \frac{(-U)^2}{(Q^2 + U^2)^2} \sigma_Q^2 \right] \\ &= \frac{1}{4} \left[\frac{Q^2 \sigma_U^2 + U^2 \sigma_Q^2}{(Q^2 + U^2)^2} \right] \\ \therefore \sigma_\theta &= \frac{\sqrt{Q^2 \sigma_U^2 + U^2 \sigma_Q^2}}{2(Q^2 + U^2)} \end{aligned}$$

Chapter 3

Instrument Design

The telescopes are eyes into the vast universe and act as light collecting buckets. From small portable telescopes of 5 inch to world class telescopes of 30-40 m is the range of technology we are witnessing today. They help us to understand the intricate mechanisms of formation & evolution of various astronomical objects. Thus they are the starting point to study many phenomena, some of which are understood and some are still a mystery to be solved! The idea behind building new telescopes with different designs comes from these unsolved scientific goals. The focal plane instruments, also called the backend instruments, are the backbone of the telescope, and they are always driven to achieve more than targeted. Instruments are designed and built with the specifications to fulfil the science drivers.

Mt. Abu Infrared observatory already has a dedicated 1.2 m equatorial mount telescope for multiple science goals and a 0.5 m telescope for comet & variability studies. The NICS (Near IR camera & spectrograph) instrument has been the main workhorse of the 1.2 m telescope and been widely used with its 8' x 8' FOV over the Y, J, H, K_s & K wavebands, and a resolving power $R \sim 1000$ in the IJ, JH, HK bands. Polarizing capability was recently added ([Aarthy et al. \(2019\)](#), also Chapter 2), using a rotating

wire-grid polarizer (WGP). This facility (NICSPol) was placed in the warm optics above the instrument window and is available in the J, H, K_s wavelength bands.

PRL is now adding a new 2.5 m telescope at Mt. Abu. The enhancement in the primary mirror aperture by a factor of 2 will quadruple the light gathering capability of the 2.5 m telescope as compared to the 1.2 m existing one. The 2.5 m telescope is a Ritchey Chretien design, with hyperbolic primary & secondary mirrors. The RC type telescopes are very common in the big facilities these days, due to the cancelling of 3rd order coma aberration present in the off-axis imaging. To make best utilization of this new possession, a host of backend instruments are being designed and developed. We have taken up designing and developing a multi-purpose instrument, Near infrared Imager, Spectrometer & Polarimeter (NISP). The instrument will provide the imaging, spectroscopy & imaging polarimetry modes in all the 4 NIR wavebands Y, J, H, K_s. The major science themes for NISP include:

1. Imaging : Using the large FOV of imaging technique to study objects ranging from nearby comets and planets, to the starforming regions of the Milky Way and on to the far-away galaxies and Active Galactic Nuclei in the Near infrared regime.
2. Spectroscopy : Spectroscopic study using the various options designed for NISP will allow in depth spectroscopic studies of a wide range of objects, for eg. Be/Xray binaries, novae in our galaxy and nearby galaxies, supernovae in distant galaxies and transients all across the universe. One of the important NIR spectroscopic results expected is in the study of comets. The water ice feature present at 1.4 & 2.0 μm is a good tracer for the presence of water in comets. The oxygen line seen in the visible spectrum of comets can arise from either H₂O or CO₂ molecules. Hence, compiling the data with NIR spectrum will help in concluding the origin of oxygen line from the water feature in comets.
3. Imaging polarimetry : Imaging polarimetry of the highly extincted regions of the Milky Way galaxy will help us measure the polarization of redder stars which were obscured by the dust at shorter, visible wavelengths. Near IR bands have less scattering and hence can penetrate deeper into the obscured regions. With

the polarization measurements, we can deduce the magnetic field geometry of the star forming cloud, the magnetic field strength & infer dust properties. "Hidden" AGN can be detected in external active galaxies using the technique of imaging polarimetry.

NISP instrument aims to couple the larger aperture of the telescope with versatile capabilities in the infrared.

This chapter covers the optical tools and techniques available to the instrument designer.

3.1 Zemax - Introduction

The optical design for NISP is carried out using physical principles to calculate the input parameters to the *OpticStudio - Zemax*¹ software. It is an advanced optical design software tool to realise and input the details of each surface of the lenses and traces the rays through them. The analysis within zemax features the 3D layout of our design, and several other criteria to check the performance of the design. The design is also improved by the 'merit function editor' as an important feature present within the software. We can constrain the different element properties using the valid operands and then optimize the design using few elements radius & thickness values to be set as variable. Apart from running the analysis tools provided by zemax, we can also write small scripts in it to do specific analysis. Further sections will give a more detailed look into some of the important tools which have been utilised in the optical design process.

¹<https://www.zemax.com/products/opticstudio>

3.2 Preliminary study based on existing instrument designs

3.2.1 NICS & MIMIR

To gain an insight into the starting point for the optical design of NISP, a thorough study was carried out of other instruments with available zemax designs. The two instruments whose design I could use to get a deeper understanding into the intricacies of optical design were NICS, hosted at 1.2 m telescope of PRL & MIMIR², hosted at 1.8 m Perkins telescope, Arizona. Both these near-IR instruments were found favourable as starting points for our work, since they had multiple mode functionality. A careful look was taken at their designs to study the material used in the designs, the pupil width achieved by the collimator optics, the definition of the merit function operands etc.

There are fewer options in the material selection for the infrared band, hence, the materials which are commonly used in such instruments were studied. NICS uses a F/13 collimator and a F/6.6 camera combination in its design. The L shape of NICS optics was in the initial plan for the optics chain of NISP too, but since we didn't want to have a reflecting component in the design due to its introduction of instrumental polarization and decreasing the overall transmission of the instrument, we chose to go with straight path optics implementation. The optics used in NICS was initially considered as a starting point for NISP, but we had to leave it and start from a fresh design, because the fabrication of the lenses looked difficult.

The MIMIR design includes an F/5 & F/17 camera with gratings used for spectroscopy. The design makes for a very good case study for complex multi-function NIR astronomical instrumentation

²http://people.bu.edu/clemens/mimir/optical_designs.html

3.2.2 NICSPol & its simulation

NICSPol is a polarimetric module add-on to the general purpose NICS instrument at Mt. Abu 1.2 m telescope (Aarthy et al., 2019). It uses a 25 mm x 25 mm wire-grid polarizer (WGP) component bought off-the-shelf from Thorlabs. This component has been fixed on to a field rotator setup with a clear aperture of 25mm diameter to reduce edge effects associated with the corners, which transformed the square dimensions for the WGP to circular diameter of 25 mm. The measurements of polarization are done at 4 position angles (0°, 45°, 90° & 135°) of the WGP by motorized field rotator.

We simulated the polarization mechanism as performed by the WGP using zemax. We first defined the WGP polarizer in the beam path of the optical design of the NICS instrument, placing it above the cryostat window. The definition of the component made use of the dimensions from the autocad file of the component as provided by Thorlabs. The zemax definition of the WGP involved two surfaces with rectangular aperture of 25 mm. A thickness of 2.2 mm was set and the material was defined as ‘fused silica’, the material of the substrate in WGP. This defined the dimension for the WGP. Now to incorporate the polarization mechanism within this component, the first surface of the WGP was defined as a ‘Jones matrix’ surface type. Jones matrix surface modifies a Jones vector as,

$$\begin{bmatrix} E'_x \\ E'_y \end{bmatrix} = \begin{bmatrix} A & B \\ C & D \end{bmatrix} \begin{bmatrix} E_x \\ E_y \end{bmatrix} \quad (3.1)$$

It can be defined for several polarizing components. Considering the polarization axis in the X-direction, the matrix for the WGP is defined by:

$$\begin{bmatrix} (1,0) & (0,0) \\ (0,0) & (0,0) \end{bmatrix}$$

These values are entered in the 8 parameters required for the Jones matrix surface implementation. The format is (a,b) , where a is the real part & b is the imaginary part. Hence, for all the A, B, C, D complex numbers, the real and imaginary parts are

entered in the parameter window as per our requirement. This completes the design realisation for the WGP used in NICSPol. The component & a 3D layout for the NICSPol system is shown in Figure 3.1 & 3.2. We performed an analysis for the polarization

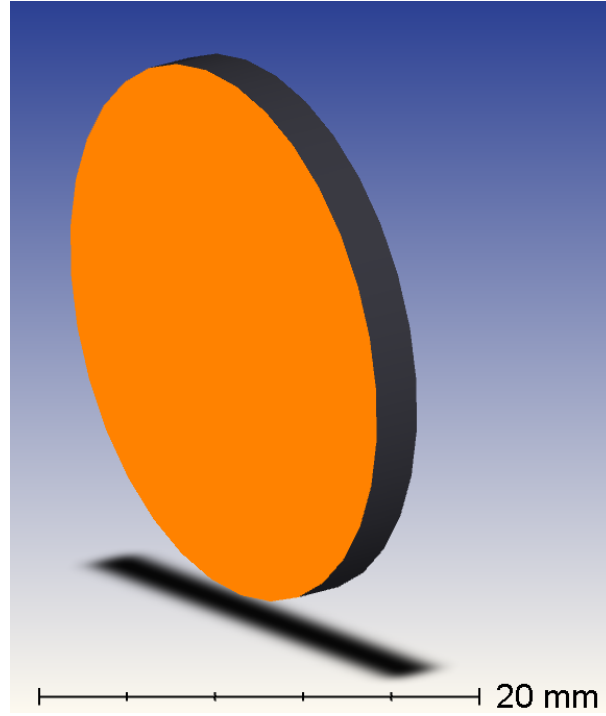


Figure 3.1: 3D shaded model of the circular Wire Grid Polarizer as used in NICSPol.

pupil map of NICSPol, to simulate the transmission as attained with the 4 position angles orientation with respect to the polarization axis of the wire grid. The results are compiled in the Figure 3.3. The different orientations for the polarization pupil map involves the definition of the input polarization using Jones electric field vector, J_x & J_y . The matrix 3.2 lists the values for each of these vectors for the angles 0° , 45° , 90° & 135° respectively.

$$J = \begin{bmatrix} J_x \\ J_y \end{bmatrix} = \begin{bmatrix} 1 & 0.707 & 0 & -0.707 \\ 0 & 0.707 & 1 & 0.707 \end{bmatrix} \quad (3.2)$$

As the polarization axis is defined horizontally in the X-direction, the transmission at 90° is found to be 0% as seen in the bottom left panel of Figure 3.3. The transmission at the image plane after the addition of polarising optics is $\sim 19\%$ for the orientation parallel to transmission axis of WGP. At the other two angles, 45° & 135° , there is a

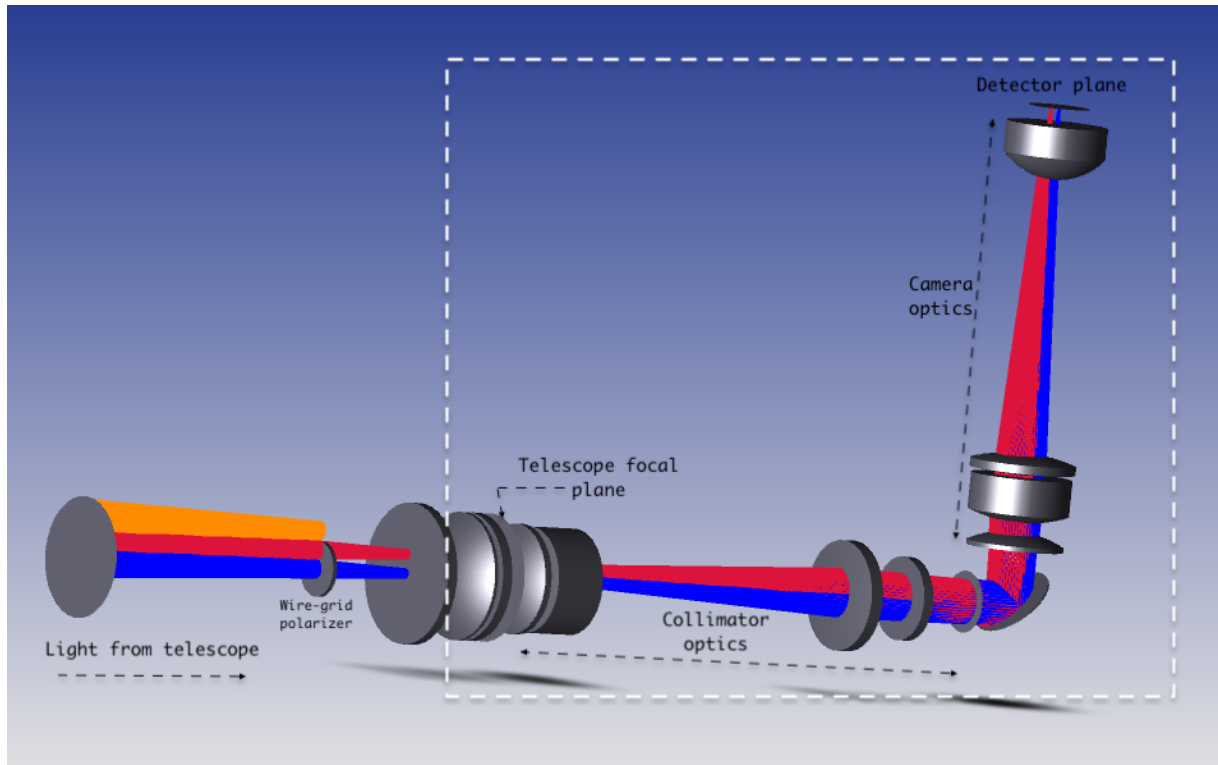


Figure 3.2: The labelled, shaded model layout for the NICSPol module added above the cryostat window of NICS. The optics inside the white dotted box is maintained at cryo temperature $\sim 77\text{K}$.

decrease in the transmission from the parallel orientation as expected. The output polarization state is P-polarized, since all the output beams are parallel to the axis of polarization.

We mention here that a change is noted in the spot diagram at the image plane from the performance achieved in the imaging mode of NICS. The spot diagram for NICS & NICSPol are shown in the Figures 3.4 & 3.5. The size of the spot is within 2 pixels of the NICS detector. We also examine the Modulation transfer function for the NICSPol module, shown in Figure 3.6. It shows that the NICSPol module performance for contrast transfer is $\sim 30\%$, and stays a bit far from the diffraction limit line $\sim 60\%$. This leads to a reduction in the sharpness of the spot as captured by the detector array and hence leads to an increase in the FWHM of objects compared to those achieved with NICS imaging. This loss of contrast is attributed to the addition of 'fused silica' material in the optical path of NICS for which the design is not optimized, as the polarization module was a later add-on to the NICS instrument in the warm optics location. The

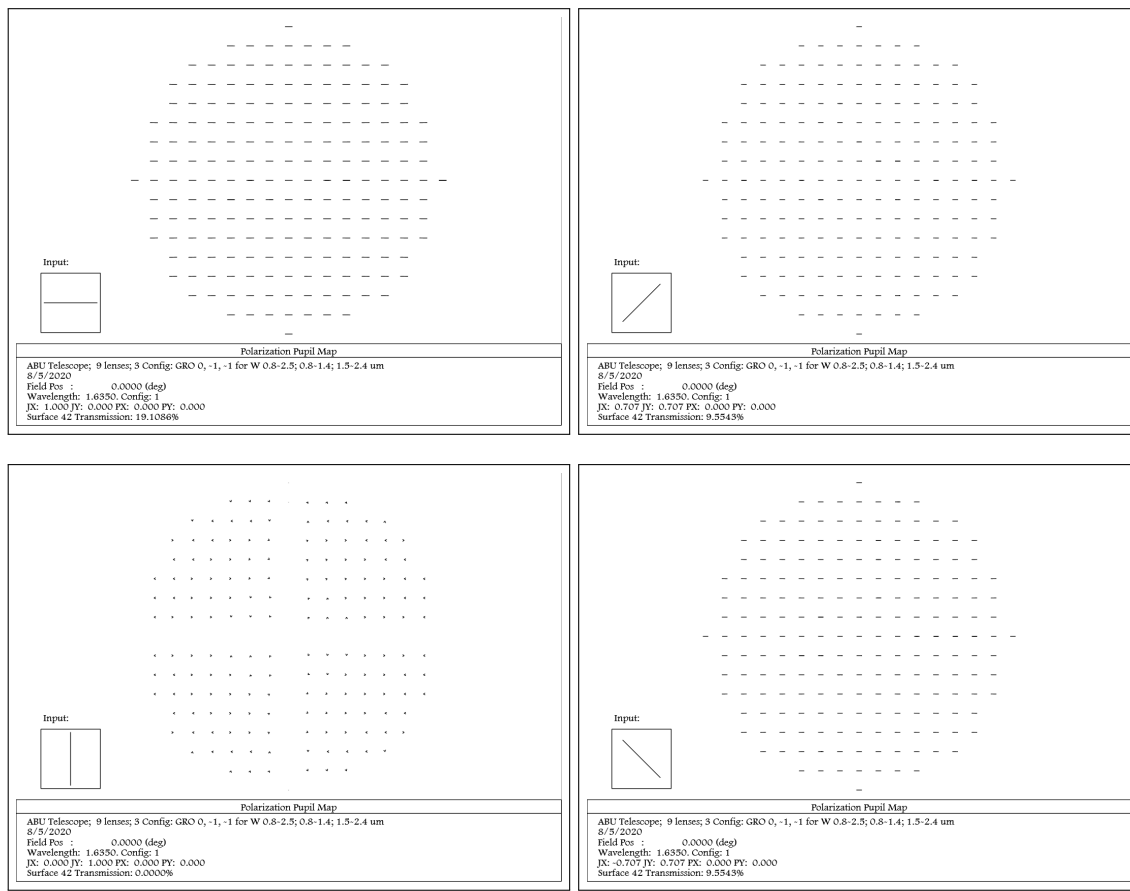


Figure 3.3: Polarization pupil map of the wire-grid polarizer at 4 modulation angles of the polarizer. The transmission percent for each of the orientation is seen in the bottom panel of each plot. The results are shown for 1.635 μm wavelength (H band central wavelength).

vignetting analysis for NICSPol system shows a fall in the 'fraction of unvignetted rays' curve beyond 0.0335° field point. The Figure 3.7 gives a glimpse of this aspect, with 100% of the rays being transmitted before the obscuration due to the small size of the WGP.

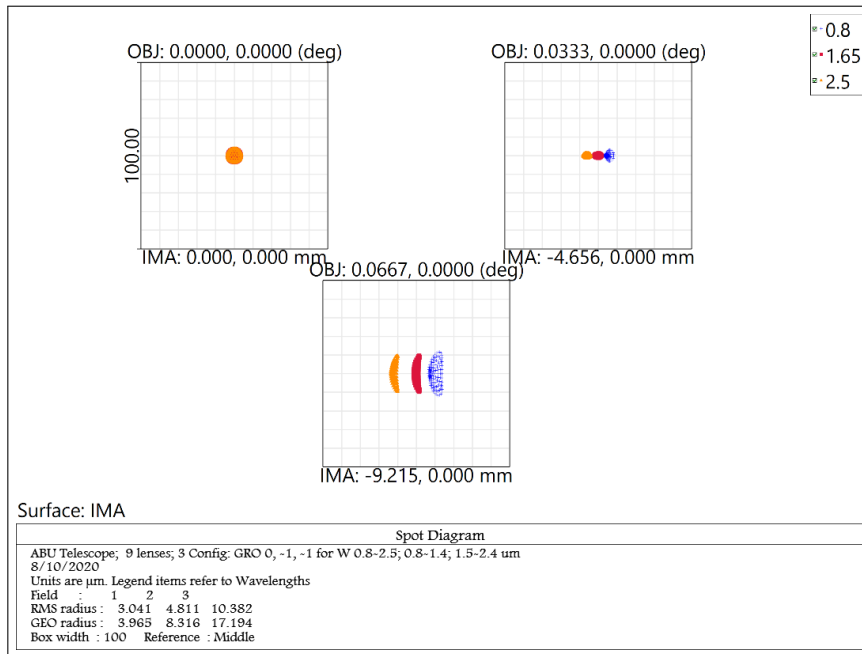


Figure 3.4: The spot diagram at the image plane for NICS instrument

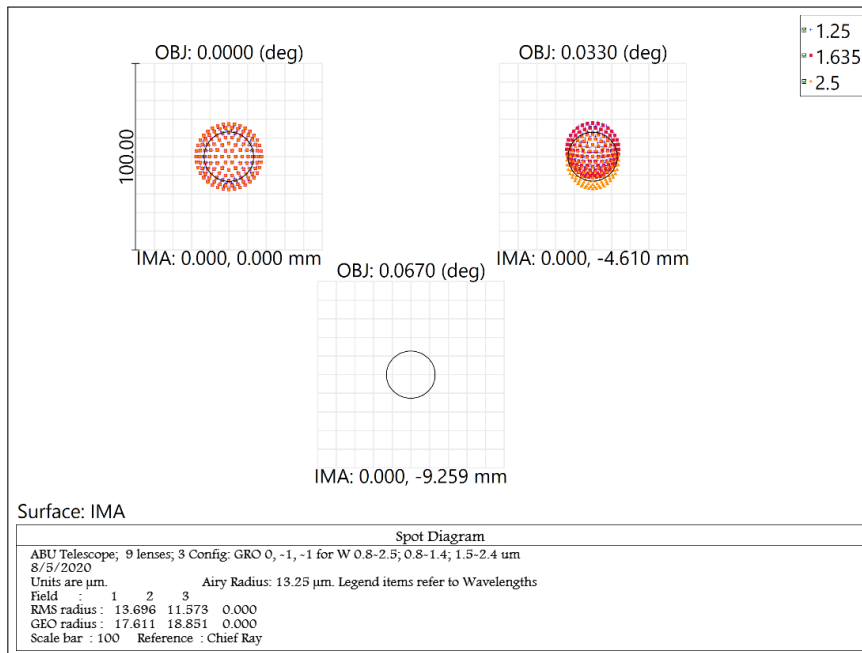


Figure 3.5: The increase in the spot size upon addition of the WGP component in NICSPol is seen compared to Fig 3.4. The spot in the third field location (0, -9.273) is lost due to rays being blocked by the WGP support (vignetting).

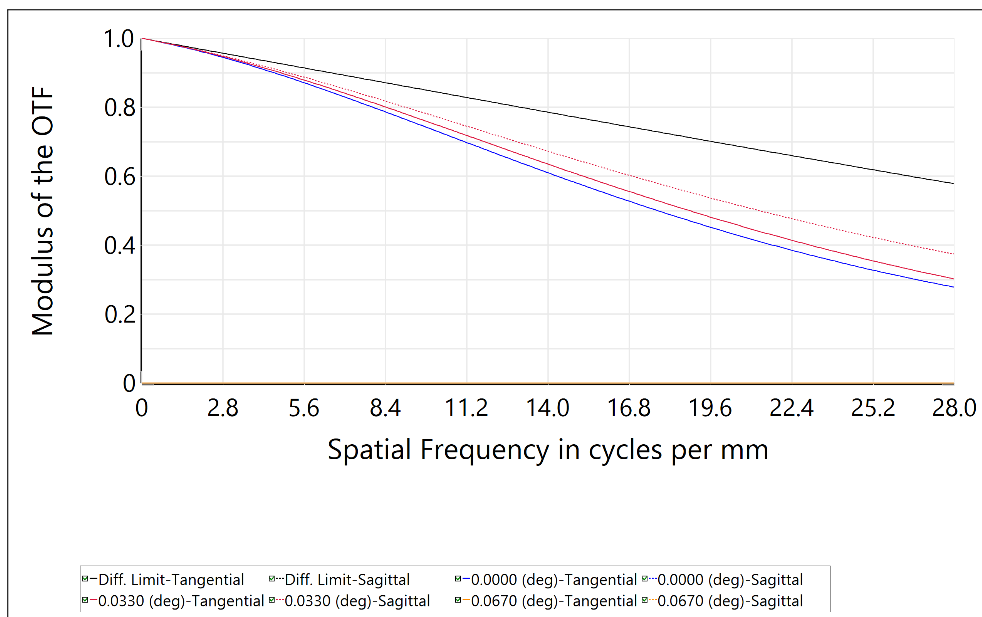


Figure 3.6: The MTF plot for NICSPol. The black line is for the diffraction limited performance. Other colors are for the different field locations defined for NICSPol.

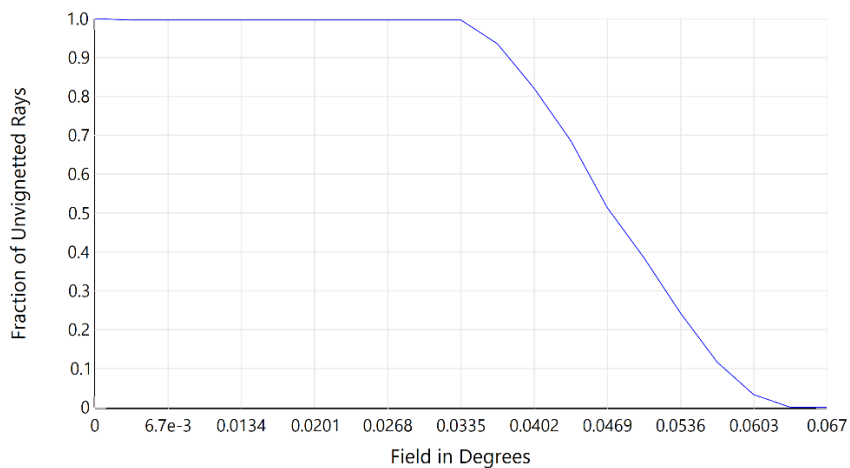


Figure 3.7: Vignetting plot for NICSPol. The fraction of unvignetted rays starts falling beyond $2'$ radius.

3.3 Alternative conceptual layout plans for NISP

This section describes the layout preferences for the optical design of Near Infrared Imaging Spectro-Polarimeter (NISP). The point of discussion includes the optical design configurations, refractive vs reflective optics, size of the elements etc. An instrument performing multiple operations requires a large volume to incorporate all the optomechanical parts. It is important to minimize the volume and ensure optimal utilization. Keeping this in mind, apart from the 'L configuration of Near-IR Camera Spectrograph (NICS) instrument at MIRO, we also thought about a 'U shaped configuration. This configuration was considered to see if it would result in a more compact mechanical volume.

From the planning stage of NISP, we had considered the optical system with *refractive optics* design, as the multiple surfaces of the lenses would help in better optimization of the design and also in minimizing the aberrations compared to the reflective surfaces. The size of the optical elements would be decided by the size of the detector and the telescope plate scale (linked to the primary mirror size). For NISP, we have decided to use a 2K x 2K detector array, which implies approximately double the size of NICS optical elements, since the latter uses a 1K x 1K array. With these prior inputs and few calculations for the FOV requirements, I started working on the optical design.

The 'U' & 'L configuration concept design is attached in the Figure [3.8](#).

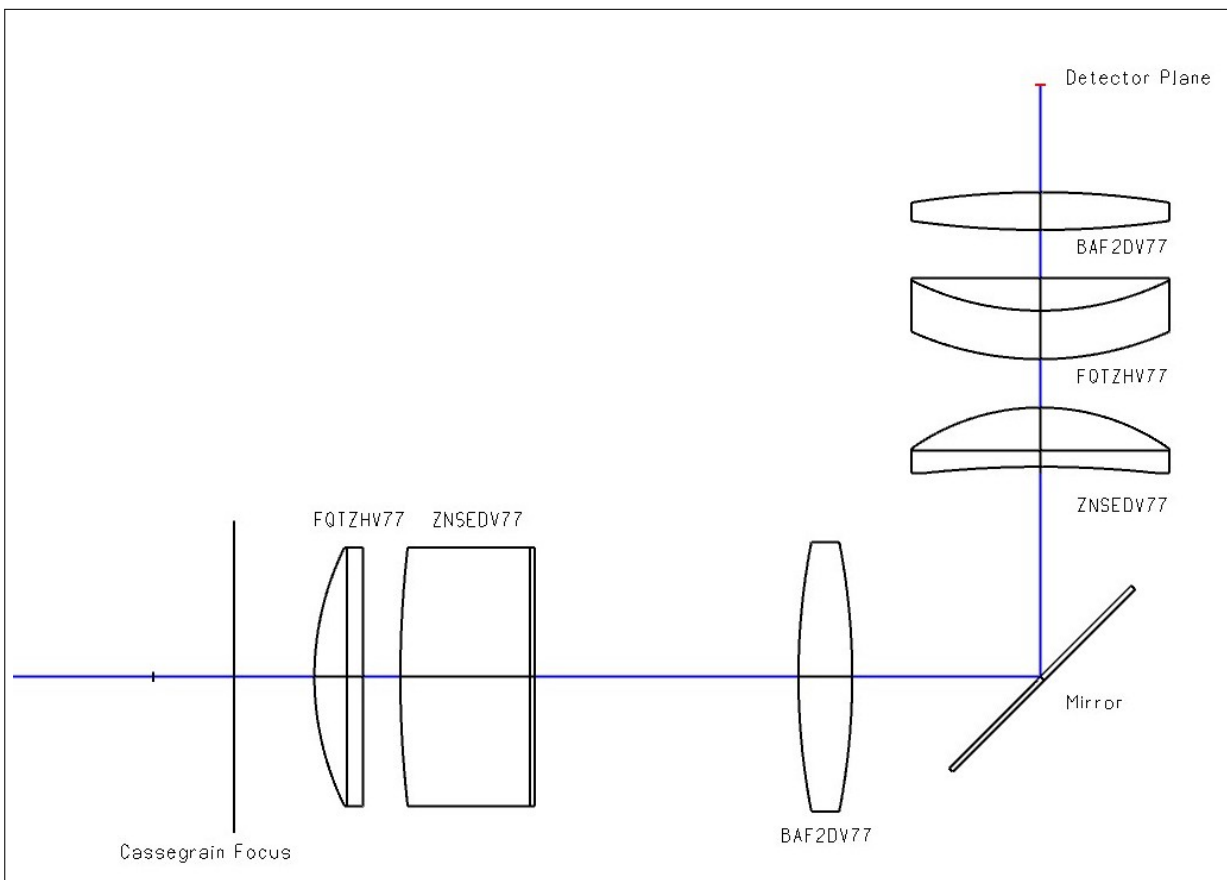
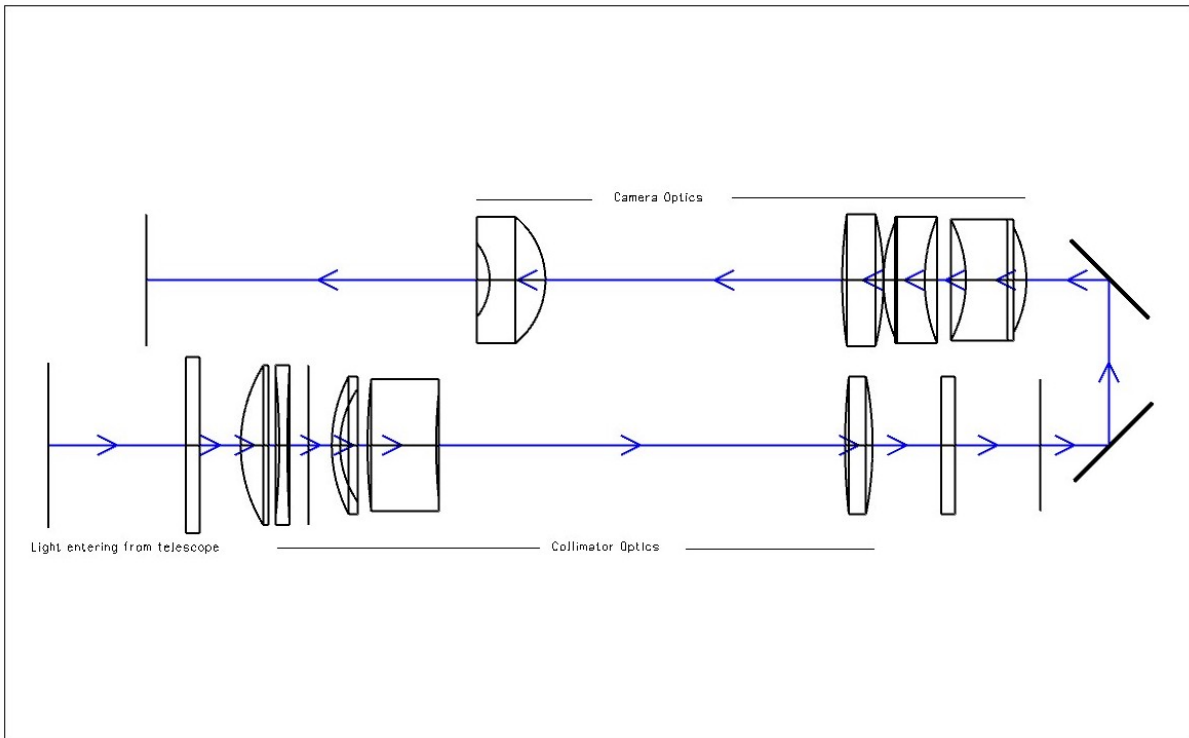


Figure 3.8: Different layouts considered at the the design planning stage for the NISP optical design

Both the above designs included mirrors for folding the optics. Using mirrors in a multimode instrument leads to reduced transmission from the optical system and could add to extra polarization and stray light which has to be dealt at future stages. To avoid these added factors of unwanted induced noise in the optics, the final optical layout adopted is an "I" configuration or "straight" path for the optical system. This will enable a more efficient use of the volume of the instrument dewar, with the electro-mechanical components having enough space to be installed. The components used for enabling the different modes play a strong role in the overall throughput of the instrument and the efficiency achieved. The Teledyne H2RG array detector has a pixel size of $18 \mu m$. The imaging FOV for the NISP instrument is considered as maximum $10'$, since the telescope supports this FOV without the need of field corrector. Spectroscopy would be met by using "grisms, and polarimetry will make use of a "Wedged Double Wollaston. The Table 3.1 gives a detailed description of the requirements for the NISP instrument and its other properties.

Table 3.1: The design goals & specifications for the NISP instrument.

Parameter	Specification
Detector	Teledyne H2RG array
Pixel size	$18 \mu m$
Detector size	36.8 mm
Operating Wavelengths	Υ, J, H, K_s
1" at focal plane	$97 \mu m$
Plate scale @ CF	$10.3'' / mm$
Plate scale @ detector plane	$16.6'' / mm$
Pixel scale	$0.3''$
Spot size	$54 \mu m$
Imaging FOV	$10' \times 10'$
Resolving power	~ 2000 using grisms
Temperature	77 K

3.4 Design Parameters

Any optical design should match the environment in which the instrument optics will be placed during observations. The environment depends upon the wavelength of operation and sensitivity of the detector employed. Since the wavelength of interest for us, is the near-infrared, the thermal emissions from the body of mechanical container, connections etc become significant & increase manifold as we go beyond $1.2 \mu m$. So, these emissions will add to the noise in the object signal at the detector. To reduce these thermal effects, the opto-mechanical components of the instrument should be cooled by operating it at liquid nitrogen temperature (~ 77 K). The environment for the design was set to a temperature of -196.0 C, and the vacuum pressure of 10^{-6} mbar in Zemax. One must recall that the refractive index of a material depends upon the temperature, which is represented by a parameter β . With changes in the temperature, the refractive index and hence the focal length changes leading to loss of focus at a particular wavelength. The pressure changes have a greater effect on the spot size than temperature, and hence the required pressure needs to be maintained throughout the functioning of the instrument. Other prior settings are the wavelength of operation and the field of view for which we want to design the instrument. The field will refer to a full coverage of the FOV required at the detector plane, which has to be set at the Cassegrain focal plane. For NISP, a $10' \times 10'$ FOV at the detector plane (37 mm square size) requires a $14.5'$ field coverage diagonally (covering 52.2 mm diagonal size of detector) to prevent vignetting at the corners. Hence, the 84.5 mm diagonal at the Cassegrain focal plane has to be demagnified to match the size of the detector ~ 52.2 mm at the detector plane using collimator & camera optics combination.

3.4.1 Lens material selection

One of the most crucial steps to start the design is the choice of the materials for lenses at the operating wavelength bands. This choice depends upon the refractive index, thermal expansion coefficient, dispersion, hygroscopic properties etc of the material.

The requirement for the proper selection of material arises from the need to eliminate the thermal and wavelength dependence of focal length due to temperature changes. From the point of view of fabrication process, the lenses should be selected based upon their availability. The design should ensure avoidance of sharp edges and steep curvatures in lenses which may make the fabrication process difficult. All the lenses commonly used are spherical with conic constant 'k value 0. 'Aspherics are a class of lenses, where $k \neq 0$, used in optical designs to speed up the achievement of the required specifications. Though usage of 'aspheric lenses are good to reduce the spherical aberrations, their use is not to be preferred due to difficulties in their precise fabrication and alignment with other optics. One of the chief criteria which characterizes a glass into optical material is its refractive index 'n'. There values vary with the changes in wavelength, temperature, pressure etc. The optical designs of the instruments are very sensitive to these changes, and hence we shall discuss their effects in the following paragraphs.

Change with wavelength; $\frac{dn}{d\lambda}$:

In the cases of optical systems, aberrations due to dispersion need to be minimized by the proper selection of glasses based upon its 'n' value. The dependance of refractive index on wavelength is seen in the empirical formula by Wilhelm Sellmeier (1872), who extended Cauchy's formula to apply it to infrared bands. The formula can be expressed as,

$$n^2(\lambda) = 1 + \sum_i \frac{B_i \lambda^2}{\lambda^2 - C_i}$$

B_i & C_i are the experimentally determined Sellmeier coefficients. The refractive index falls as the wavelength increases. Figure 3.9 shows a deviation of the Cauchy's equation at IR bands & the trend followed nicely using Sellmeier revised equation, Keeping this in mind, the set of materials used in the lenses for NISP are BaF₂, CaF₂, LiF, ZnSe, ALN, AgCl, CsBr & KRS5. They have refractive indices ranging from 1.3 - 2.44 and are used in infrared wavelength instruments. The properties of these lenses are tabulated in the Table 3.2.

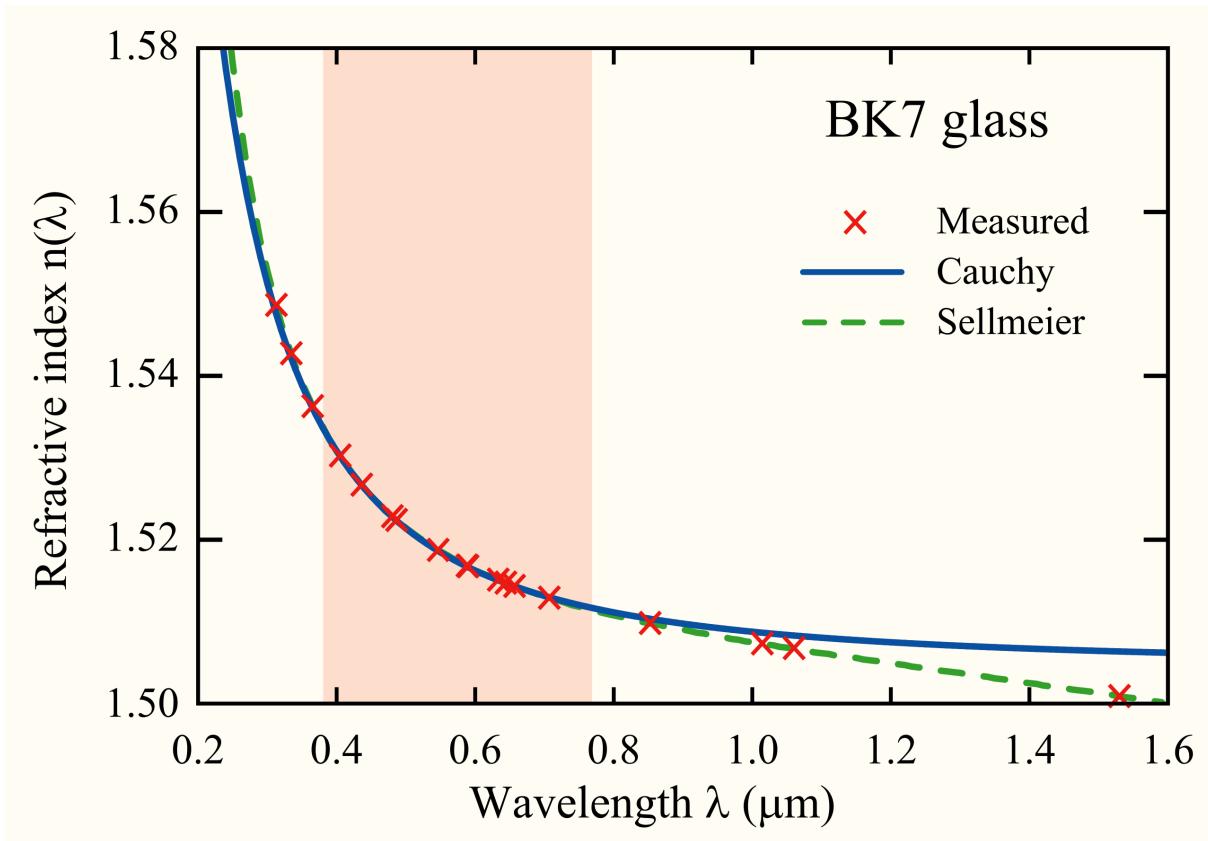


Figure 3.9: Refractive index variation with wavelength. Image by Bob Mellish, CC BY-SA 3.0, <https://en.wikipedia.org/w/index.php?curid=11902841>

Change with temperature; $\frac{dn}{dT}$:

The values of refractive index are usually defined at specific temperature. The refractive index change with temperature, is predominantly due to the variation in the density of material with ΔT . A functional dependence (Waxler & Cleek, 1973) is,

$$\frac{dn}{dT} = \left(\frac{\partial n}{\partial T}\right)_{\rho} + \left(\frac{\partial n}{\partial \rho}\right)_{T} \left(\frac{\partial \rho}{\partial T}\right) \quad (3.3)$$

Table 3.2: Properties of the materials for lenses used in NISP. The refractive index values for a few of the materials at the respective central wavelength are taken from <https://refractiveindex.info>

Material	Refractive Index @			
	Y	J	H	K _s
LiF	1.3869	1.3851	1.3820	1.3771
ZnSe	2.4762	2.4593	2.4462	2.4388
ALN	-	-	2.0284	2.0219
AgCl	2.0216	2.0147	2.0089	2.0053
KRS5	2.4434	2.4209	2.4031	2.3928
CsBr	1.6781	1.6750	1.6724	1.6708

3.4.2 Lens splitting

The first step towards making an optical design is the selection and placement of lenses. For this one can go for similar instrument designs from literature and try to use them to get the specific performance as needed by them, or start putting the lenses intuitively and learn how it behaves with an incident beam of light. One needs to choose a good starting point, whatsoever, to reach the best of requisite specifications from optics. As listed, any starting way we follow, we need to start modifying and optimizing it based upon our demands. Once we reach a good set of lenses and the spot diagram is showing realistic RMS radius for the image, we need to correct it for aberrations and bring the rms radius size to a lesser value. For this several attempts are made like, putting the material on "Variable" for hammer optimization, lens splitting, using doublets, triplets etc. Defining aspherics in the design, though helps immensely by removing many aberrations, should be our last resort. Amongst these, splitting of lenses (Geary, 2002), is a very useful approach which includes distribution of power among different elements of a set of lens. It not only helps the design to become aberration free, but also achieves better diffraction-limited spot sizes.

Lens splitting helps us in distributing the power of singlet lens into doublet or triplet.

A singlet lens of power and refractive index, is divided into doublet or triplet by equally dividing the power into the new elements. Let ϕ be the power of singlet lens, then $\phi_d = \frac{\phi}{2}$, is power of doublet lens. Using the "thin lens" power equation, we calculate the starting radii of curvature for the doublet elements.

$$R_1 = 2 \frac{(n-1)}{\phi}$$

$$R_1 = -R_2$$

This radii is set for the singlet turned into doublet, with the material being the same for now. To optimize the design with the new introduction of doublet, the new radii is set 'Variable', and optimized to minimise the merit function and achieve the necessary performance. The performances before and after the lens splitting is clearly evident and it improves the design. If the doublet doesn't yet bring the required specifications, we go for triplet splitting.

3.4.3 Optimization of design parameters

The optical design of NISP has undergone continuous optimizations to minimize the spot size, achieve close to diffraction limited performance in encircled energy, produce an un-vignetted full FOV & with minimal aberrations. The entrance pupil diameter is 2.5 m which is the primary mirror aperture of the telescope. The current design, post optimization, consists of collimator lens beam of F/8 at the Cassegrain focal plane which is reimaged at the detector plane through F/5 camera optics and hence achieve a diagonal FOV of 14.5'. To list few of the major criteria for optimization, we discuss in detail their significance for the design in the following paragraphs.

Spot Size

Spot size refers to the total size of the projection of rays on the image plane. The pattern of the set of rays defines the image quality of a design. Zemax gives RMS and geometric spot radius for all the field angles and all wavelengths. The RMS radius gives an average concentration of all the rays falling on the image plane. It tells about a realistic measure of the resolution to be expected with the inclusion of all the aberrations. The geometric radius, on the other hand, tells us about a physical spread of the rays falling on the image plane. This spot radius is a measure of the size of a point source object as it travels through the atmosphere to reach the ground based telescope system. The observations with ground based instruments suffer from the atmospheric turbulence, and one cannot achieve the diffraction limited performance. Hence, the size of the spot is dominated by the seeing caused due to turbulence, and hence a spread is seen in the size of point source. This is called the Point Spread Function (PSF). Any design requires the spot size to be well within the best seeing limit at the observatory location as decided by the wavelength and place of observatory. The seeing limit must be covered by a sufficient number of pixels satisfying the Nyquist sampling criterion. This would result in a good image with seeing limited spatial resolution. Lately with the use of adaptive optics, which corrects the variations due to atmospheric turbulence in an ideal spherical wavefront, the diffraction limited performance is achieved. NISP, being a general purpose instrument has a goal of a large field of view and hence we adhere to a seeing limited design.

The seeing for Mt. Abu observatory location is typically about $1''$. In NISP, the imaging optics gives a FOV of $10' \times 10'$. This gives the pixel scale of $0.3''$ for each of the 2048 pixels. If we consider Nyquist criteria, 3 pixels shall be used to image an object with a $1''$ seeing disk. The pixel size of the detector is $18 \mu m$, and considering 3 pixels sampling gives the spot size to be achieved $\sim 60 \mu m$. Seeing the spot diagram, one can tell the type of aberration dominant for any field angle. The spot size depends a lot on the vacuum pressure in the dewar. The achieved spot size for the NISP instrument design are discussed in the further chapters.

Aberrations

Aberrations are the departures of the performance of an optical system from the predictions of paraxial optics. The departures or defects could be in the shape of wavefronts. The wavefront of an EM radiation is always considered to be spherical and hence expected to come to a perfect focus in an ideal imaging system. Deviation from the sphericity of wavefront leads to an aberrated image. The paraxial point is taken as reference point here, and the spread of ray intersections around it gives the types of aberrations present in the lens. Since, the optical systems are designed considering first order or paraxial optics, they mostly consider light as a ray. *Aberrations are on account of the wave nature of light*, but they also occur due to pure ray propagation, mostly in cases when large angle of incidence is considered for any surface. A typical wavefront map of a point source which suffers from the presence of different types of aberrations is compiled in the Figure 3.10. For an ideal optical system, a spherical wavefront em-

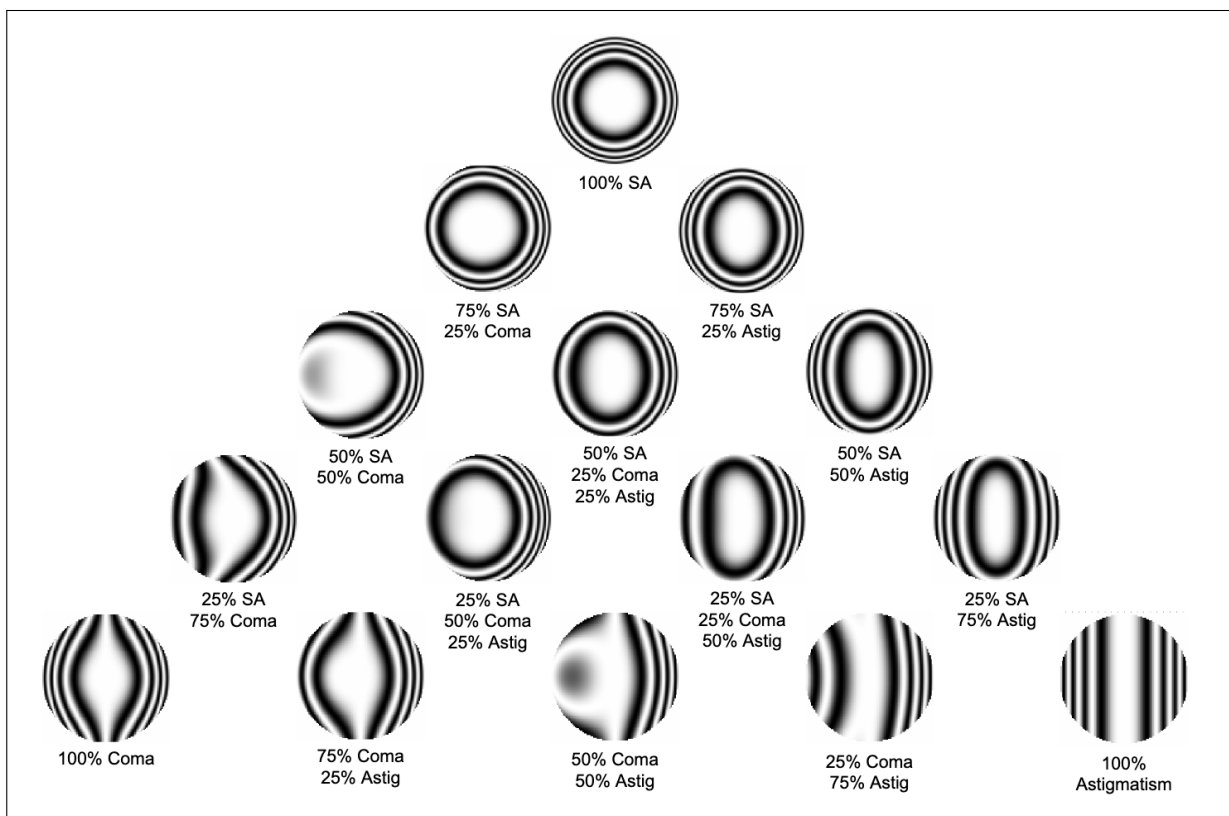


Figure 3.10: Wavefront map for an aberrated image. Image credit : Margy Green

anating from a point source, travels through as plane waves, and is converted back to spherical wavefront with the converging optics. These are termed as ‘ideal wavefronts’.

A deviation from ideal wavefront to actual (distorted) wavefront is termed as wavefront aberration. For a rotationally symmetric system, the wave aberration W for a ray from an object point of fractional height τ and passing through a point (ρ, θ) on the exit pupil is expanded as the power series:

$$W = W_{020}\rho^2 + W_{111}\tau\rho\cos\theta + W_{040}\rho^4 + W_{222}\tau^2\rho^2\cos^2\theta + W_{220}\tau^2\rho^2 + W_{131}\tau\rho^3\cos\theta + W_{311}\tau^3\rho\cos\theta \quad (3.4)$$

The first two terms are longitudinal and transverse shifts in the image position and not counted as aberrations. The next five terms represent the primary aberrations. They represent the primary spherical aberration, coma, astigmatism, sagittal field curvature and distortion respectively. These aberrations are the concerns of any optical designer & need to be minimized to 3λ or less to have a good design. In Zemax, the Seidel coefficients tab provides us with the values for these aberrations and the contribution from each surfaces for an on-axis system. For an off-axis or tilted system, one should explore the 'ray fan', 'OPD', spot diagram, field curvature and few other tools offered in Zemax to better understand the presence of all aberrations. This can be used to check for the worst offenders and during optimization, such surfaces should be labelled as free (variable) parameters to get a better design. A proper compilation of the available analysis tools along with its depiction for each aberration is shown in the Figure 3.11 & 3.12. 'Quick Focus is used sometimes to shift the focus to correct place after a series of optimizations.

Merit Function Editor

Merit function editor is an editor window in Zemax which helps to optimize a design as per the required specifications based upon few constraints. It has multiple operands defined to target the various design parameters, alongwith a default merit function which is a strong optimization tool. The operand for a specific purpose is selected and then the target value it should reach after optimization process, is entered. On optimizing the design, the elements whose parameters are set as 'variable' will have new values tending to the desired value against the operands. Subsequently, iterations go

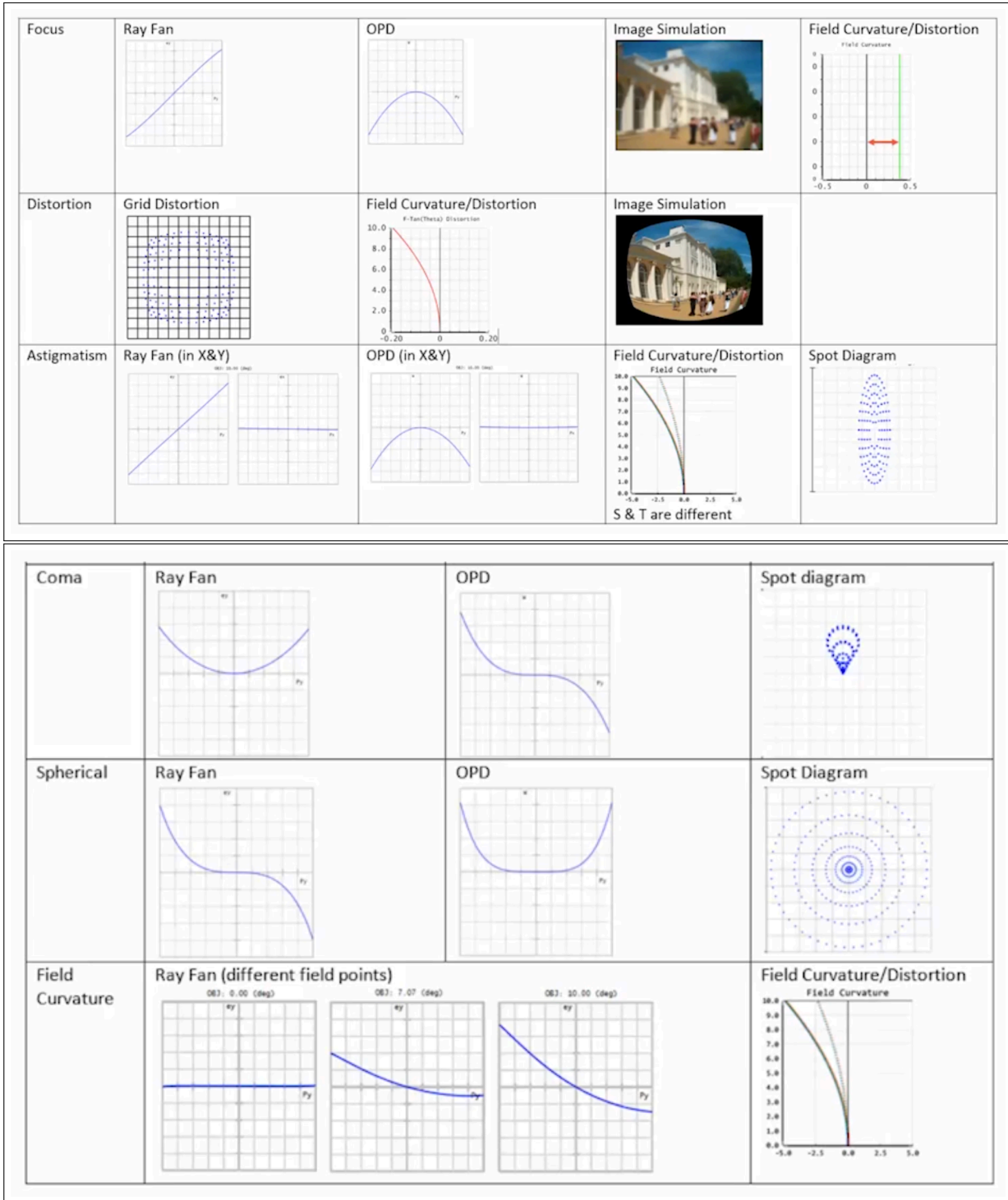


Figure 3.11: A compilation of the aberrations present in an optical system and the analysis tools present in Optic Studio, Zemax with proper representations. Image courtesy: Optic Studio

on till the target is achieved and design looks practically realizable. In optimizations, it runs Monte Carlo simulations, least square sums etc for each run with selected

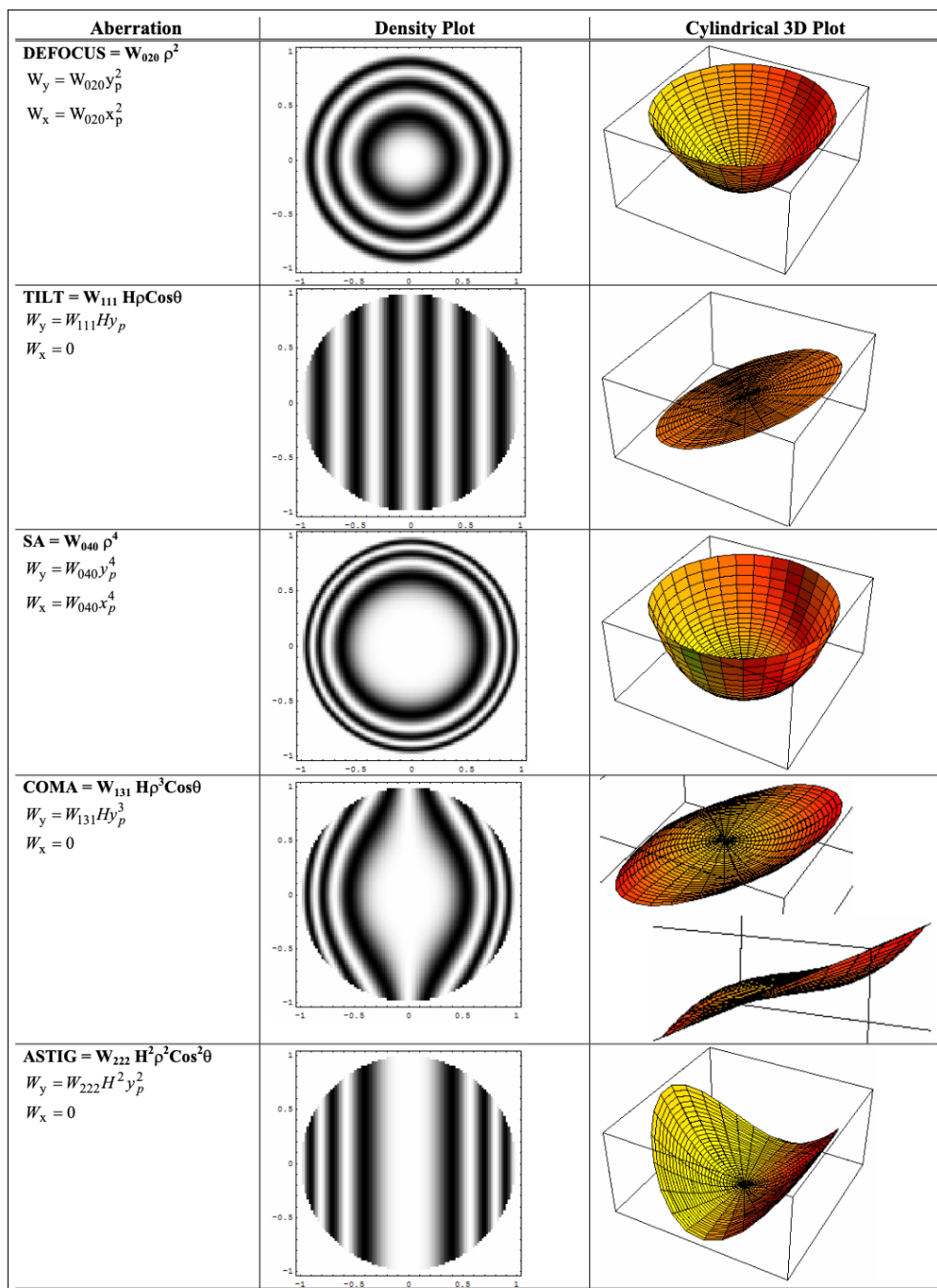


Figure 3.12: Aberrations and corresponding analysis tools in Zemax. Image credit : Margy Green

parameters and then tries to achieve a local minima. A typical Merit Function is defined as:

$$(MF)^2 = \frac{\sum_i W_i (V_i - T_i)^2}{\sum_i W_i} \quad (3.5)$$

where, W_i is the weight, V_i is the current value, and T_i is the target value. Hammer optimization is a very powerful optimization tool which should be definitely used once the minor design modifications are completed. It helps in fine tuning the details of an optical design. Usually the variables are set for the 'radius' & 'thickness' parameters. Further to it, the material itself could be substituted as variable, and zemax will suggest the material which meets the design requirements as per operand target setting.

In NISP, the goals in the first stage were to achieve the full FOV of the detector (can be seen from the Footprint diagram), reduce the spot radius and minimize the aberrations. The full FOV of the detector was achieved by using the operand **WFNO** in merit function editor and putting its target value as 5, which means the camera optics is required to demagnify the focal plane image and fast focus to F/5 beam. Once it was optimized with this criterion, the full diagonal FOV of the detector was achieved. Second was to reduce the spot size at the image plane. Here, it is important to define a set of surfaces realised by Zemax, i.e., '*worst offender surfaces*'. These are the surfaces which are more sensitive to any perturbations done to their surface parameters, and vary the criteria more by small changes in them. The primary criteria defined in the Optimization wizard was set to "Spot size, and then all the thickness and radii of the worst offender surfaces were put variable, with constraints on the same by operands defined by **CTGT** & **CTLT** (center thickness greater/less than) alongwith the surface numbers mentioned in the merit function editor. The other constraints were placed on the thickness of lens materials using **MXCG** (maximum center thickness inside glass), **MXCA** (maximum center thickness in air) & **MXEG** (maximum edge thickness inside glass). A typical merit function editor window is shown in the Figure 3.13.

3.5 Design Structural Flow

The planning of the different modes of NISP is a significant step taken for a streamlined implementation of a multi-mode instrument. The different operational modes selecting components are placed in the aperture wheel at the Cassegrain focal plane, and the filter wheel around the pupil plane area. The pupil plane is defined as the location where the image of primary mirror is reimaged by the collimator optics. The entire

Wizards and Operands Merit Function: 0.0107083033725747

Optimization Wizard
Current Operand (16)

Optimization Function
 Criterion: Spot
 Spatial Frequency: 30
 X Weight: 1
 Y Weight: 1
 Type: RMS
 Reference: Centroid

Pupil Integration
 Gaussian Quadrature
 Rectangular Array
 Rings: 3
 Arms: 6
 Obscuration: 0

Boundary Values
 Glass Min: 0 Max: 50 Edge Thickness: 0
 Air Min: 0 Max: 1e+03 Edge Thickness: 0

Start At: 5
 Overall Weight: 1
 Configuration: All
 Field: All
 Assume Axial Symmetry:
 Ignore Lateral Color:
 Add Favorite Operands:

OK Apply Close Save Settings Load Settings Reset Settings

	Type	Wave	Hx	Hy	Px	Py	Target	Weight	Value	% Contrib
1	WFNO						4.900	1.000	4.900	5.562E-05
2	BLNK	Distance to Pupil Plane								
3	GLCZ	14					2411.448	0.000	2100.136	0.000
4	DMFS									
5	BLNK	Sequential merit function: RMS spot x+y centroid X Wgt = 1.0000 Y Wgt = 1.0000 GQ 3 rings 6 arms								
6	BLNK	Default individual glass thickness boundary constraints. No air constraints.								
7	MNCG	37	46				8.000	0.100	8.000	0.000
8	MXCG	37	46				15.000	0.100	15.000	2.493E-07
9	MNEG	37	46	0.000	0		4.500	0.100	4.500	6.187E-07
10	MNCA	37	46				10.000	0.100	10.000	3.406E-06
11	MXCA	37	46				80.000	0.100	80.000	0.000
12	TTHI	37	46				150.000	0.000	205.588	0.000
13	TTHI	14	46				0.000	0.000	730.860	0.000

Figure 3.13: A snapshot of the Merit function editor of NISP imaging design.

field rays cross each other at this place, and hence any optical component situated near it will see the full field from the focal plane. Since the width of pupil is small, this is best suited for placement of gratings, broadband filters, Wollastons etc. In many of the IR instruments, a cold mask & pupil viewer is placed at the pupil plane, since the emission from the support system of secondary will form a major source of thermal background.

A full plan of the filter wheel assembly is described in the Figure 3.14.

Aperture Wheel	Filter Wheel 1	Filter Wheel 2	Filter Wheel 3
2 Slits	Y, J, H, Ks Broadband filters	Y, J, H, Ks Grisms	WeDoWo
1 Focal plane mask & 1 WGP	1 Open	1 Low res. grism	Cross-dispersor
Open	1 Block	1 Open	3 narrow-band filters
Block			1 Open

Figure 3.14: The filter wheel assembly of NISP

With reference from the filter wheel assembly, the functioning of the imaging, spectroscopy & polarization modes will be incorporated in the following manner. The *imaging mode* includes the aperture wheel as ‘open’, and the filter wheel 1 & 3 used with the specific filter. The filter wheel 2 will be at ‘open’ position too. The *spectroscopy mode* can function in two sub modes. One is the single mode at intermediate resolution and other is low resolution mixed mode. To implement them, the aperture wheel is occupied with the ‘slit’ of a particular width. For the single mode spectroscopy, the filter wheel 1 will have broad band filters Y, J, H, K_s as defined by Tokunaga³ in conjunction to the specific grisms in filter wheel 2, and the 3rd filter wheel as open. To utilise low resolution mixed mode (open for 1st filter wheel), filter wheel 2 houses a low resolution grism, R ~ 500 which will be combined with a cross-dispersor in the filter wheel 3. In the *imaging polarimetry mode*, aperture wheel will switch to ‘focal plane mask’ or ‘WGP’ depending upon the need for calibration. In filter wheel 1 the broadband filters will be used alongwith WeDoWo in filter wheel 3. The 2nd filter wheel will be open. A ‘cold block’ is given in the 1st filter wheels for operational advantages. The aperture wheel with slits should not be disturbed in the midst of observations, if dark frames need to be taken, as it may lead to shift in spectrum. Hence, to comply with this requirement, it is always good to have a block in one of the filter wheels which doesn’t contain the grism. Figure 3.15 gives a flow diagram of these operational modes.

³http://www.ifa.hawaii.edu/~tokunaga/MKO-NIR_filter_set.html

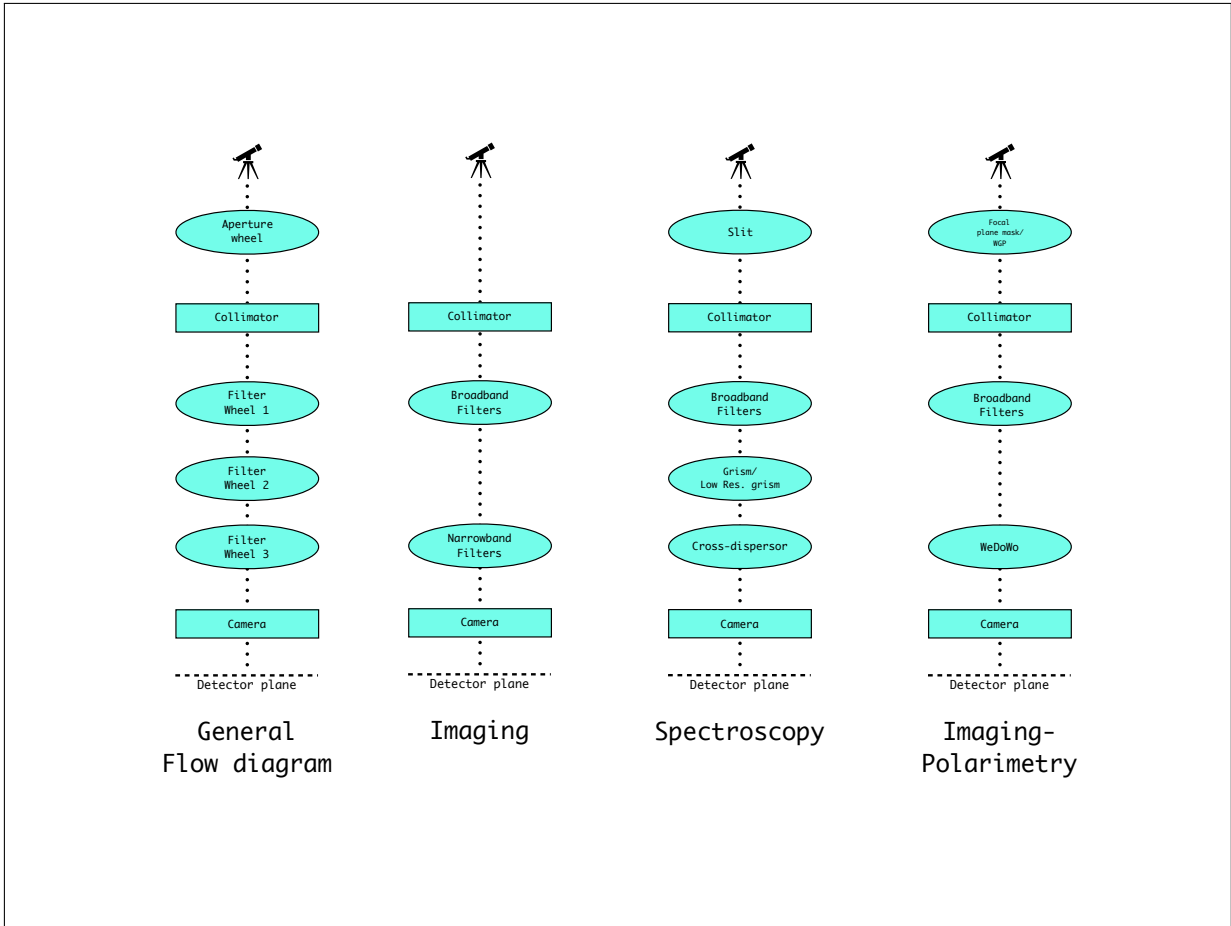


Figure 3.15: Schematic detailed description of the different modes of NISP and their functionality

3.6 Summary

The chapter showcases the various tools available in *OpticStudio Zemax* for carrying out a comprehensive analysis for an optical system. It also summarizes some of the techniques available to an instrument designer. It describes the design parameters in the optical design of the NISP instrument. A complete description of the multiple modes of NISP & their implementation has also been explained.

Chapter 4

Imaging Optics

"A picture is worth a thousand words"

Astronomical imaging has always been the most attractive subject for people. The advancement of detectors from the early era of glass plates to film, and eventually digital CCDs etc is remarkable. Even the shift from CCDs to CMOS arrays is quite remarkable. The detectors specification are chosen based upon the requirements of our design and the scientific parameter targets. The optics design is the main part which acts as a bridge between the telescope delivery and the detector potential. Hence, the optics design need to cater to all the necessity of the requirements of the instrument.

4.1 Overview of the imaging optics

Imaging optics requires mapping object points in one plane with the image points in other plane. The visualization and implementation of the imaging design should be of prime importance to avoid any defect in the system. The systems for imaging are mostly either composed of direct CCD imagers, or simple objective lens leading to the detector,

or a combination of lenses acting as objective lens system and then a reimaging optics which projects the image on the detector plane. All these methods provide desired performance and differ because of the underlined parameters to be achieved. We opt for a re-imaging optics consisting of collimator & camera system in NISP design. The main reason behind the choice of this setup is to de-magnify the image at telescope focal plane and enhance the performance by including other optical components. The demagnification factor is ~ 0.62 , given the F/8 collimator beam imaged by a F/5 camera beam. The Fig. 4.1 shows the full layout of the instrument, as the backend instrument to 2.5 m telescope. The design included the following operating parameters:

- The entrance pupil diameter = 2500 mm.
- Wavelengths = $0.9 \mu\text{m}$, $1.25 \mu\text{m}$, $1.635 \mu\text{m}$, $2.15 \mu\text{m}$ & $2.5 \mu\text{m}$
- Field definitions = 0° , 0.03° , 0.083° & 0.12°

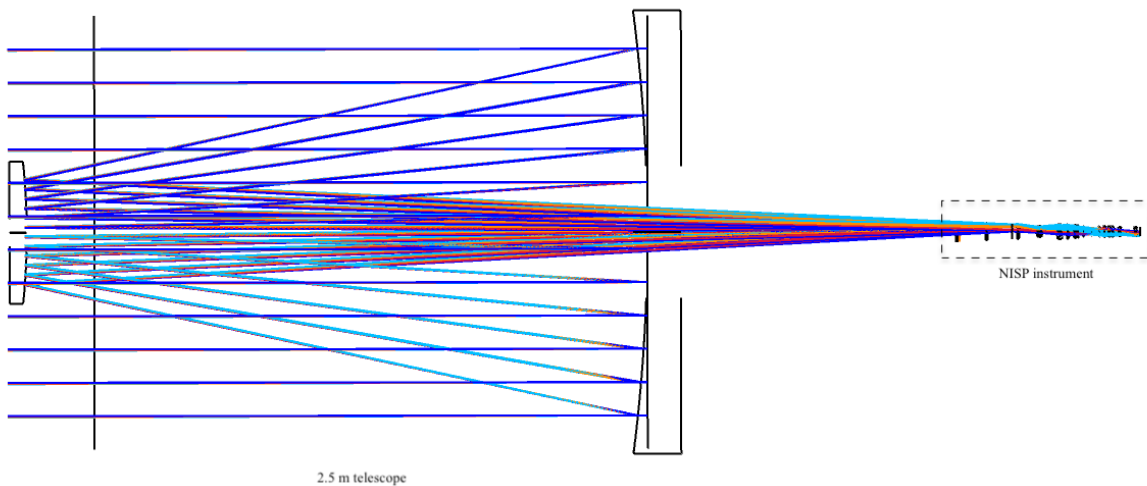


Figure 4.1: NISP instrument optical design as backend to 2.5 m telescope

4.2 Collimator Optics

Collimator is a crucial part of an imaging design, which consists of a set of lenses that makes the diverging incident beams, parallel on exit. The rays which come from the telescope cover a large area on the Cassegrain focal plane for our definitions of full field of view, thus requiring larger collimator lenses. This means that the semi-diameter of these lenses will be close to 50 mm for the 2.5 m telescope. It also requires the system to be un-vignetted, hence the f-number of collimator should be equal to the f-number of telescope, to allow all incident light to pass through the collimator. Upon exiting from the collimator, this beam width is reduced to a parallel beam with a smaller radius. This reduction in the beam width, helps an optical designer to fit in important optical elements required for operating different modes in the instrument. This position within the design where the rays from different field angles cross each other is called the "Pupil", and different optical elements e.g.- grisms, filters etc are placed here.

Journeying through the optics design is a continuous learning experience as one explores the minute details necessary for achieving the specifications. The NISP final collimator design was established following several iterations of various approaches. The instrument design comes to a length \sim of 740 mm, and the number of analysis and re-runs of optimizations done in this length to make the optical design perfect are explained below. Some of the promising design approaches considered include:

- 1) We start with a set of lenses defined in the lens data editor. The materials included those preferred for IR wavelength i.e., CaF₂, BaF₂, LiF, ZnSe, ZnS etc. One needs to decide the power distribution to each surface of the lenses, to get a perfect collimation as required. The next step is to define the Merit Function Editor for the operation. The operands were chosen so as to minimise the merit function value, which means achieving a good design. Apart from defining the usual operands for air and glass thickness, and semi-diameters on lenses, a new operand was chosen for collimation. The operand "RAID" i.e. real ray angle of incidence, defines the angle between the surface normal and incidence ray at the surface. The surface chosen for the incidence angle definition was the pupil stop, and the paraxial and marginal rays angles were defined following simple trigonometry. Though RAID is very good for producing telecentric systems, the

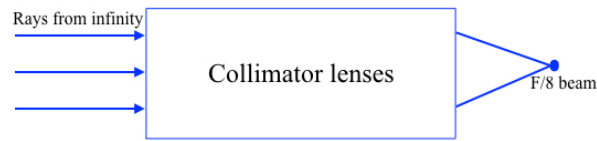


Figure 4.2: Schematic of the collimator design approach.

problem we encountered here was non-uniform collimation. The RAID operand leads to “pupil dilation” which causes the width of pupil to increase as we go from central to extreme field rays.

2) We will be using this approach to achieve collimation performance in our instrument, NISP. This shall be called the *inverted approach*. We designed the entire collimator set of optics, by giving a collimated beam i.e., parallel rays as input to the lenses to get an F/8 beam as the output to this system to match the F-ratio of our 2.5 m telescope. The Merit function needs to be devised in a manner to give us diffraction limited spot size at the output of this system. Once we achieve that, the set of lenses are reversed, and therefore, the input becomes the output & vice-versa giving us the collimator optics. The fields defined in this approach were under the head “Paraxial Ray Image Height”, and the y-coordinate values were known from real ray tracing for the particular surface and field point. A flow diagram (Figure 4.2) to clarify this approach is shown below : As seen from the flow, once the F/8 beam is achieved, i.e. WFNO equals 8 in merit function, and the desired spot sizes are as it comes at Cassegrain focal plane of the telescope, we are ready to reverse the design. Following this procedure, the collimator design is completed.

In the NISP design, we had started with a set of 6 lenses. We had used INFRARED.AGF, SCHOTT-IRG.AGF, 77&RT.AGF catalogs available in zemax for infrared materials. The information of the refractive index for the glasses was noted from <https://refractiveindex.info/>. For a quick glance, the refractive index information for the lenses used in NISP instrument are tabulated in Table 3.2. With the lens splitting, the final number of lenses in the collimator design is 8, with two sets of triplets within the design.

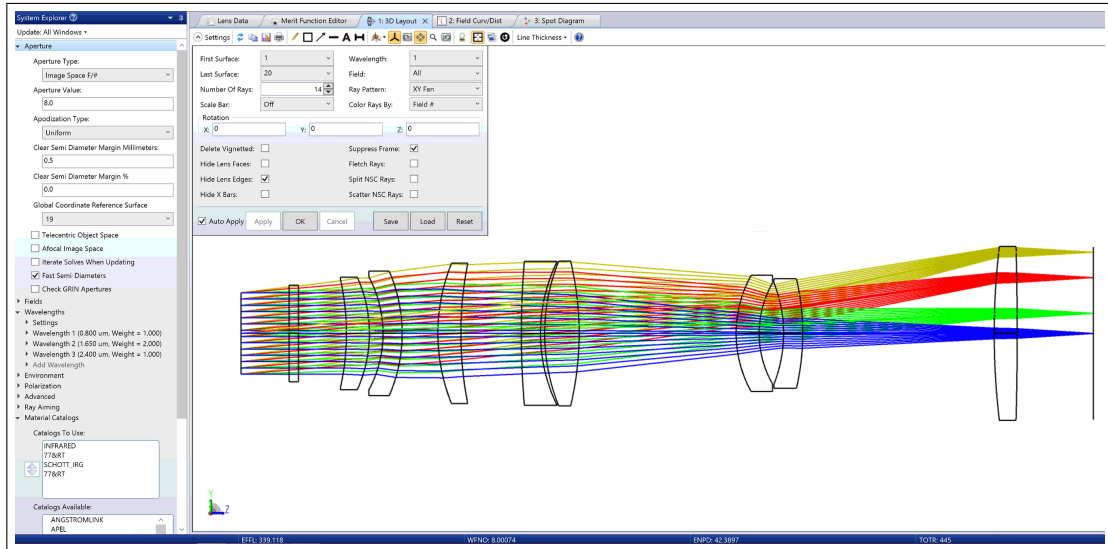


Figure 4.3: Zemax window showing the collimator layout, aperture settings, wavelength settings done for the final design.

Setting up the variables

In Zemax, to optimize the design, we need to define variables whose values are allowed to change during the course of optimization. It's a common practice to start with putting 'V' for mostly all the radii & thicknesses for the elements defined. The optimization process helps us to reach closer to our desired target value, by modifying these 'V' numbers. The next very quick setting to achieve good performance further after these changes is by setting 'V' for materials. The chosen lens materials are defined based upon the refractive index 'n', Abbe number 'v' & deviation of partial dispersion 'dP_gF'; whose values can be 'modelled' or 'substituted' during the variable setting. On substituting it, Zemax selects glass materials with similar properties from the already defined catalogs in 'catalogs to use' tab. This operation has the potential to improve the finer details of our design. The preferred optimization at this point is 'hammer optimization', which is run for several hours in 'auto-update' mode to see if significant changes are also happening to the design and its spots etc.

The main settings done for the collimator design in NISP are,

1. The aperture type was set to 'Image space $F/\#$ ' with the value set to be 8.

2. The aperture of all the elements was set to 'circular'.
3. The weights on wavelengths were distributed with the H band given larger weight than others.
4. The semi-diameter of the lenses once the design was reversed, was set to 'Automatic' to prevent vignetting.
5. The 'V' (variable mark) was removed from the parameters it was defined for all collimator lenses, to make those lenses fixed and hence prevent them from modification during further design analysis.

With all these settings the total length of collimator comes to be 445 mm. This entire set of lenses was reversed and then added to the 2.5 m telescope optics. The design of unreversed & reversed collimator setup is shown in Figure 4.4. The spot size for the Cassegrain focus shows that we could achieve the required collimator specifications.

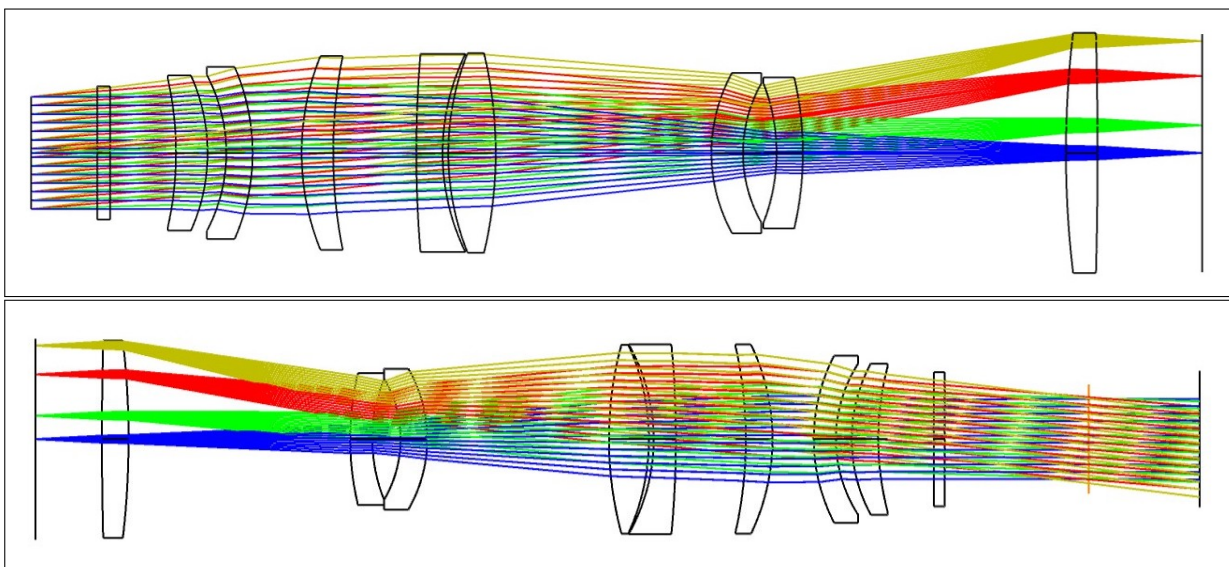


Figure 4.4: The design approach from a reversed input design (top) to NISP collimator design (bottom)

4.3 Stops & Pupils : Placement of Filter Wheels

Stop is a physical aperture in an optical system. It limits the aperture of the system by allowing the bundle of rays within stop width to pass through it and restricting others outside it. Pupils are the images of the aperture stop from a point on the optic axis, in the plane of object. Pupil location serves as an important point for multiple reasons :

- Pupil is the location in an optical design where the rays from different fields cross each other. There are 3 types of pupils in any optical system - entrance (EP), intermediate & exit pupil (XP). The intermediate pupil is also called as the aperture stop. Any optics kept at this point will see the unvignetted beam. This place is considered to be ideal for placing filters, gratings, polarizers etc. Owing to the narrow size of pupil, as compared to collimator optics, it is more realisable to design transmitting optics here to serve the purpose of imaging or spectroscopy or polarimetry. While defining these stops & pupils, one possibility to be explored is vignetting in the system. Vignetting, i.e., darker corners of the images occurs if a beam of light is intercepted by apertures other than the stop defined. Usually, the top and bottom end of the beam gets clipped off due to the clear apertures of the lenses used for collimation or camera, which blocks the off-axis rays. By definition, the stops and pupils don't let vignetting to occur, but if the location of exit pupil doesn't include all off-axis field rays, system is again vignetted.
- Pupil plane in an Infrared system has another very important purpose to fulfil. It is the place where an image of the primary mirror along with a view of the secondary and its' support structures is obtained. Thus this location can be used effectively as a cold pupil stop to block the thermal radiation coming from the support structures which can contribute significantly to the background light in the longer wavebands (K filter in our case). In our system, it has been located between the 2nd & 3rd filter wheels.

In NISP, the width of pupil is ~ 38 mm. Referring to Fig.4.4 bottom design, the right side of the system shows an orange vertical line. This is considered as the intermediate pupil, and the location for placing filter wheels. The footprint diagram (Fig. 4.5) at the

pupil surface shows that all the fields are overlapping circles, which means that fields are crossing each other at that point.

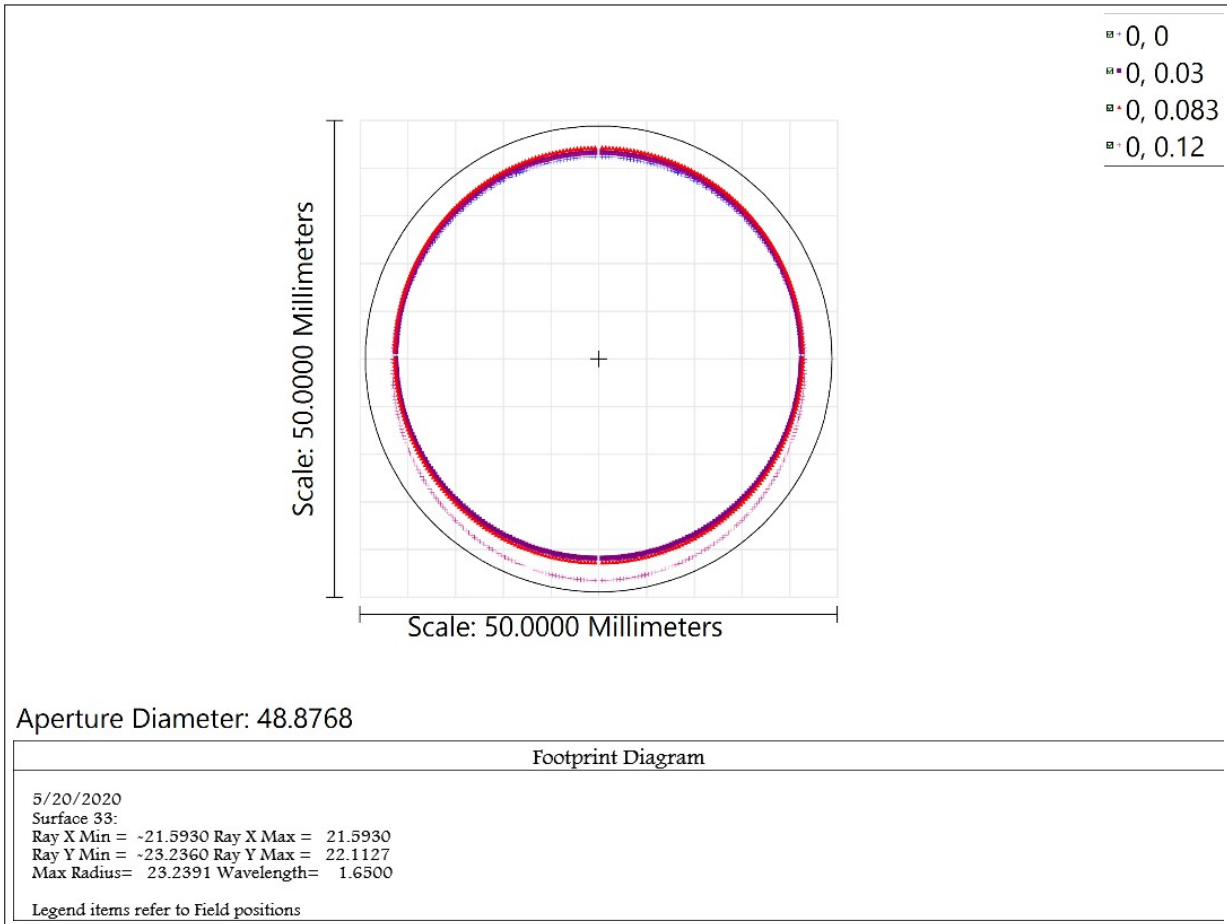


Figure 4.5: Footprint diagram where the different circles reveal individual fields, and the diameter denotes the width of the pupil.

4.4 Camera Optics

Camera lens consists of the focusing optics. They are added after the filter wheels, to re-focus the intermediate image at the telescope focal plane on the sensor. The focal length of the camera system decides the magnification of the entire system. If the collimator-camera system has a 1:1 ratio, there is no magnification. But if the collimator-camera system has value $\neq 1$, it result in magnification/de-magnification of the image at the

sensor. The term magnification here is defined as,

$$M = \frac{f_c}{f_e}$$

where, f_c and f_e are focal length of the collimator and camera optics respectively. A de-magnified image means more field of view (FOV). Quoting this, a few parameters of major interest become the spatial resolution and point spread function (PSF) of the point astronomical sources. The spatial resolution for a sensor is defined considering the 'Nyquist criterion', which is a finite rate at which a signal needs to be sampled to retain the information. The sampling frequency should be greater than twice the maximum frequency present in the signal, and this rate is called the Nyquist rate. Any sampling frequency lower than the Nyquist rate, makes the signal to be attenuated and hence 'aliasing' which means loss of signal occurs. A very informative discussion is offered on the similar topic in [Willey \(1992\)](#). In astronomy, 2 pixel sampling is considered for imaging a point source to provide good spatial resolution. Spatial frequency, in this case the Nyquist frequency (f_N) and cut-off frequency (f_c) are defined as,

$$f_N = \frac{1}{2p}$$

$$f_c = \frac{1}{\lambda N}$$

where, p is the pixel size, N is the $f/\#$. The region lying between $f_N < f < f_c$ is the aliasing region. It is said that images are limited by the sensors and not by the optics. The spatial resolution is noted in terms of pixel scale, in pixellated arrays. For a ground based instrument, this value is decided based upon the seeing of the location. The PSF due to seeing is sampled into 2-3 pixels, and the value per pixel is termed as the pixel scale. For any telescope, the plate scale defines the linear scale for the angular projection of an object in the sky. This value is easily calculated from the focal length

of the telescope,

$$PS = \frac{206265(\prime\prime)}{F(mm)}$$

The plate scale is defined here in units of $\prime\prime/mm$ at the Cassegrain focus of the telescope. Pixel scale is defined by the seeing of the place. We need to divide the PSF into 2-3 pixels. Based upon, the defined pixel scale, one gets the total FOV over the detector plane.

In the context of NISP, we have designed a system which demagnifies the telescope focal plane. The F/8 beam is converted into a F/5 beam to achieve a $10' \times 10'$ FOV on the detector plane. The detector used is a H2RG array with pixel size of $18\mu m$. The plate scale at telescope focus comes to be $10.3\prime\prime/mm$. Owing to an average seeing of $\sim 1\prime\prime$ at Mt. Abu observatory, the pixel scale comes to be $0.3\prime\prime/pixel$. The plate scale at the detector plane is $16.6\prime\prime/mm$, for a detector size of ~ 37 mm.

In defining the detector plane in Zemax, one needs to define it diagonally to avoid any vignetting which may otherwise occur at the corners. Since, the definition is for a semi-diameter, we need to assure that our square detector diagonal length equals to the diameter of the circular aperture. In this way, to achieve a $10' \times 10'$ FOV on detector plane, we actually defined a diagonal FOV of $14.5' \times 14.5'$. The camera lenses include one set in which lens splitting was utilised.

4.4.1 Cryostat Window

A cryostat window is an important part of an Infrared instrument. Since these instruments are maintained at a cool temperature (*using liquid nitrogen*) as per the detector requirements, a cryo window is required to maintain vacuum. The placement of a cryostat window is before the Cassegrain focal plane. This is very crucial to note, that the placement of the window in the converging beam leads to slight variation in the focus. We have looked into the options of several materials for the cryostat window, for eg., CaF_2 , *fused silica*, *sapphire*. Out of these we opted to go ahead with 'fused silica' for

our requirement, due to its easy availability, and good transmission in the NIR range. The dimensions of the window are 11 mm width with a diameter of 100 mm.

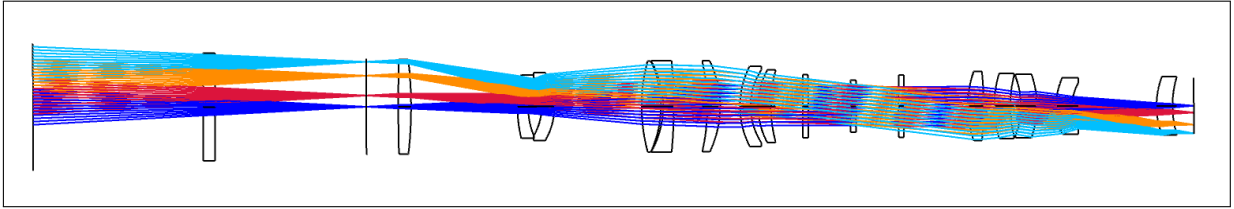


Figure 4.6: NISP instrument optical layout showcasing the cryostat window placement before Cassegrain focal plane.

4.4.2 Imaging layout

The imaging design for NISP had two variants based upon the lens materials for the camera optics. The materials differed because of the independent ‘hammer optimization’ applied on different camera lenses to change the materials for best match of our specifications. The further sections will discuss both the designs & their analysis, thereby leading us to choose the more suitable one for our requirement.

The layouts *a* & *b* (Fig 4.7), are a representation of the imaging optics of our instrument NISP, from the Cassegrain focal plane to detector plane. The colors symbolise the different fields defined to cover the full FOV. The materials are labelled over the lenses to show the difference in the camera optics. The imaging specifications of the instrument are tabulated in Table 3.1.

4.5 Analysis of Imaging Optics

In an optical design, the design performance requirements are specified by spot diagram, encircled energy, aberrations study, PSF, MTF and other similar measures. Analysis of a design is a comparison between the real aberrated image performance & theoretical limits for them. Zemax provides a suite of tools for carrying out the analysis to understand the system performance and to ensure better delivery of required

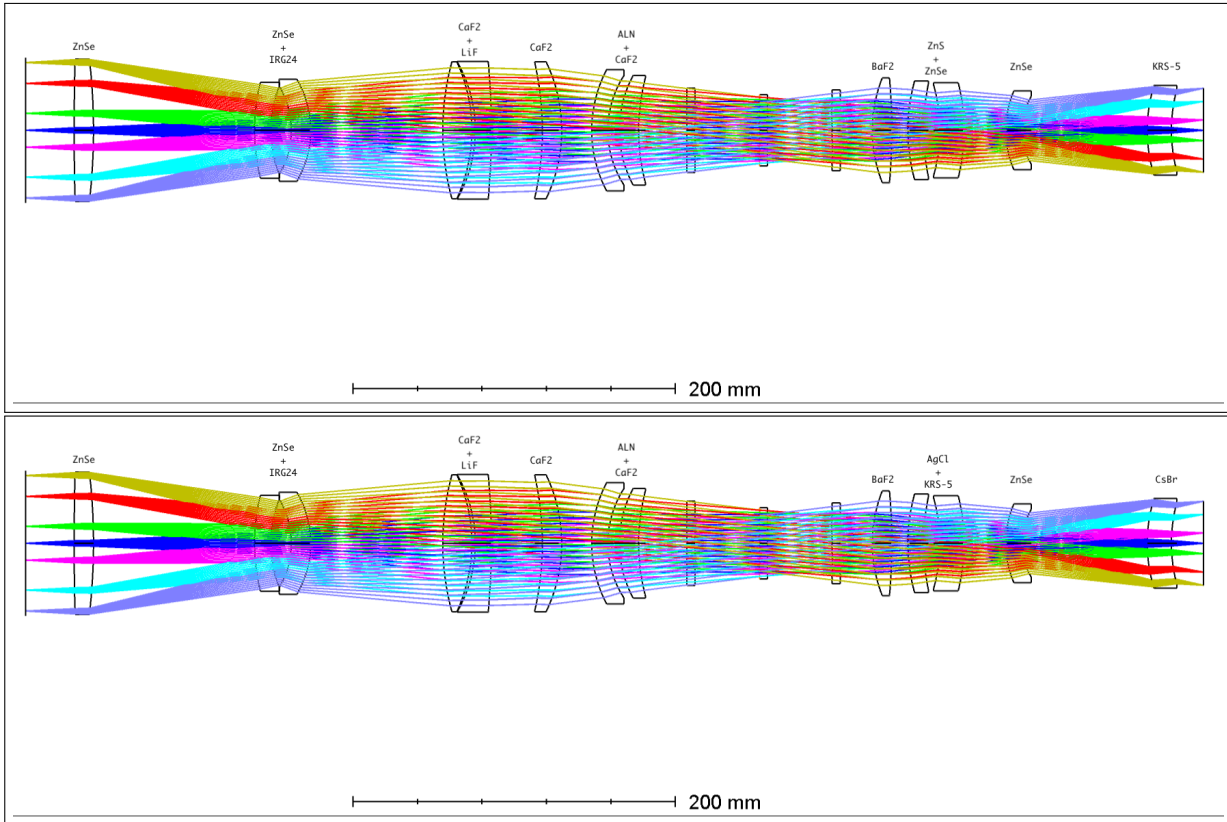


Figure 4.7: Labeled imaging optical design of NISP. The design will be referred as variant 1 for the top panel & variant 2 for the bottom panel.

specifications.

4.5.1 Spot diagram

It gives a picture to the projected beam points on the image plane in an imaging instrument. The spot size is a 2-D representation of the flux of rays falling in a particular fashion & different fields response on the image plane. It is important to understand how different wavelengths are distributed in the image, and strive to bring them to focus within the seeing limit.

From one glance at the spot diagram, one can deduce the aberrations present in the design and hence try to optimize in a way to get rid of them. Looking at the spot diagram in Fig.4.8, we can list few terms mentioned below in the panel i.e., Airy disk, RMS radius, GEO radius. The Airy disc radius tells the theoretical diffraction limited

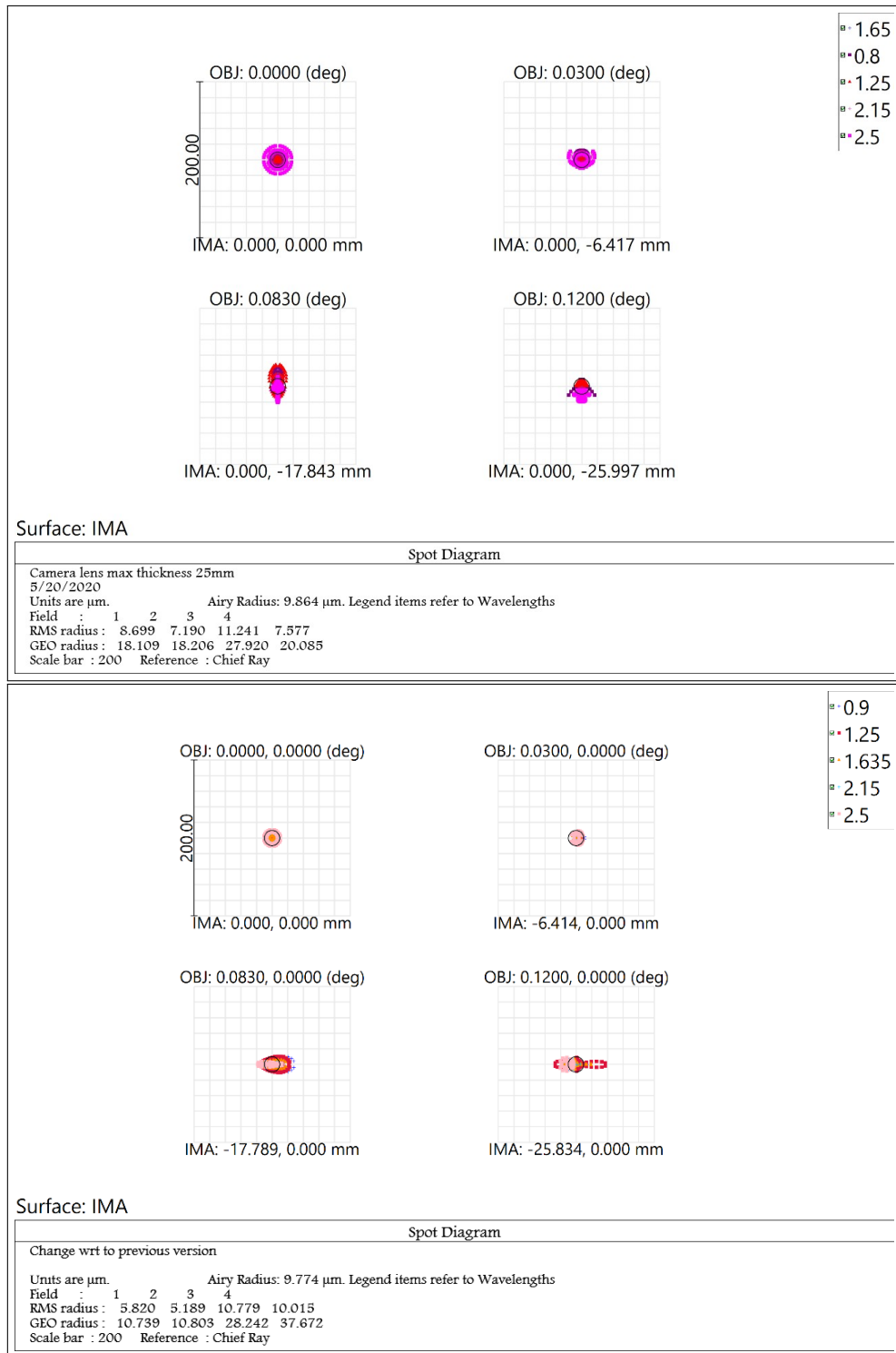


Figure 4.8: Spot diagram for the variant 1 (top panel) and variant 2 (bottom panel)

spot size that our instrument can achieve in the absence of atmospheric disturbances & aberrations. The RMS & GEO radius are the real aberrated radius of the design. For a perfect optical system, PSF is an Airy pattern which is derived from Fraunhofer diffraction theory. The core of the Airy pattern is termed as the Airy disc, which is

inside its 1st minimum. It contains the $\sim 90\%$ of the total light flux of the image. RMS radius is the realistic measure of the expected resolution including the aberrations. The GEO radius gives a measure of the total spread of spots on the sensor plane. The aim of a ground based design, from these specifications is to get RMS spot size of all the wavelengths (required for the instrument) within the seeing limited performance. Since, our ground based location cannot give us diffraction limited performance, and we aren't including adaptive optics in our design, so seeing limit is our performance goal. The spot diagram of Fig. 4.9 is at the telescope focal plane.

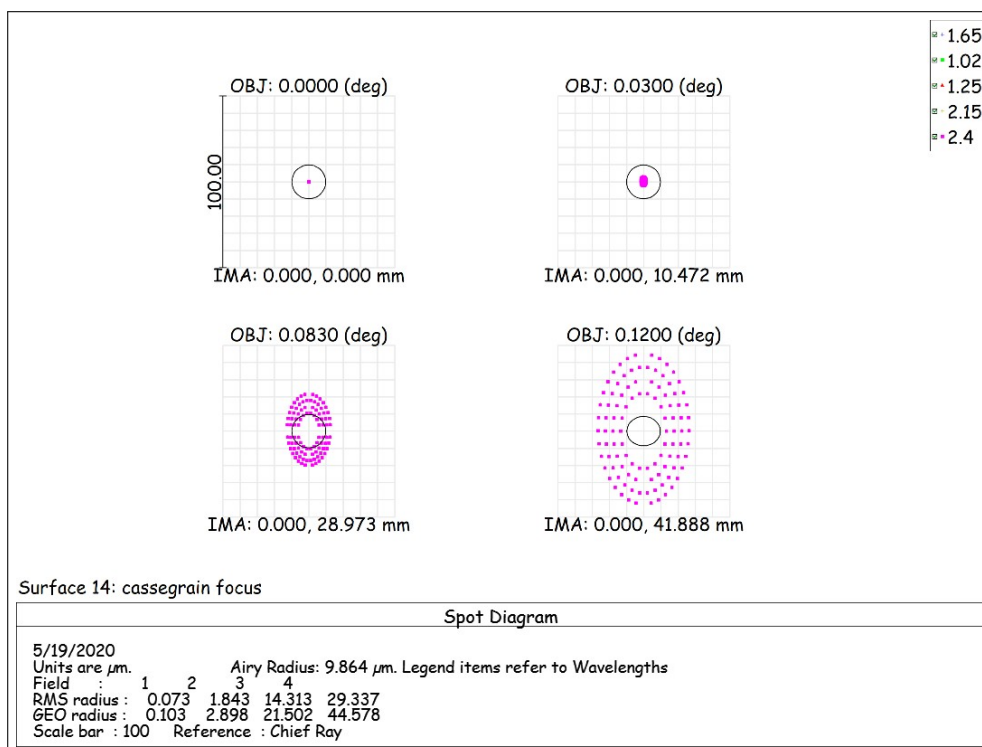


Figure 4.9: Spot diagram at the Cassegrain focus of the telescope, showing diffraction limited performance achievable by the telescope.

A fact to notice in the Fig. 4.9 is that the spot diagram of the two extreme fields, i.e., at 0.083° & 0.12° have sizes beyond the Airy disc, however they are within the seeing limit. This tells that the telescope might need a corrector lens for fields beyond this FOV for any instrument. Another very important tool for assessing the merit of the imaging design is by considering the field coverage over the sensor diametrically. As is evident from the 'Footprint diagram', Fig. 4.10, the fields labelled with different colors spread over the entire detector array, giving us a full circular FOV of $14.5'$. In terms of our square $2\text{K} \times 2\text{K}$ array detector, this FOV is equivalent to a diagonal length of

52.2 mm. At Mt. Abu, the typical seeing is 1". Considering that at times we may have

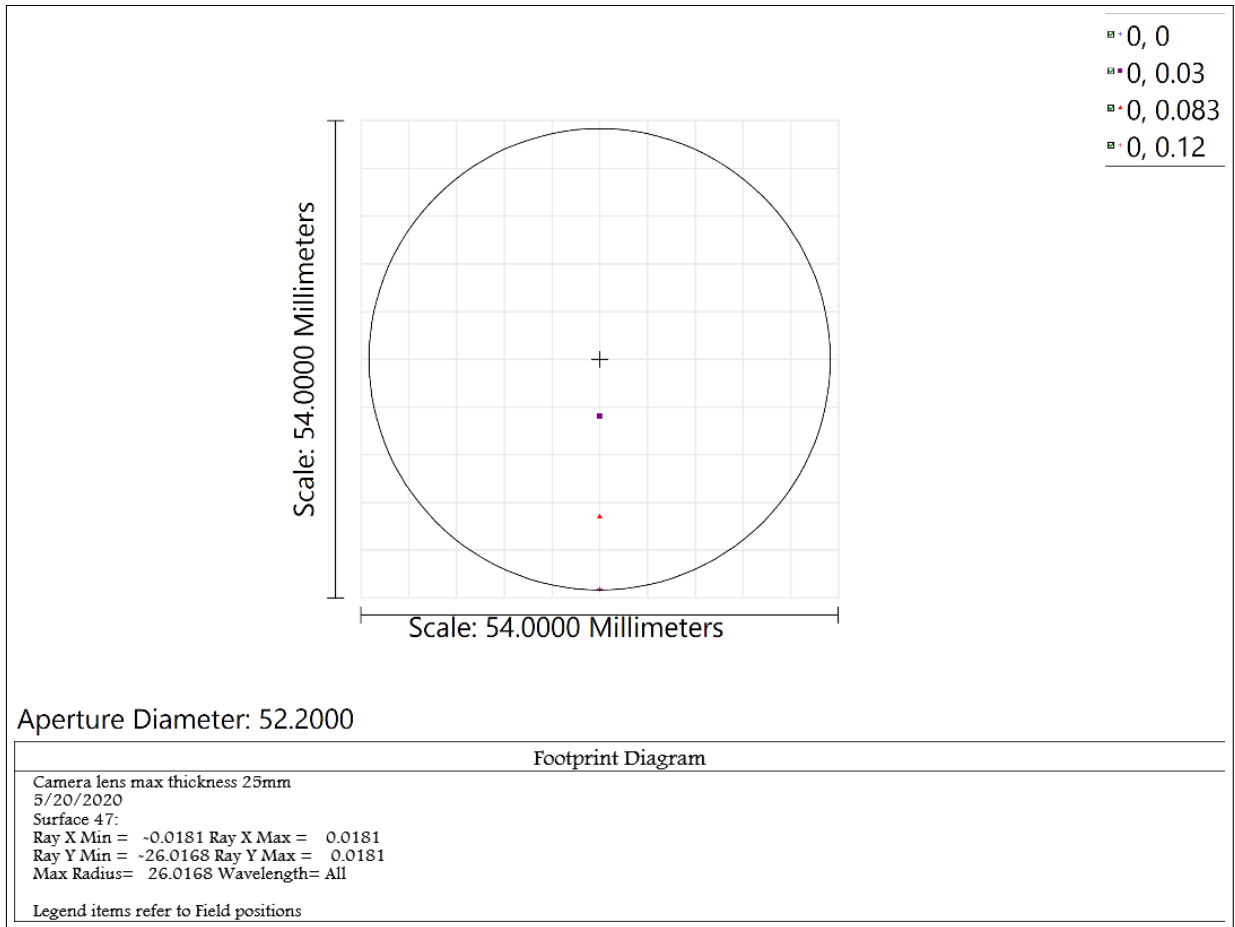


Figure 4.10: The footprint diagram showing all field points covering the diameter of circle

better seeing, we spread the stellar flux over 3 pixels so as to suffice Nyquist criteria of sampling even during better seeing conditions. The pixel size of H2RG being $18 \mu m$, seeing limit performance needs the spot to be less than $54 \mu m$. The design (Fig.4.8) shows that both the variants of the imaging optics design have all the spots well within the required specifications.

4.5.2 Diffraction Encircled Energy

It is a fraction of the total integrated flux in the image contained within a given radius 'r'. It measures the relative intensity in the diffraction PSF contained within a circle of specific size, centered on the PSF (Andersen, 2015). Another term with similar meaning is the ensquared energy, and it holds the same concept, but in terms of square apertures (pixels). A formulation for the encircled energy (EE) as a famous expression derived by Lord Rayleigh (1881),

$$\begin{aligned} E_c(p) &= \frac{1}{4\pi} \int_0^p \int_0^{2\pi} \left(\frac{2J_1(r)}{r} \right)^2 r d\theta dr \\ &= 1 - J_0(p)^2 - J_1(p)^2 \end{aligned} \quad (4.1)$$

where, p is the radius of circular pixel. From the Fig. 4.11, one can notice that the black color line is for the diffraction limited performance, and the other colors are meant for different field angles. It is evident that the distribution is mostly close to the diffraction limited performance. The size of one pixel being $18\mu\text{m}$, 50% energy should be within one pixel, and 80% within 2 pixels. Since the plot 4.11 has x-axis representing the radius from chief ray, 80% encircled energy is within 2 pixel (i.e. $18\mu\text{m}$ radius) for all the fields for both the design variants.

4.5.3 Effect of vignetting

The explanation of vignetting in a system has been described in the Section 4.3. The system shows full irradiance up till a radius 'r' which is termed as the un-vignetted FOV of the system. After this radius, the irradiance drops to some value, and then it drops to zero at fully vignetting aperture. From the plot in Fig. 4.12, it seems that the system is vignetted. The fraction of un-vignetting is 0.7-0.8 fraction of the full irradiance of the incident beam. Also, it can be seen that this fraction remains constant for the entire FOV

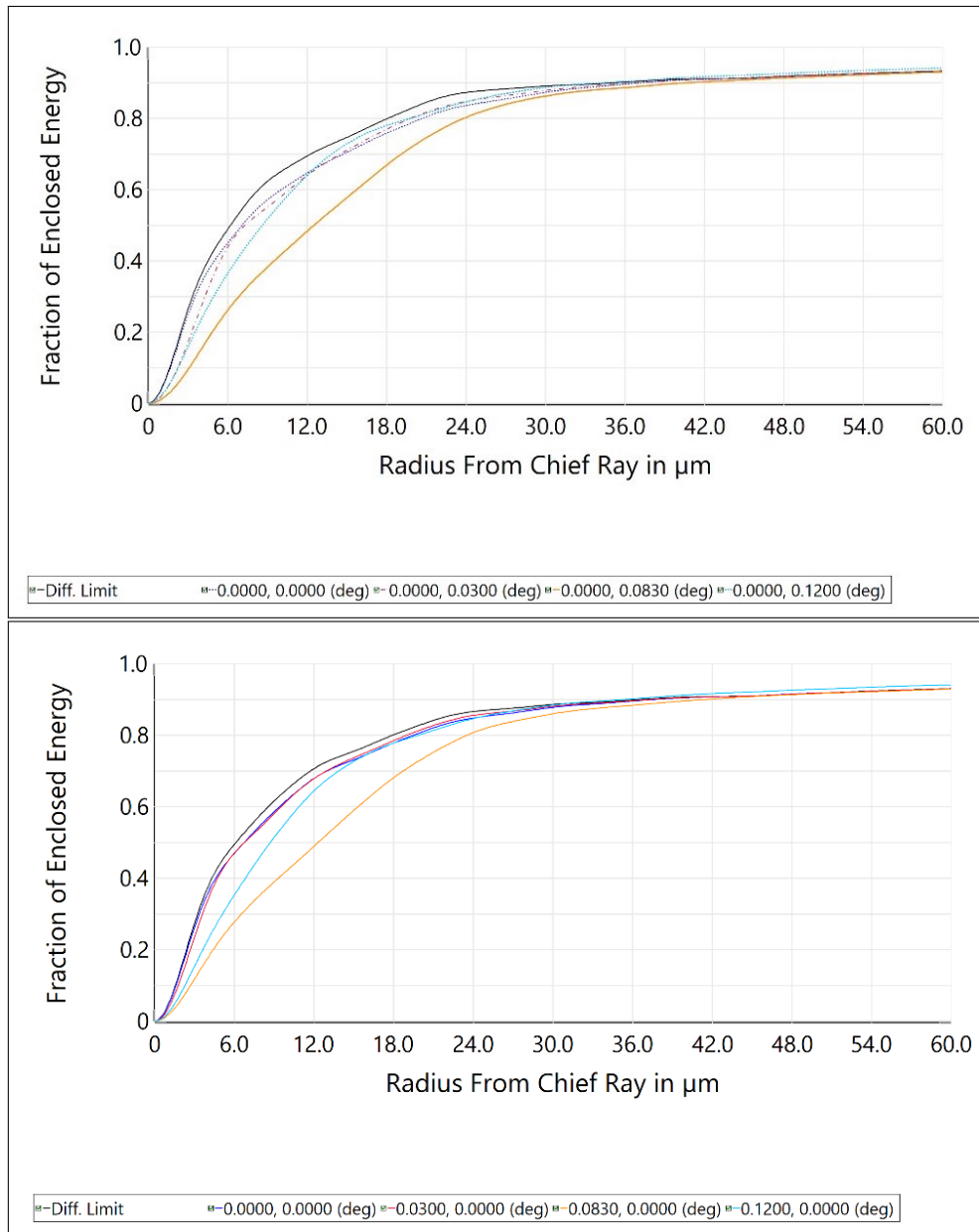


Figure 4.11: Diffraction encircled energy plot for variant 1 (top panel) and variant 2 (bottom panel)

of the NISP instrument, i.e. $0^\circ - 0.12^\circ$. But, the vignetting seen in the imaging design of NISP is not from the apertures defined in the instrument. The vignetting is happening due to the presence of 'circular obscuration' by the secondary mirror in the definition of the 2.5 m telescope. Hence, it is clear that the NISP design is not introducing any additional vignetting.

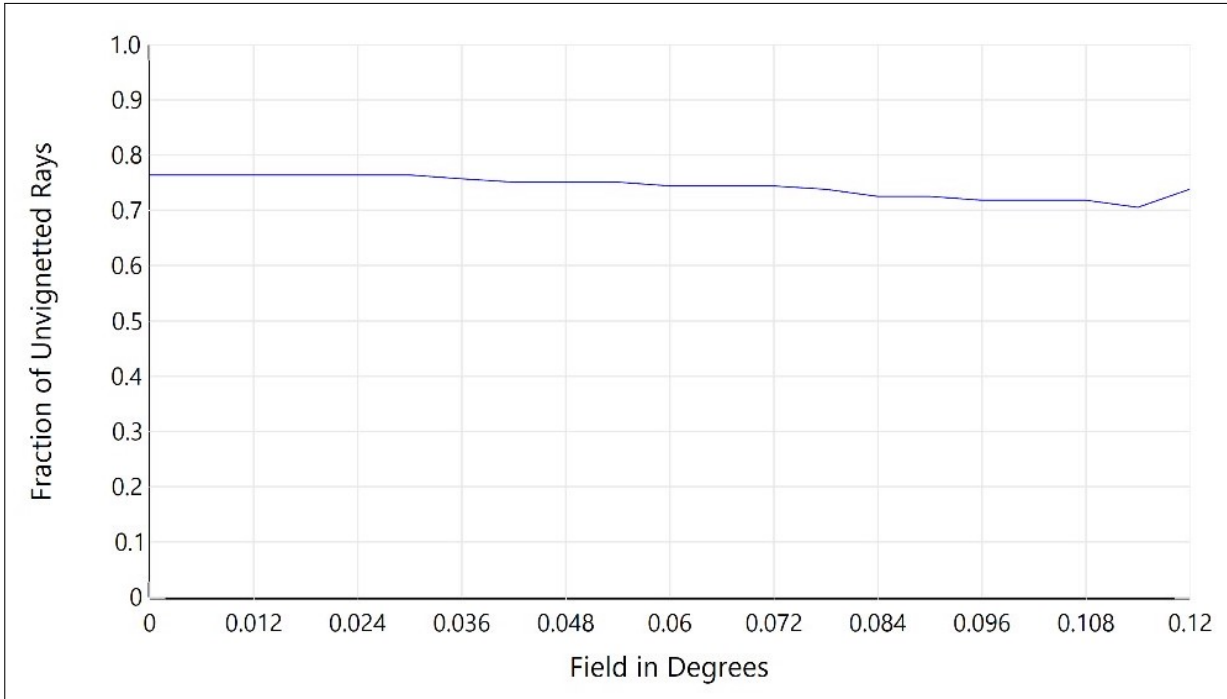


Figure 4.12: Vignetting plot of NISP

4.5.4 Modulation transfer function (MTF)

The modulation transfer function is the magnitude response of an optical system to different spatial frequencies. The analysis of the system in frequency domain makes use of sine functions, rather than discrete steps. MTF is a measure of the contrast of the system, over a particular spatial frequency. It is a link between the resolution and contrast of the system, as resolution is defined at a specific contrast. A measure of the MTF as a variation of the irradiance is defined as,

$$M = \frac{I_{max} - I_{min}}{I_{max} + I_{min}}$$

The combined system MTF, is defined as a sum of the MTF from each component within the optical system. The imaging system consists of detectors, where the final imaging performance is understood. The pixels are divided into line pairs, to properly resolve a dark & white patch falling on adjacent pixels. The width of one line pair is used to define the spatial frequency of the system, upto which the MTF needs to be measured. The Figure 4.13 shows the MTF plots for the two NISP imaging designs.

The black line is for the diffraction limit MTF for the system. If we compare the MTFs of the two designs, the top plot (i.e. variant 1) shows that the MTF of different field angles (defined by different colors) are far from the diffraction limited performance. The bottom plot (i.e. variant 2) MTF is very close to the diffraction limit performance for almost all the field angles. This means that there is a scope for further improving the MTF of variant 1 by continuing the optimization for the design, but for the other variant the contrast of the system is already very good.

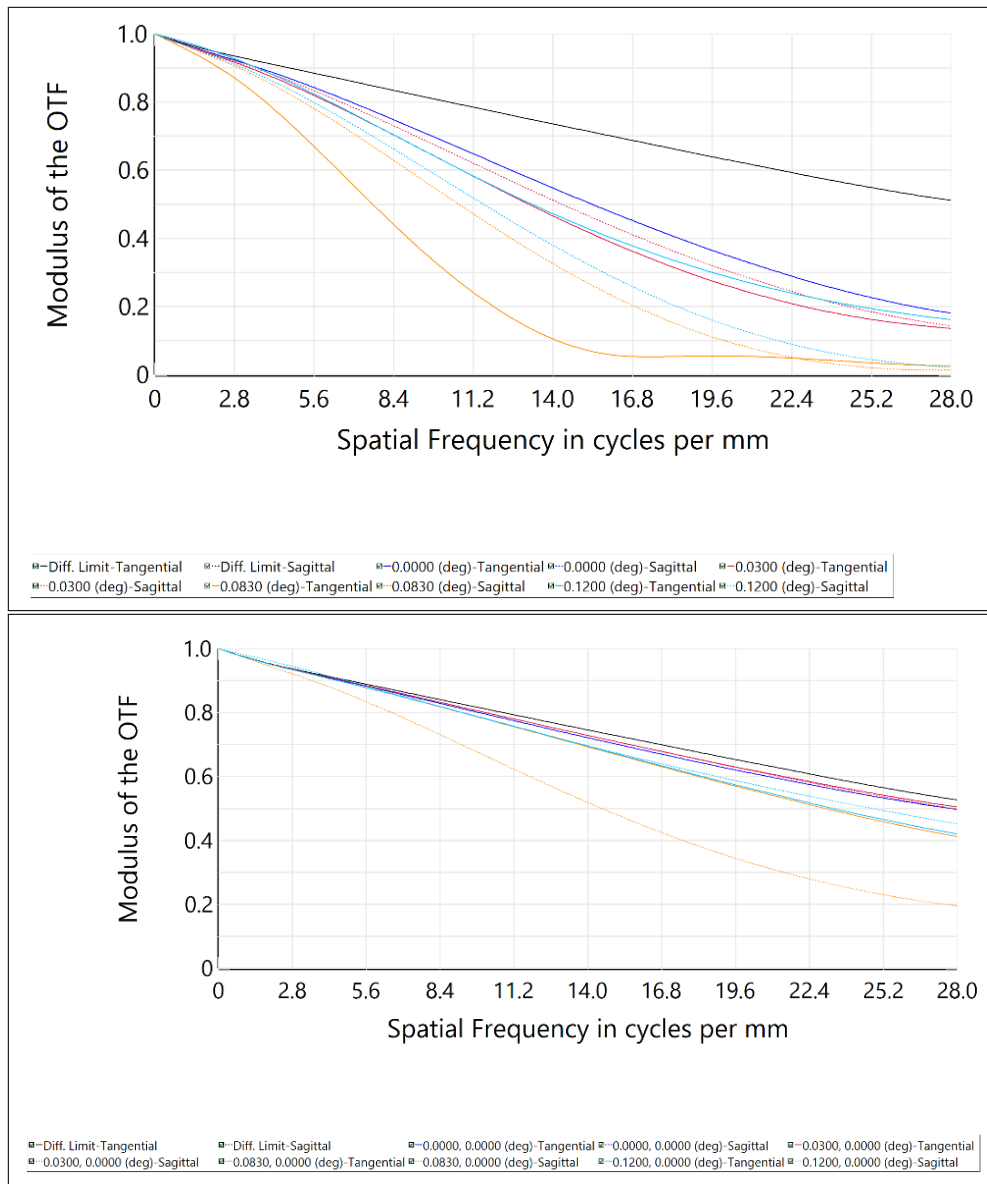


Figure 4.13: The MTF plot for the imaging design of NISP for variant 1 (top panel) and variant 2 (bottom panel).

4.5.5 Wavefront Map

The wavefront map gives us a measure of all the aberrations present within an imaging design at the final image plane. The wavefront map for NISP for on-axis & at extreme field position is shown in Figure 4.14. The image of the spider support structure is seen at the center of the wavefront. The wavefront maps reveal that the on-axis & off-axis

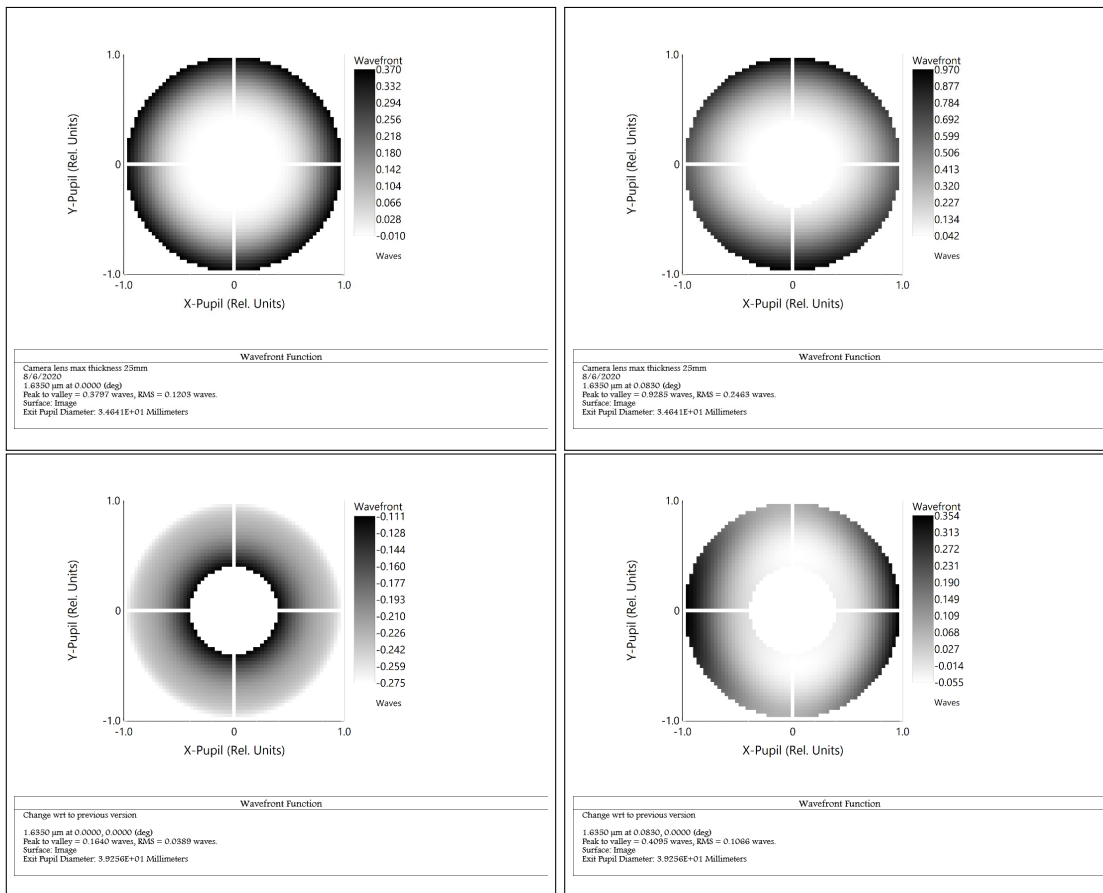


Figure 4.14: Wavefront map for the central and extreme field for NISP. *Top panel:* On-axis & off-axis maps from variant 1, *bottom panel:* on-axis & off-axis maps from variant 2.

performance of variant 1 has large variation in the peak to valley, for the image at the detector plane. If we see the bottom panel (variant 2), the map is smoother with minimal change in the peak to valley performance. Hence, variant 2 is the better option. The 4 arms and a central patch seen at the center for all the 4 panels comes from the image of spider & central obscuration for secondary defined within the telescope system.

4.5.6 Aberrations

An introduction to the topic of aberrations has been given in the Section 3.4.3. As seen from the equation 3.4, the non-linear terms in the Snell's law cause a deviation from perfect imagery. The aberrations in the design can be studied by monitoring the Seidel coefficients in Zemax. One can quickly look for a spherical aberration or coma present in the image from the spot diagram. In the presence of coma, the spot diagram for the extreme field shows a comet (tail) like feature. One more promising tool in zemax is the OPD fan & Ray fan plot, for estimating the presence of aberrations. Ray fan is the derivative of OPD fan plot. There is a presence of few aberrations even after removal of all the other aberrations from our optical system. The attached plot (Fig. 4.15), shows two of these aberrations, i.e., field curvature & distortion. Not seen directly though, but the same plot can be used to point out the presence of astigmatism in the design.

Field curvature causes the image of a plane object to be curved. It is considered to arise from 'power error' for rays at larger angles. Simplifying it, the extreme rays will see a higher power and the image off-axis points shall be closer to the lens. *Distortion*, occurs due to the dependence of linear magnification on off-axis distance. Magnification is a ratio of the image height to the object height. This ratio must stay constant over the entire optical system. From the definition of magnification, it is known that it is a function of focal length. If the focal length of the lens changes for different parts of the lens, magnification also gets disturbed. This causes distortion to occur in all parts of an image which are otherwise very sharply focused. *Astigmatism* occurs when rays travelling in two perpendicular planes have different foci. The two planes are denoted as the tangential and sagittal planes in zemax.

In NISP, the values of the field curvature for all the wavelengths covering the entire FOV of the instrument, comes to be ~ 0.2 mm. The deviation from the central zero location, shows that there is a defocus in the system. This was taken care of with a dummy surface to compensate for the 0.2 mm shift in focus. We are further minimising it with 'FCUR' operand in the merit function editor. The deviation increases chiefly towards the extreme field rays from 0.1° - 0.12° . The value of distortion increases from 0% - 2%

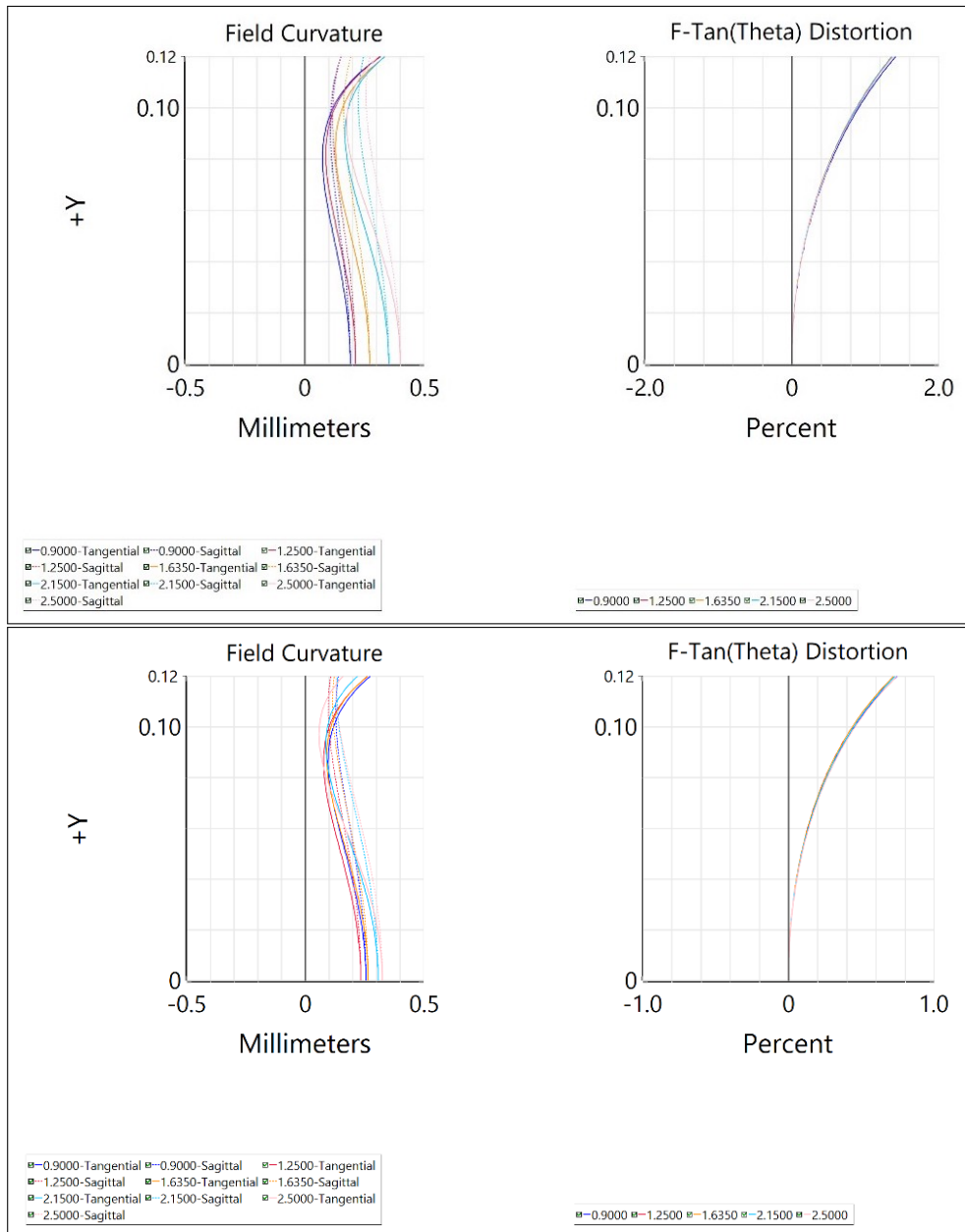


Figure 4.15: Plot showing the field curvature and distortion values for the two variants 1 & 2, top and bottom panels, respectively

as one goes from center to extreme fields for the variant 1 & goes till 1% for variant 2. As a benchmark for acceptable distortion within a system, 1% -2% distortion is not detectable. The negligible astigmatism in the design is visible from the small separation of the two rays (bold for tangential & dotted for sagittal) in the field curvature plot.

4.5.7 Image Simulation

After going through a study of all the aberrations for our system, an image simulation helps us to understand the quality of image formed. This particular feature is also provided by Zemax in the 'Extended Scene Analysis' tab. It provides us with different inputs to be used for simulating the entire FOV of our detector plane and to study the image variations which happen as a result of the imaging optics. The Figure 4.16 shows it more clearly. In the variant 1 (top panel), the inner detector positions are having small distortions seen for the input source grid. The image simulation for variant 2 (bottom panel) shows that the full input source grid is simulated at the image plane, with slight distortion at the edge of the detector.

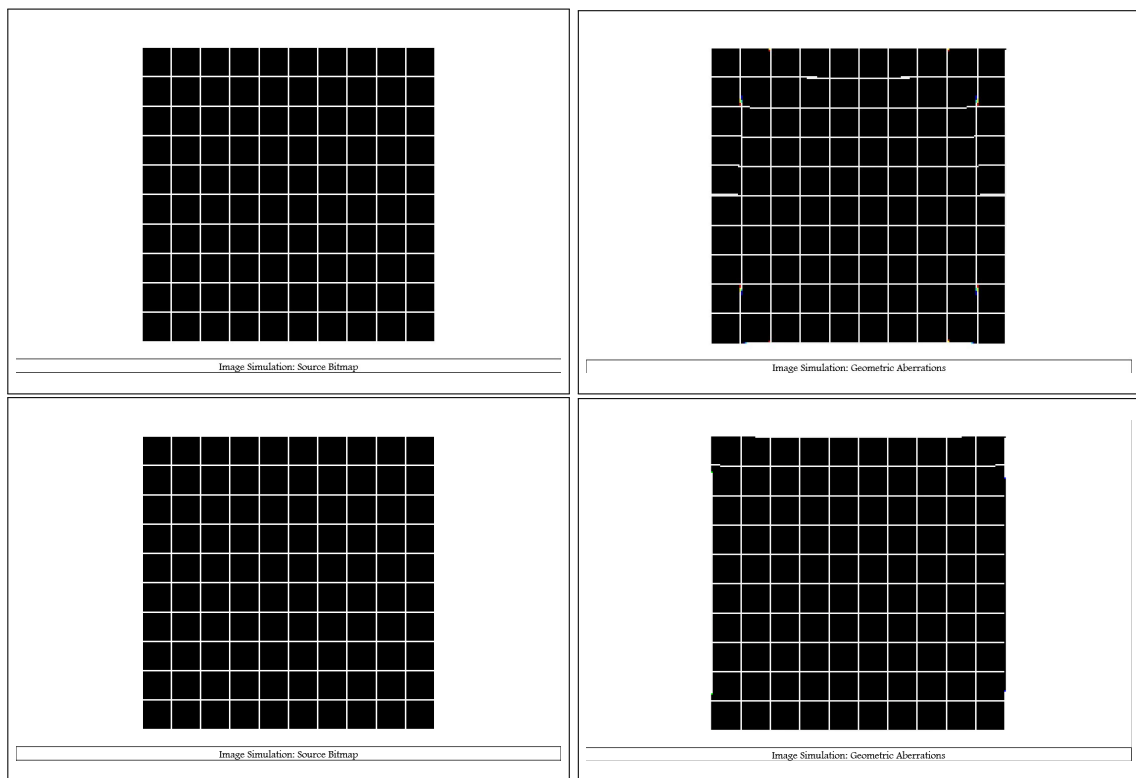


Figure 4.16: Image simulation tool of Zemax, showing the source (left) & final image (right) from the NISP optics for the two variants 1 & 2, top and bottom panels, respectively.

4.6 Limiting magnitudes from NISP

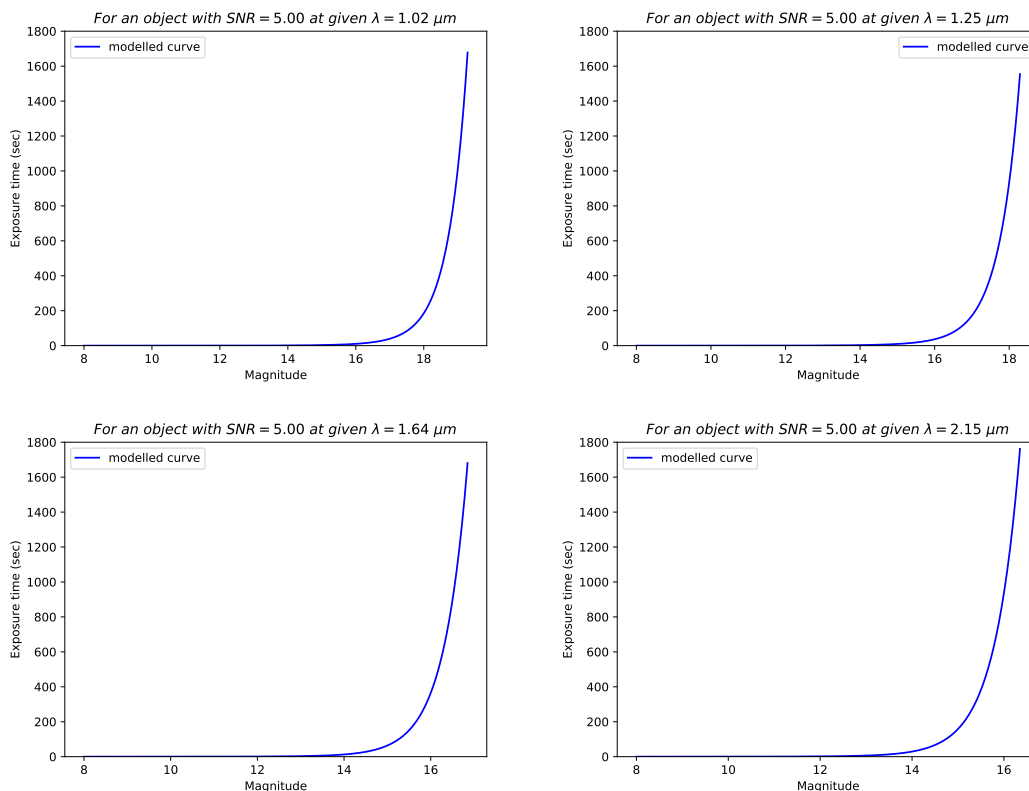


Figure 4.17: Magnitude vs Exposure time plot for SNR =5 at the central wavelength for each filter band in NISP.

In Figure 4.17, the magnitudes reachable with specific exposure times for an SNR of 5 are shown. These take into account the transmission through the different optical elements of NISP for the 2.5 m telescope with a final focal ratio of F/5 with an H2RG detector with 1" seeing. We see that magnitudes of 19.32, 18.38, 16.9 & 16.36 in the Y, J, H, K_s bands respectively, are reachable in half an hour exposure for a SNR = 5 (corresponding to errors in the range of 1.0 to 0.1 mag).

4.6.1 AR coatings

AR coatings are, indeed, very desirable in such an instrument to achieve the best throughput possible. Vendors, "Thorlabs", "Eksma Optics" etc have been contacted for

a quotation on AR coatings in the wavelength range of 0.9 - 2.5 μm . Finally we received a positive response from Eksma optics, about the availability of coating material : Ta (Tantalum) which will do the job using ion beam sputtering (IBS) technique. The other information provided by them are :

- Average reflectivity: < 2% @ 800-2500 nm
- LIDT: > 3 J/cm^2 , 10 ns , 10 Hz @ 1850 nm
- AOI = 0

They have also confirmed that the resulting coatings would withstand our operating conditions of cryo temperature and pressure.

4.7 Thermal Analysis

Thermal analysis is required to test the performance of the elements and the entire optics at room temperature (required at the time of assembly). The design has been made at 77 K & 10^{-6} mbar pressure. All the analysis and performance of the design are shown at this environment setting. With thermal variations, the major parameters which are controlled are:

1. The expansion in the thicknesses & semi diameters of the lens elements depending upon their *thermal coefficient of expansion (CTE)*.
2. Changes in refractive indices, which eventually lead to focus shifts.
3. Thermal expansion due to the CTE of the housing material of dewar e.g. aluminium has $\alpha = 23.6 \times 10^{-6} / ^\circ C$.

All these factors play a major role while understanding the result one should get while the assembly of the optics is done at room temperature. To check the way the various elements of the optics might respond to thermal environment, we used the "Make Thermal" tool available in Zemax. The minimum temperature was set to $-196^\circ C$ and maximum to $30^\circ C$. The deviations as seen with the above settings are :

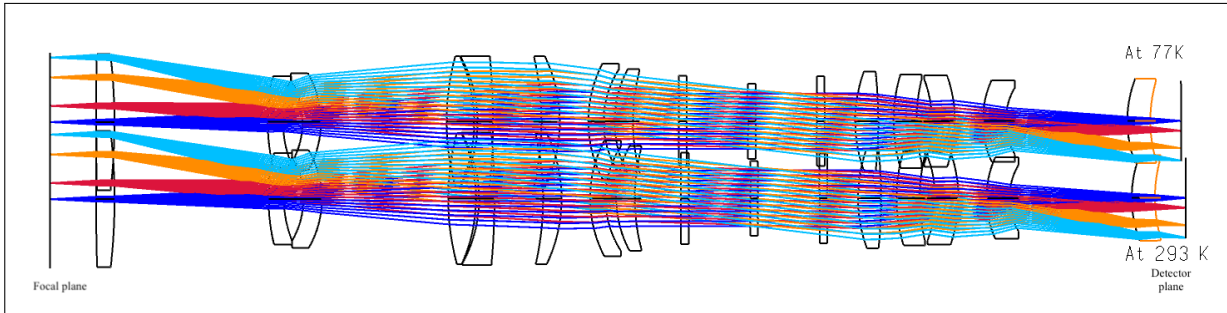


Figure 4.18: Optical layout for NISP for different thermal configurations.

- The expansion in the total length is ~ 3 mm. The lenses are separated from one another by aluminium rings.
- The WFNO changes from 4.89 (@ 77K) to 4.93 (@ 293° K or 20° C) subsequently.
- The spot diagram also shows changes in the spot sizes. The spot sizes are typically of $\sim 98 \mu\text{m}$ size for the various fields at room temperature.

The layout shown in Fig. 4.18 shows the difference in layout at the two different temperatures as labeled in the figure.

4.8 Tolerancing

Tolerancing of an optical design is crucial to link the ideal design to real performance specifications. Tolerances are specified for the parameters in the design, which may vary from the system prescriptions. It involves all the mechanical tolerances, lens tolerances, material property deviations etc to fit into a realisable fabrication by the manufacturer. The analysis further showcases the elements which need tighter tolerances, and others which can be loosened, as they don't contribute much in modifying the system performance. Zemax offers different analysis options for tolerancing, for example, sensitivity, inverse sensitivity and inverse increment mode. Monte Carlo simulation is also present for further analysis check post the basic run.

In the *sensitivity analysis*, we specify the tolerances for the parameters which might vary, and chose a criteria (RMS spot size, RMS wavefront, merit function etc.) which needs to be checked while running this analysis with the mentioned perturbations. Once the

analysis is run, zemax will estimate and record the amount of change in the criteria due to each of the tolerances mentioned individually.

After the sensitivity analysis, a *Monte Carlo* simulation is performed to estimate the changes brought in the criteria due to the perturbations simultaneously. Unlike, the sensitivity analysis, which shows worst offenders in the system, the Monte Carlo simulation gives a real-world performance for the system which meets the specified tolerances. *Compensators* are also realised for final focus adjustments, which is important to be specified in tolerance analysis.

Theoretically (Schwertz & Burge, 2012):

Lets define a criteria as Φ , and the tolerances as x_1, x_2, x_3 etc, the analysis will check sensitivity as,

$$\frac{\delta\Phi}{\delta x_i} \approx \frac{\Delta\Phi}{\Delta x_i} = \frac{\text{Change in criteria}}{\text{change in parameter}}$$

Hence, the contribution from each tolerance on criteria is,

$$\Delta\Phi_i = \frac{\delta\Phi}{\delta x_i} * \Delta x_i$$

Finally, based upon root-sum-square (RSS) differences method, the total contribution is estimated on the criteria due to the individual contributions of each tolerances,

$$\Phi = \sqrt{\Phi_0^2 + \left(\frac{\partial\Phi}{\partial x_1} \cdot \Delta x_1\right)^2 + \left(\frac{\partial\Phi}{\partial x_2} \cdot \Delta x_2\right)^2 + \dots}$$

For NISP, we have carried out one level of tolerancing performing "sensitivity analysis" with the criteria as "RMS spot size", and specified the tolerances on parameters for each of the surfaces whose details are mentioned below :

- Lens spacing = $50 \mu m$
- Lens thickness = $25 - 50 \mu m$
- Radius of curvature = $25 \mu m$
- Flatness = $\lambda/4$
- Index of refraction = 0.0002
- Wedge/tilt/decenter = $50 \mu m$

We checked 100 worst offenders list to pick the parameters which are sensitive and need to be tightened in order to ensure the required system performance. The tolerance analysis for NISP is going on iteratively to adjust to requirements, manage cost, with discussion with mechanical engineer, fabricators etc. The mechanical considerations have been incorporated in the tolerancing analysis with discussion with the mechanical engineer in the team. Important points which are considered from assembly viewpoint :

1. The edge separation shouldnt be very small, as it is hard to achieve. The value should be ~ 1 mm or more. This can be achieved with a spacer ring or other mechanisms.
2. The lenses should have actual diameter greater than the clear aperture with a value at least 6 mm, to enable ease of mounting.
3. The edge thickness needs to be ~ 5 mm.
4. Other important considerations are appropriate baffles to prevent stray light from off-axis beams, reflections from support structures which hit the primary mirror.

4.9 Stray light analysis

Stray light is the unwanted light in an optical system. It can occur due to scattering, straight paths from out of FOV areas and ghosting (out-of-focus images of bright objects due to reflection off lens). In zemax, the stray light analysis requires us to convert the design to "non-sequential" mode. It includes all multiple features of analysing the

layout with ray trace, and look in the detector viewer to see the light which reaches our detector. Later, the filter strings are applied to only check for the contribution of stray light hitting our system. Stray light analysis for NISP is on-going to check and eliminate the effects of unwanted light, which are incident on the system, using baffles.

4.10 Summary

The chapter deals with imaging optics design of NISP. The collimator with two camera variants are discussed with their comparative analysis of the design achievements. The imaging optical design has started with a set of goals to be attained, and the optimization process of the various optical elements, has led to the realization of the set targets. The imaging design of NISP comprises of a combination of F/8 collimator & F/5 camera to achieve a full FOV of $10' \times 10'$ in all the 4 near-IR wavelength bands. Two of the imaging design variants have been discussed in the chapter. We find that the variant 2 has merit in terms of better performance for most of the analysis tools. The major difference is seen in the MTF plot for the variant 2, where the system achieves a good contrast for all the field angles as compared to the variant 1 design, as well as a better peak to valley performance. Hence, the variant 2 shall be considered for further implementation of the spectroscopic & polarimetric techniques in the NISP imaging design. Further analysis needed for meeting real performance specifications have been carried out. These included, thermal analysis, tolerancing, stray light analysis.

Chapter 5

Spectroscopic Optics

“A spectrum is worth a thousand images”

The technique of spectroscopy is inevitable in any general purpose astronomical instrument. In order to get continuum and line emission flux caused by transitions in sources of interest almost all big telescopes have spectrographs of different resolving powers using various dispersing elements. Low resolution spectroscopy is considered important for faint sources on small telescopes, so as to get good SNR for the object. High resolution spectroscopy on medium or big telescopes provides us with the opportunity to study vibrational and rotational features of the spectra, apart from the electronic transitions seen in molecules. Hence, they help in inferring more detail into those modes. These features are seen as a blend in the low resolution spectra. Gratings & prisms have been used extensively in the past to record spectra in the low /intermediate resolving powers. With advancement of technology & requirement, echelle gratings were designed to provide highly resolved spectra with $R \sim 60,000 - 1,00,000$. Integral field units (IFUs) are being used for multi-object spectroscopy. Recently many instruments are designed as multi-mode, placing optical components in filter wheels within the path of optical chain, to switch from one mode to other. This arrangement requires a

need for a dispersion element which can be designed to produce undeviated diffracted light at the central wavelength of the band, with dispersion covering the detector plane for the entire range. Grisms have been designed for this purpose, and their use has been advantageous to double up an imaging instrument to spectroscopy.

5.1 Calculations of Grism parameters

Grisms are also called as ‘Carpenter Prisms’, and they are a conjunction of transmission gratings & prisms. They combine the dispersive properties of both the elements, to give zero-angle diffracted beam for an optical system. Grisms are very versatile & best suited for IR instruments, in which the pupil location is best suited for placement of grism. In astronomical spectrometers, the major advantage of grisms over transmission gratings is their ability to produce dispersive beam while sending the ‘blaze wavelength’ forward in its original undeviated path. Blaze wavelength decides the diffraction order in which maximum power for the grism is concentrated. The system is optimized for it by shaping the grooves, and application of coatings. This leads to easiest conversion of an imaging system to a spectrograph, which is mechanically simple and compact. The infrared imager design mostly re-images the image of telescope pupil on a cold stop to minimise the effect of thermal radiation on the detector. By placing a filter wheel containing the grism at the location of pupil stop, collimated beam shall be incident on the element, making the system ideal for spectroscopy. Such schemes are good for moderate resolution spectroscopy ($100 < R < 10000$) [Mar et al. (2009)].

The equations in Deen et al. (2017) are presented in order to calculate different parameters while incorporating a grism in the optical design. The main basic parameters to be controlled are apex angle of the prism (δ), slit width (Δx), groove spacing (σ) & blaze angle (ζ). Starting with the first principles, the equations here will illustrate the step by step process for calculations of relevant angles and other parameters for grism. Considering a grism with apex angle (δ), refractive index for the prism material (n), incidence angle at the flat surface (α), groove spacing (σ) & exit angle (β), the generalized grism

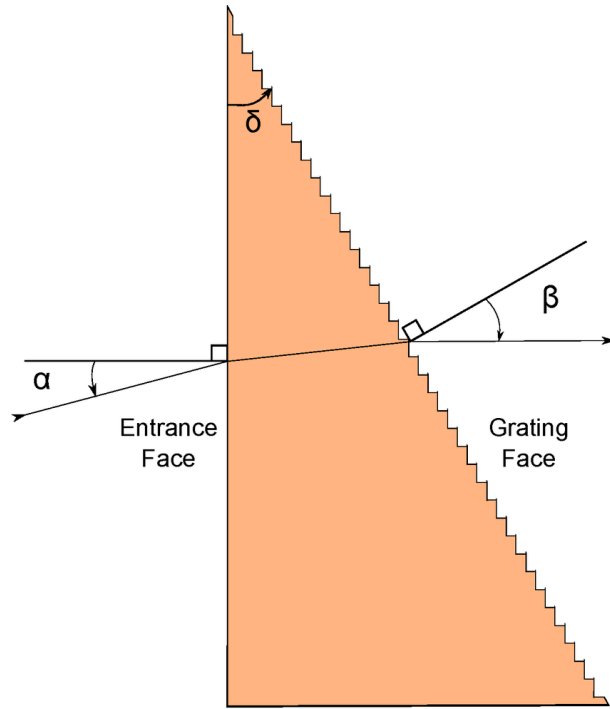


Figure 5.1: Schematic for grism design. Credit : [Deen et al. \(2017\)](#)

equation is presented solving the grating equation for β ,

$$\frac{m\lambda}{\sigma} = n(\lambda) \sin \left(\delta - \sin^{-1} \left(\frac{\sin(\alpha)}{n(\lambda)} \right) \right) - \sin \beta \quad (5.1)$$

These calculations also put a concern that the desired range of β should be within the field of view of the detector. There is a very simple relationship between the angles of the grism for an undeviated beam.

$$\beta = \delta - \alpha$$

Assuming the incidence angle for zero incidence, $\alpha = 0$, the groove spacing is calculated for the grism of any order “m” and orientation, to let the wavelength λ_0 pass undeviated.

$$\sigma = \frac{m\lambda_0}{(n-1) \sin \delta} \quad (5.2)$$

Resolution is of major concern in the spectroscopy instrument, as it is one of the main deciding factors in its practical usefulness for different scientific problems. As any

generic spectrometer will consist of the slit placed at the focal plane of the telescope, and then a grism at the cold stop location, the resolution is a convolution of the diffraction due to both these elements. The diffraction limited spectral resolution for a grism is defined as,

$$R_{\text{diff}} = \frac{\lambda}{\Delta\lambda} = (n-1) \frac{W}{\lambda} \tan \delta \quad (5.3)$$

where, n is the refractive index of the material of grism,
 W is the pupil/collimated beam width,
 δ is the apex angle of the prism.

The two main parameters to contribute in the resolution are,

1. Δx , slit width which determines the sampling in the spectral direction & the angular width of the slit on the sky. In the below equation, f_1 & f_2 are the focal length of the collimator and camera systems respectively. Δx_{pix} is the pixel size in the focal plane array.

$$n_{\text{slit}} = \left(\frac{f_1}{f_2} \right) \left(\frac{\Delta x_{\text{slit}}}{\Delta x_{\text{pix}}} \right) \quad (5.4)$$

2. δ , apex angle of the prism, determines the total wavelength coverage across the detector. N denotes the number of unvignetted pixels across the field.

$$\Delta\lambda_{\text{tot}} = \lambda \frac{N}{f_2} \left[\frac{\Delta x_{\text{pix}}}{(n-1) \tan \delta} \right] \quad (5.5)$$

The combination of the slit width and the apex angle of the prism determines, the resolving power of the grism.

$$R = R_{\text{diff}} \frac{f_1 \lambda}{W \Delta x_{\text{slit}}} = (n-1) \tan \delta \frac{f_1}{\Delta x_{\text{slit}}} \quad (5.6)$$

The resolution at a given slit width is given as (Mondal et al., 2009),

$$R = \frac{d}{D \tan \phi} \quad (5.7)$$

where, d is the diameter of the collimated beam, D is the telescope aperture & ϕ is the seeing. Using the equation, for a fixed resolution at a given seeing value, the collimated beam diameter increases with increase in the aperture of the telescope. The optimal seeing conditions are the governing factors for the slit width. The values are chosen to be smaller and larger than the median seeing of the place. The angular dispersion for a grating is defined as, $A = m/\sigma \cos \delta$, which is the amount of change of the diffraction angle with the change in wavelength. It gives the measure of angular separation between beams of adjacent wavelengths.

A very important aspect to be kept in mind while designing a grism and its mechanical mounting, is the dependency of the output spectra on the grism orientation. This leads to constraints on the repeatability of positioning of the grism wheel.

1. Tilt in the grism is introduced to avoid ghost images. It is seen from the grating equation (5.1) in Deen et al. (2017) that a tilt of $\alpha = 1^\circ$ in the incidence angle of grism, causes a deviation of 0.001° for the beam from the grism.
2. As per the calculations presented in Deen et al. (2017), a small angular displacement of 0.001° will lead to a linear displacement of $1.75\mu m$ within the detector.

Considering the size of one pixel $\sim 18\mu m$, this linear shift is very small. Hence, any moderately engineered grism wheel will also be able to produce repeatable spectral format. This clearly shows an insensitivity of the grism orientation with respect to an incoming collimated beam.

5.1.1 Choice of Order

Orders of diffraction are the different diffracted angles in which the power of the incident beam is distributed. The $m = 0$ order is direct transmission from the grating

in which we do not see the presence of a diffraction pattern (see Figure 5.2). The higher orders are more resolved, but include overlap from adjacent orders. As has been mentioned in Deen et al. (2017), the resolving power slit-width product is independent of the order of grism. The angular dispersion is also independent of the order, once the $\tan\delta$ & λ_0 are fixed, as σ includes them. It is advisable to choose first order for grisms in any instrument. The IR instruments present an added advantage of the grisms being used in the first order : it allows us to use the wavelengths at peak of blaze function and hence, the light of the higher orders could be easily blocked (Deen et al., 2017). On the other hand, $m > 1$ offers advantage to decrease the polarization effects. Hence, one can think of it as a trade-off between large spectral range & polarization independent performance.

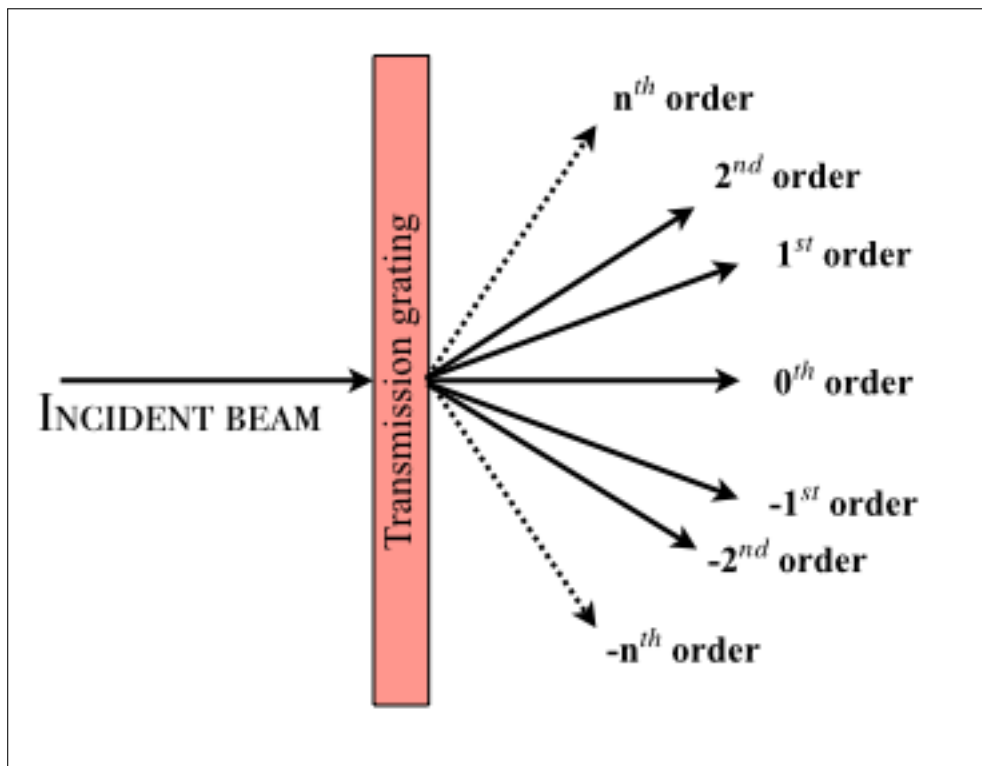


Figure 5.2: A schematic representation of the different orders from a transmission grating surface.

5.1.2 Blaze function & efficiency

The dispersion from a grism distributes the incident energy of the beam into different orders, which are seen at different angles. The amount of energy which gets transferred to a particular order, defines the efficiency of the grism in that specific order as a function of wavelength. The process of blazing introduces a modification in the grating groove geometry and helps to maximize the diffracted energy in one particular order for a wavelength. In the case of grism, this blaze wavelength will go undeviated from the grism and have peak efficiency. As is mentioned in the "Diffraction grating handbook" by Richardson Gratings (now Newport), there are different groove profiles, i.e. triangular, sinusoidal etc. They conclude that a particular groove profile isn't necessary to aim for blaze function within the different types of gratings. Usually the holographic gratings are available with sinusoidal grooves, and the ruled gratings have triangular grooves, but the blaze characteristics of both seem to be satisfactory. Hence, blazing only refers to concentration of diffracted energy and is independent of the groove profile or the fabrication mechanism for the same.

The efficiency of the grating depends upon several parameters: incident light power, polarization (s & p), angle of incidence (α), angle of diffraction (β), refractive index of the material at the grating surface, groove spacing and groove profile. The grating equation can be expressed to show the blaze condition,

$$m\lambda = 2d \sin \theta_B \quad (5.8)$$

θ_B is called the blaze angle for the grating, i.e. between the groove face and the plane of grating. According to [Mar et al. \(2009\)](#), for a beam to be undeviated from grism, the condition is $\beta = \delta - \alpha$. The blaze wavelength condition occurs, when

$$\beta = \delta \quad (5.9)$$

which leads to the undeviated blazed light passing through the grism.

5.1.3 NISP grism specifications

The first step which was followed towards designing the grisms for NISP was calculating the resolution which can be achieved with the present pupil diameter for NISP. The standard formula for resolving power of a grating is,

$$R = \frac{\lambda}{d\lambda} \quad (5.10)$$

Considering the λ for H band central value as $1.635 \mu m$, the $d\lambda$ required for a $R \approx 2000$, with Nyquist sampling of 3 pixels, the resulting dispersion element is 2.72 \AA . With the resolution per pixel of 2.72 \AA , the total range covered in a $2K \times 2K$ array would be 5570 \AA . Given that we have four wavelength bands to be covered, this range will suffice for all the band pass.

With this elementary calculation, we started with calculating the prism angle & groove spacing for achieving this resolving power. The use of Equations 5.2, 5.3, 5.6, helped us achieve the required values for our grism in the Y, J, H & Ks bands. The resolving power $R \approx 2150$ was achieved in all the four wavebands and the beams were undeviated. The Y grism was given a tilt of $\sim 1.2^\circ$ at the entrance face, to bring the deviation in diffraction angle within the detector extent. Table 5.1 gives a full description of the calculations and the required parameters for the design of grism in Zemax. The refractive index as a function of wavelength used the Sellmeier equations, and were derived from the *refractiveindex.info* site¹.

5.2 Grism design & analysis

The calculated numbers from the Table 5.1 were input in Zemax within a sequence of surface definitions to make the design of grism. To provide a detail over the steps to be followed,

¹refractiveindex.info

Table 5.1: The required parameters for an $R = 2150$, KRS5 material grisms in the Y, J, H, K_s filters in the 1st order, with $F_{coll} = 339$ mm, and $\Delta_x = 0.097$ mm are tabulated.

Resolving Power	Refractive Index	Wavelength (μm)	Prism Angle ($^\circ$)	Groove spacing (μm)
2150	2.4434	1.02 (Y)	23.08	1.80
2150	2.4209	1.25 (J)	23.41	2.21
2150	2.4031	1.635 (H)	23.68	2.90
2150	2.3928	2.15 (K_s)	23.83	3.82

1. Define a standard rectangular aperture surface, with the material KRS5 (Thallium Bromiodide) chosen from a list of IR materials which can be used for grism from [Mar et al. \(2009\)](#). One issue with KRS-5 is the difficulty in preparing surface rulings. For the grism with KRS-5 material, we had contacted Richardson Gratings (now Newport) with our specifications and requirements of the instrument working at cryo temperature. The reason for choosing this material in the first place was its high refractive index to achieve a desired resolution for our instrument. Richardson Gratings response to build grism from ZnSe material (other alternative considered) was negative and so we consider KRS-5 material only as of now.
2. Next is to define a 'Tilted' surface, for the inclusion of prism. The tilted surface requires the input of parameter 'Y-tangent', which is the value of tangent (prism angle) calculated for the grism.
3. After this we need to place the grating resin on the tilted surface. Since this required a slant in the coordinate plane, we include a coordinate break surface at this point to apply the required tilt for the grating surface. In this we enter the 'Tilt about X' as the value of prism angle.
4. Within the coordinate break space, we enter the resin & diffracting grating surface sequentially. The resin surface is defined with a surface thickness of $9 \mu m$, and the same material as prism, i.e., KRS5. This is done to avoid Fresnel losses coming from index mis-match. The discontinuity in the surface is seen at the

interface of change in refractive index between surfaces, and it could be avoided by using anti-reflection coating in case of high index materials (Mar et al., 2009). The next surface is 'Diffraction grating', which required two inputs for its proper application. They being the *order m*, and *groove frequency*. These values are entered from our calculated inputs for a particular grism.

In this way, the grism design is completed and each of the grisms are placed in the optical chain at filter wheel 2 position. One of the grisms for the Y band, had an additional surface to define its entrance face. The entrance face of all the other grisms are right-angled. For the Y grism, we gave a slight tilt to it of 1.2° , to bring the spectrum within the detector FOV. The values of each of the parameters for each wavelength band was entered using the multi-configuration editor in zemax. The grism designed is shown in Figure 5.3

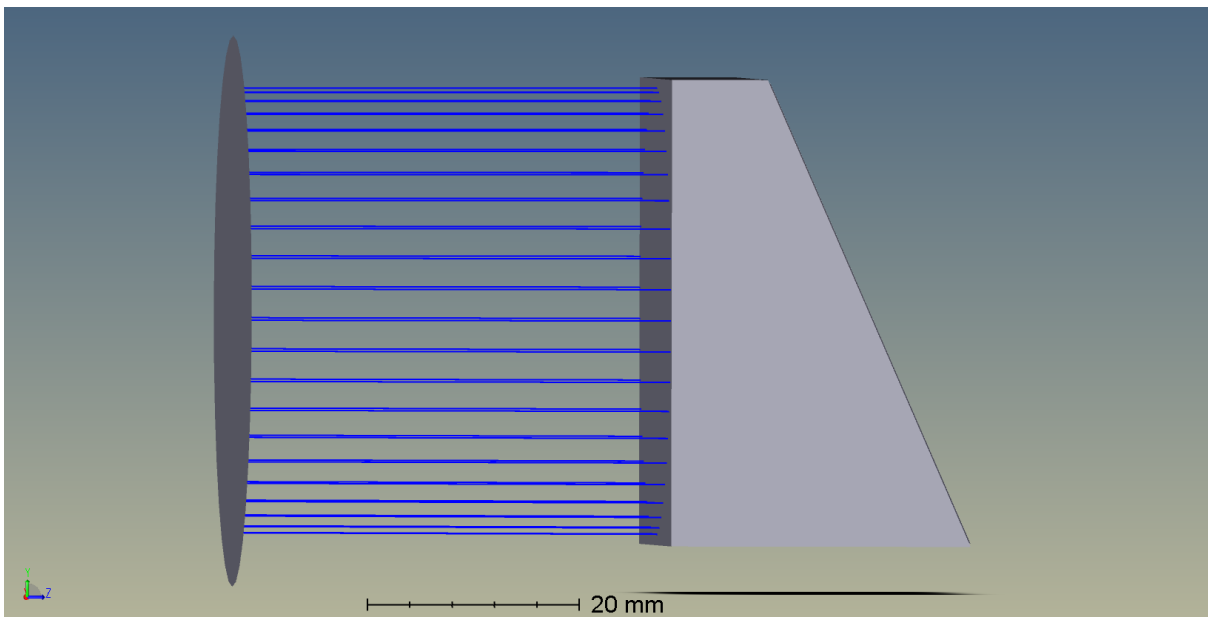


Figure 5.3: Grism design

5.2.1 Low resolution grism

A low resolution grism with resolving power $R \approx 560$, has also been designed. This grism gives the entire spectrum from $0.9 \mu\text{m} - 2.3 \mu\text{m}$ covering the full FOV of detector.

The grism is used in the 1st order for all the 4 wavelengths using ZnSe material. A layout for it is shown in Figure 5.4. The prism angle defined for this is 5.37° . The higher orders (for Y & J bands) will need to be separated from the spectrum using a cross-dispersor. The footprint diagram in Figure 5.5 is an overview of the coverage of

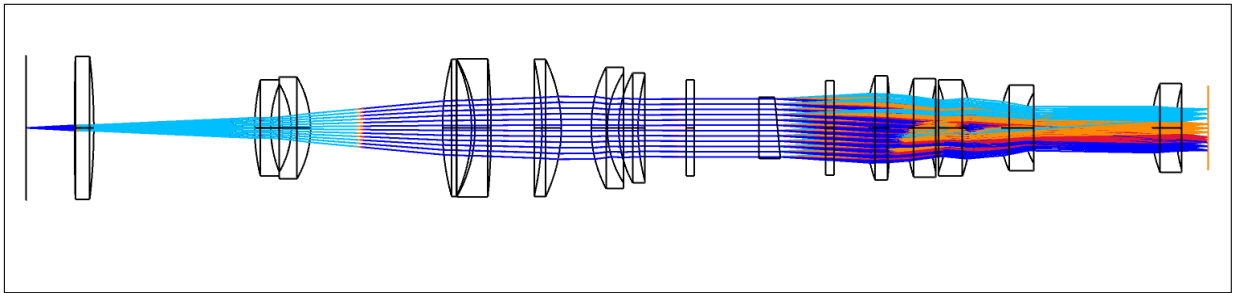


Figure 5.4: An optical design layout for a low resolution, $R \sim 560$ grism for NISP.

Y, J, H, K_s bands over the detector plane with the spots seen being comparable to the sizes \sim airy radius.

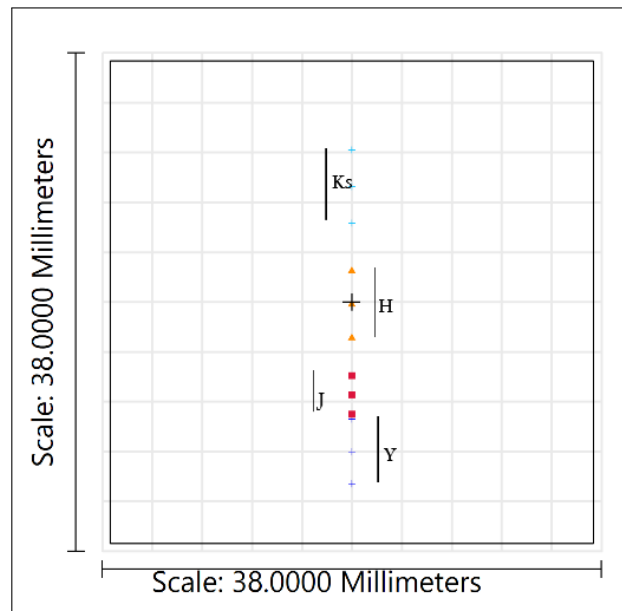


Figure 5.5: The footprint diagram shows the simultaneous coverage of different wavelength bands on the detector plane for the low resolution grism.

5.2.2 Intermediate resolution grism

The layout for the grisms in the filters Y, J, H, K_s are showcased in Figure 5.6. The Y grism has an added tilt of 1.2°. These grisms will be used in **conjunction** with the imaging filters in 1st filter wheel to confine only the respective wavelength range to pass through the grism. This will also avoid the presence of higher orders of other wavelengths to contaminate the spectrum.

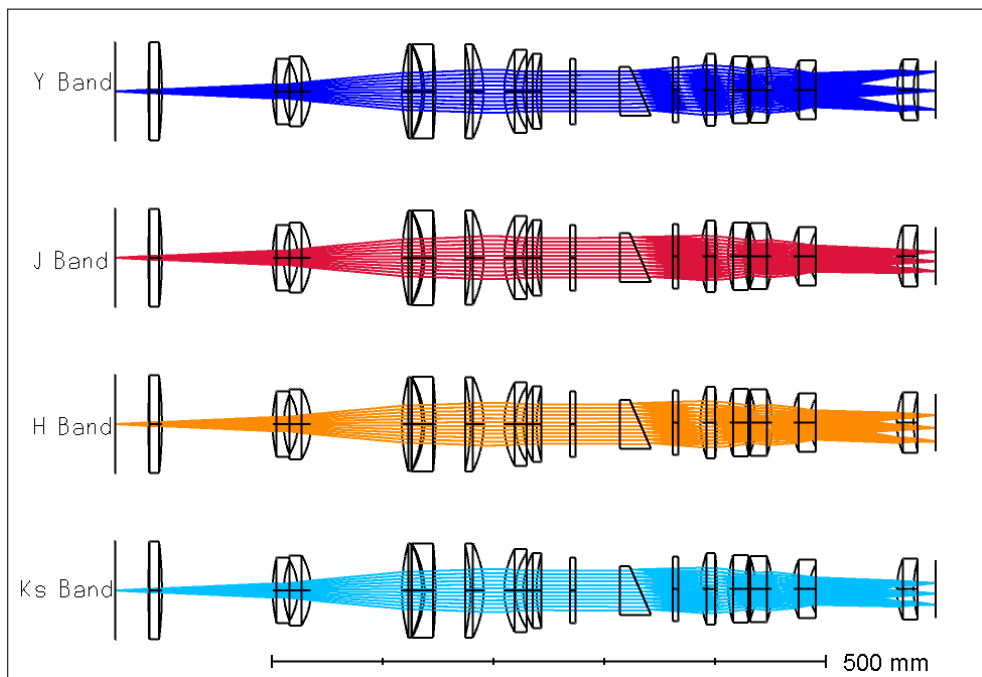


Figure 5.6: Layout of the Y, J, H, K_s grisms for NISP with $R \sim 2150$ for $m = 1$ using KRS 5 material.

5.2.3 Spot diagram

The spot diagram for spectroscopic analysis is important in the sense that it tells how clean and focused spectrum is seen for a point source at specific wavelengths. The size of the point source should get properly transferred over to the detector plane as a spectrum when considering all wavelengths. The spot size for H band at its central wavelength is shown in Figure 5.7. The size of the spot being close to Airy radius is a

good determinant. From the matrix spot diagram we can see the detector coverage for

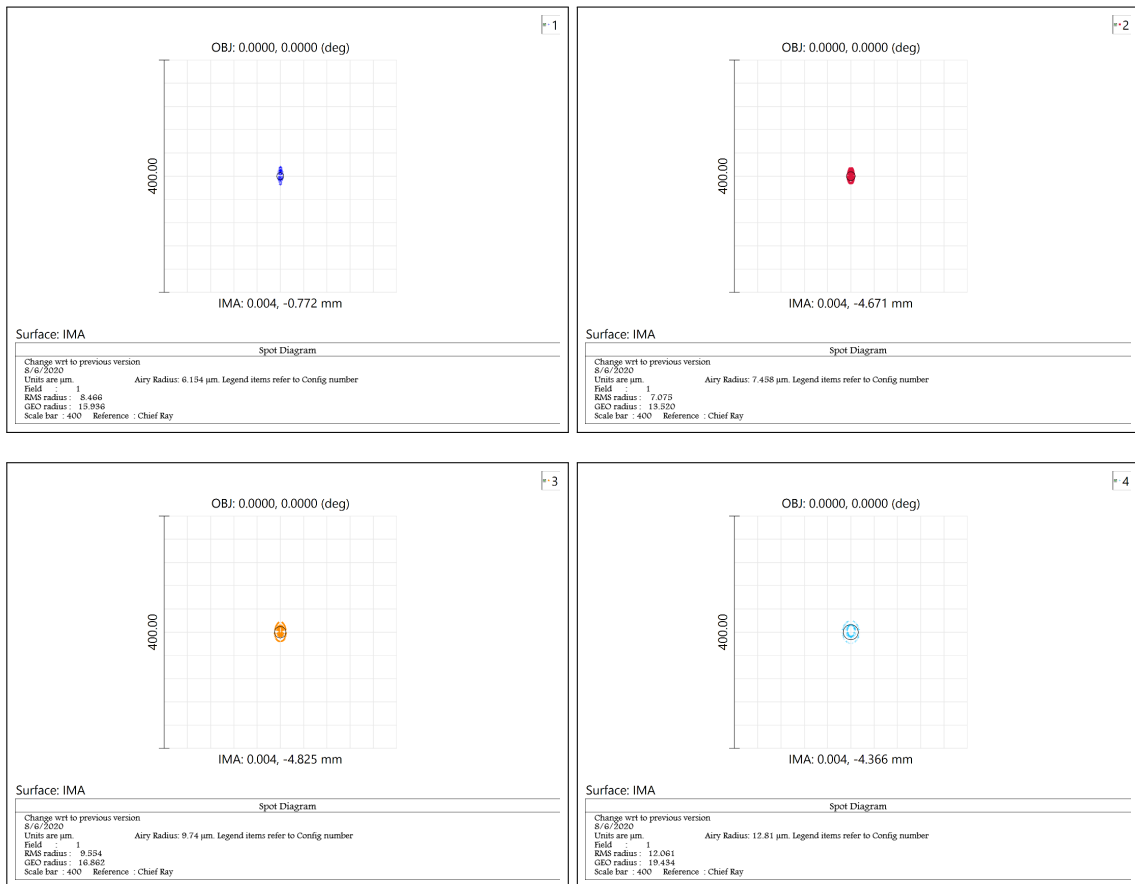


Figure 5.7: Spot diagram for on-axis field for the Y (top left), J (top right), H (bottom left), K_s (bottom right) filters.

the different wavelength bands marked as different configurations. Its interesting to see that the full single mode spectrum for each individual waveband could be achieved using these gratings without any vignetting in the system.

5.2.4 Diffraction encircled energy

The diffraction encircled energy plot is a very good tool to be considered in an optical design. As can be seen from the Figure 5.9, the encircled energy plots are approaching towards the diffraction performance for each individual wave band. The sampling size chosen in *Zemax* is 512 x 512. It is done to sample the pupil using a ray grid, with larger the number, higher the accuracy.

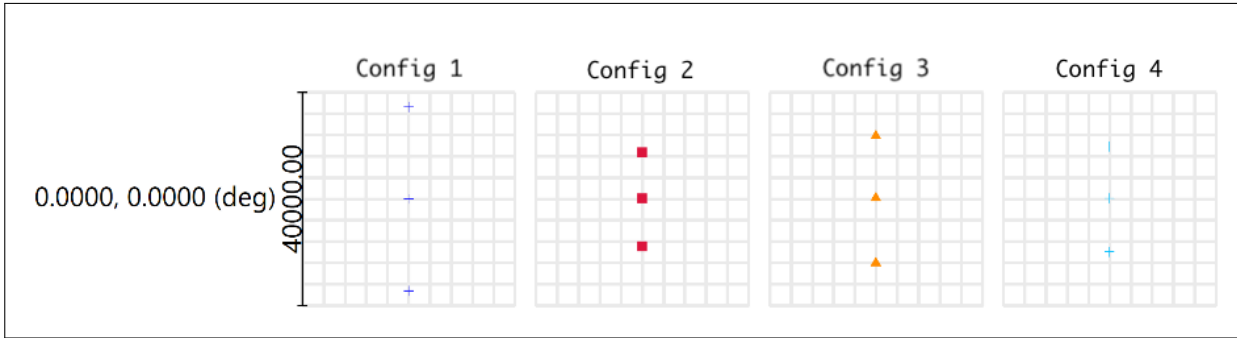


Figure 5.8: Matrix spot diagram for the Y, J, H, K_s grisms of NISP defined as different configurations in Zemax.

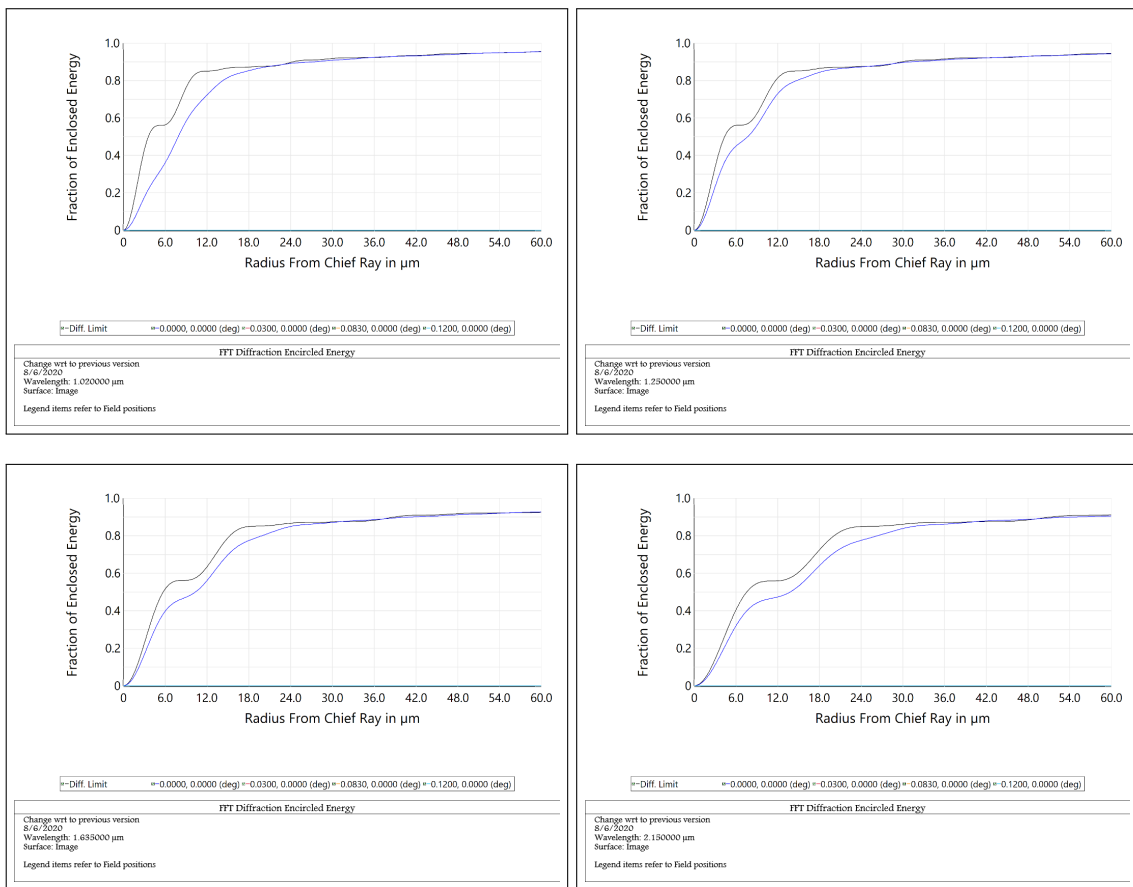


Figure 5.9: Diffraction encircled energy for the Y, J, H, K_s grisms at their central wavelength.

5.3 Summary

The chapter discusses the spectroscopic optics for the NISP instrument. An illustration of the grism design for spectroscopy is presented & the calculations performed for its

implementation are discussed. The spectroscopic mode for NISP provides an intermediate resolving power, $R \sim 2150$ at all the 4 near-IR wavelength bands. Another grism designed for low-resolution, $R \sim 560$ is discussed.

Chapter 6

Polarisation Optics

“To many astrophysicists, Stellar polarimetry is a Cinderella subject considered as being so insignificant and, at the same time, being so esoteric as to be ignored and left alone.”

- Stellar polarimetry ([Clarke, 2010](#))

Above mentioned quote is very relevant when it comes to utilisation of one of the very important tool at the disposal of astronomers: polarimetry. The technique of polarimetry provides deeper insight into several exciting processes like dust alignment mechanism, estimation of galactic magnetic field strength, which are not otherwise addressed by other techniques. It, thus, helps us understand these sources of interest. The previous chapters of the thesis have dealt with *imaging & spectroscopy* techniques, widely used to gain knowledge of astrophysical sources. In this chapter, some details about the design of polarization optics to be incorporated in NISP are given.

6.1 Algebra of Polarisation

Polarization is a fundamental property of light. It can be described as a vector quantity \mathbf{S} expressed as function of $[x,y]$ and the wavelength λ and time t (Snik & Keller, 2013). Light is an electromagnetic wave and the polarization of light is defined as, *the evolution of oscillation of E vector perpendicular to direction of propagation of light with time*. Unpolarized light, is the random orientations of the E vector with time as it propagates. There is a close relationship between the polarisation properties of random electromagnetic beam and its coherence properties as explained by Wolf (2003). The theory helped to elucidate changes in the state of polarization of light, as the beam propagates. By measuring polarization of an astronomical source, one can reveal the physical properties of the underlying medium which cannot be done measuring only the scalar properties. From the polarization of a star light, the physical properties of the dust i.e, size, shape, refractive index and the mechanism which caused the process to occur can be determined. polarization could occur due to scattering off micron sized dust particles having aspherical shapes, synchrotron process, or reflection (see Chapter 1).

6.2 Choice of polarization optics & trade-offs

The optical elements used in the instruments to serve the purpose of polarization measurements have different properties. There are several criteria which define the suitability of a particular element as per requirement. The size of optics and wavelength of work are critical factors to account for the feasibility of the device. Other major factors include the efficiency, transmittance, angular acceptance, internal scattering, extinction ratio, ghost images and interference effects. The available varieties of polarizers include birefringent materials i.e. Wollaston, Foster prisms, Glan-Thompson prisms; polaroids; wire-grid polarizers; wedged double Wollaston; mostly with a rotating modulator/retarder i.e. half-wave plate or quarter wave plate. The underlying working mechanism of a polarimetric instrument involves three components: a 100 % calibrator, a modulator (or polarizer) & a polarizer (as analyser). They are placed in the

optical path sequentially as the light from telescope arrives and is impinged on 100 % calibrator, and passes through the optics, the polariser elements and finally the detector. The 100% calibrator (Glan-Thompson prism or WGP) is removed from the optical path for regular observations. The function of the modulator is to rotate the axis of transmission, and the intensity as the function of phase is analysed by the polarizer which we measure from the image captured by detector. One of the parameters which defines the merit of a polariser is 'extinction ratio'. Extinction ratio is the ratio of transmitted intensities taken with the axes of two polarizers aligned and crossed. It is determined by measuring the transmission of the system once when the transmission axis and input polarization axis is parallel, giving maximum intensity; and other by placing them at 90° phase recording minimum intensity. Such instruments' efficiency depends on the extinction ratio of the polariser device chosen and on the number of optical components present in the optical path before it reaches the polarizer. Due to this reason, polariser optics is often preferred to be placed before any optics (reflecting, tilts) which can introduce a change in the initial state of polarization of light. The polarizers can be chiefly divided on the mechanisms of their working into 2 main types, described below :

6.2.1 Dichroic Polarizers

Dichroism is defined as selective absorption. If white light is passed through a dichroic crystal, then the resulting light possesses different colors according to the direction of travel of light with respect to the crystal axes. It reflects the anisotropy of the crystal material, and can be conclusively told as the material absorbing more light in one incident plane than the other. This makes the light become more polarized as it travels further through a dichroic crystal. The typical examples of polarizers based upon this mechanism are : polaroids (H- & K-types). A polarizing filter has a transparent or greenish appearance for the direction of vibration parallel to its principal axis (Clarke, 2010). Polaroids have large acceptance angle, which makes them useful for convergent beams i.e. as attachment just before the focal plane. Dichroic polarizers are considered to have the largest acceptance angle $> 20^\circ$.

Wire-grid polarizers, function in a way that the incoming EM wave incident on the grid, with the oscillations parallel to the grid is reflected and the oscillations which are perpendicular to it are transmitted through the mesh. This gives a polarized output by selectively absorbing one direction of oscillation of the incoming EM wave. The spacing between the wire mesh and width of the wires is the deciding feature in designing the polarizers for a specific wavelength. Both parameters should effectively be smaller than the wavelength of operation. This makes wire-grid as a right choice for infrared wavelength band.

Glass polarizers, refer to simple piece of glass which can also be used as an effective polarizer for light at non-normal incidence. The working principle involves Brewster angle θ_B , which tells that the reflected light will be fully polarised for the incidence angle at θ_B . At this incidence angle, the separation between the refracted and reflected beam is 90° , and the refracted beam will be only partially polarized. A Brewster window is only available polarizer in the UV wavelength band. Its extinction ratio depends on the angle of incidence for the incoming beams, and is of order $\sim 1000:1$.

6.2.2 Birefringent Polarizers

Birefringence is a property of crystalline materials which exhibits separate indices of refraction for the two directions within the crystal. An input incident light on such a crystal, produces two output beams which are orthogonal to each other. They are termed as ordinary (o-) ray and extraordinary (e-) ray. The difference in refractive index, called the birefringence ($= n_o - n_e$) for the crystal, produces a phase difference (effective path difference) between the o- & e- beams. One other form of birefringence is also present which involves total internal reflection (TIR) of one of the components at the interface of the crystal. For the previous case, three cases of polarizers can be listed, namely Rochon, Wollaston & Senarmont. They are made from two components cemented together. With little variations in the direction of the optic axes of the three polarizers, they differ in the separation angle achieved between the two orthogonal beams on exit from the prisms.

Rochon prism, is designed in a manner that the optic axis of the first prism is parallel to

the propagation direction, while the optic axis of the second prism is perpendicular to it. The emergent rays have o- ray undeviated, and the e- ray deviated by two interfaces; firstly from material-material and second from air-material exit face. The deviation is small of the order of 1° or 2° , which depends on the angle of prism and the refractive index of the material (Clarke, 2010). *Senarmont prism*, has the optic axis of the first prism parallel to the direction of propagation, and that of the second prism is perpendicular to the propagation direction and the base of the prism. *Wollaston prism*, is very widely used prism which also gives more separation angle between the o- ray and e- ray. The optic axis of both the prism in Wollaston is perpendicular to the direction of propagation and to each other. It causes a deviation of both the o- ray and e- ray from its original path. Thorlabs provides s with the separation angles between the output beams range from 1° to 20° . The extinction ratio is very high of the order of 10,000:1 for few materials like quartz, MgF_2 ; to 100,000:1 for calcite, YVO_4 . A full comparison based upon the extinction ratio for all the available polarizers is shown in the plot 6.1. Mentioning about the other types of birefringent polarizers, including TIR in the principle to transmit only one component of the emergent beam to be used for polarization estimation. Two of such polarizers readily used in instruments are Glan-Foucault & Foster prisms. Such polarizers offer more angular separation between the emerging beams. In a *Glan-Focault* prism, the incident beam is perpendicular to the entrance and exit faces. The optic axes is parallel to both the faces. An air gap is present between the two prisms, which causes TIR to occur at the interface. The prism in this setup has an acceptance angle of 7° and the angle of prism is $\sim 38.5^\circ$. The emergent beam is the e- ray.

Drawbacks -

1. The birefringence causes lateral chromatism in the images when employed in an instrument.
2. The transmitted intensity of the e-ray in case of Glan-Foucault prism is about half the incident one.

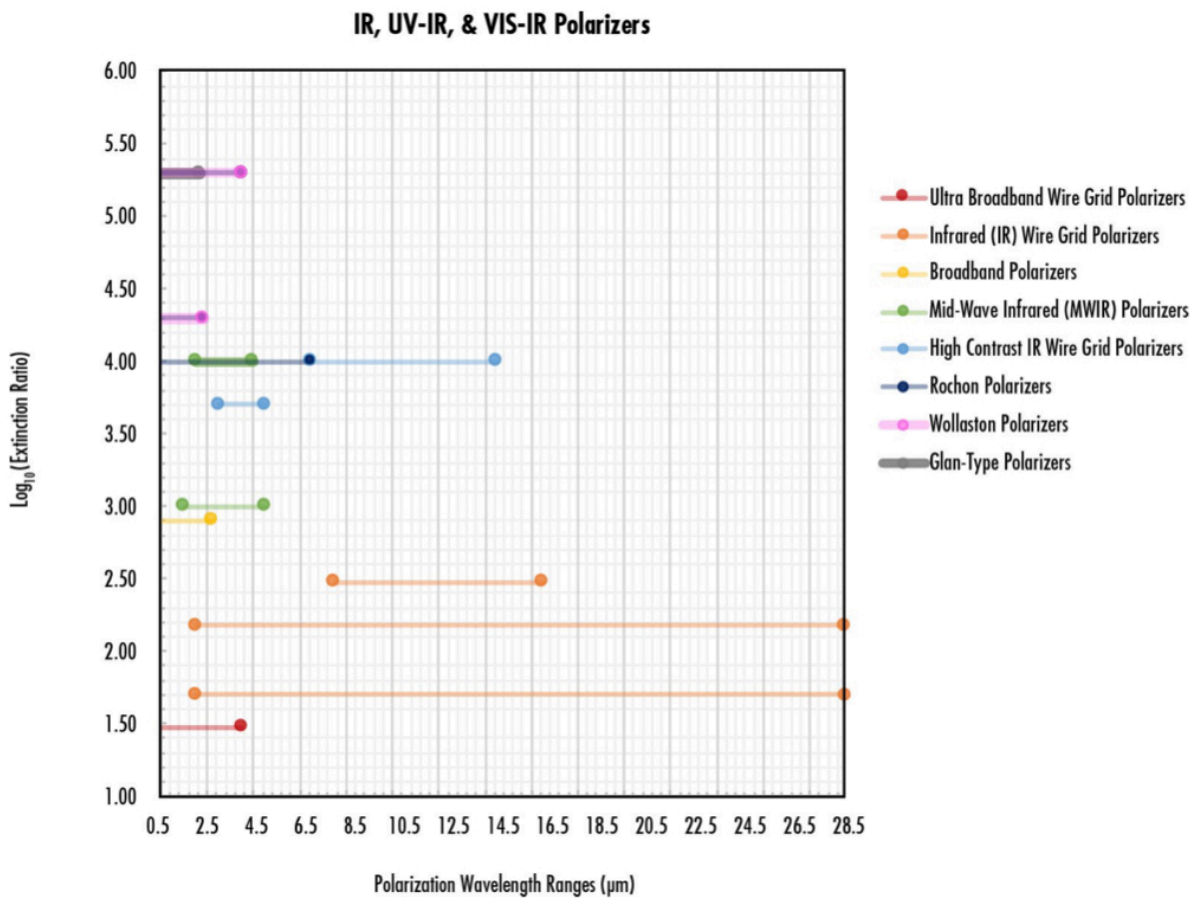


Figure 6.1: Comparison showing the extinction ratio for different types of polarizers available in the VIS-IR wavelength range. (From 'Edmund optics' <https://www.edmundoptics.com/knowledge-center/application-notes/optics/polarizer-selection-guide/>)

6.3 Wedged Double Wollaston (WeDoWo)

Wollaston prisms have the property of splitting the beam of light into e-ray and o-ray. Utilising the complete 100% flux of incident light, gives it an advantage over the other polarisers for the purpose. It is quite well known that the atmosphere plays a role in affecting the imaging of distant stars. The extinction which needs to be corrected in the case of photometry, only reduces the flux which reaches to a ground based observer. In the case of non simultaneous polarization measurements, these sky variations affect the measured values at the different position angles. The intensity scintillation overriding the photon shot noise may pose a problem in case of polarization measurements.

This particular problem could be avoided by employing a system which can record the images at different angles of the polariser simultaneously. A Wollaston prism with half wave plate can very well serve the purpose. But to get polarization values, we need intensity measurements at atleast 3 position angles. The more the number of angles, the more precise we would be able to infer the polarization values from our observations. But the variation in sky in the time gap of changing the modulation angle of the modulating retarder still doesn't nullify the presence of uncertainties in the measurements. To get rid of it, a component which uses two Wollastons in its design, with their optical axis at 45° offset can provide us with intensity at 4 modulation angles simultaneously. These can then be utilised using Stokes formalism to derive the result. This component is called a wedged double Wollaston (WeDoWo).

The significance and a general implementation of WeDoWo in multimode instruments has been discussed in detail by [Oliva \(1997\)](#). The advantage of not using a $\lambda/2$ retarder plate in the optical beam increases its worth by further avoiding the mechanical complexities in the design due to its inclusion. Subsequent to it, there have been several instruments including the major FOSC family instruments which have utilised the capabilities of WeDoWo by integrating it as part of instrument. Few examples being AFOSC ([Pernechele et al., 2003](#)), TFOSC ([Helhel et al., 2015](#)), ALFOSC ([Gorosabel et al., 2014](#)), FOCAS ([Kawabata et al., 2003](#)), FORS1 ([Patat & Romaniello, 2006](#)), HOWPOL ([Kawabata et al., 2010](#)), PAOLO ([Covino et al., 2014](#)).

6.3.1 Design of a WeDoWo

[Oliva \(1997\)](#) explains the implementation of a combination of 2 Wollastons with 2 wedges, resulting into an element capable of measuring intensity at 4 angles simultaneously.

The design sketch for the WeDoWo is shown in [Figure 6.2](#). The collimated beam from the pupil plane is deviated at an angle by the wedge for incidence on the Wollastons. The deviation of the beams by the wedges, ensures the prevention of vignetting in the system due to two Wollastons and hence full beam is used. Then each Wollaston divides it into the two orthogonal beams, giving us 4 beams from 2 Wollastons. In

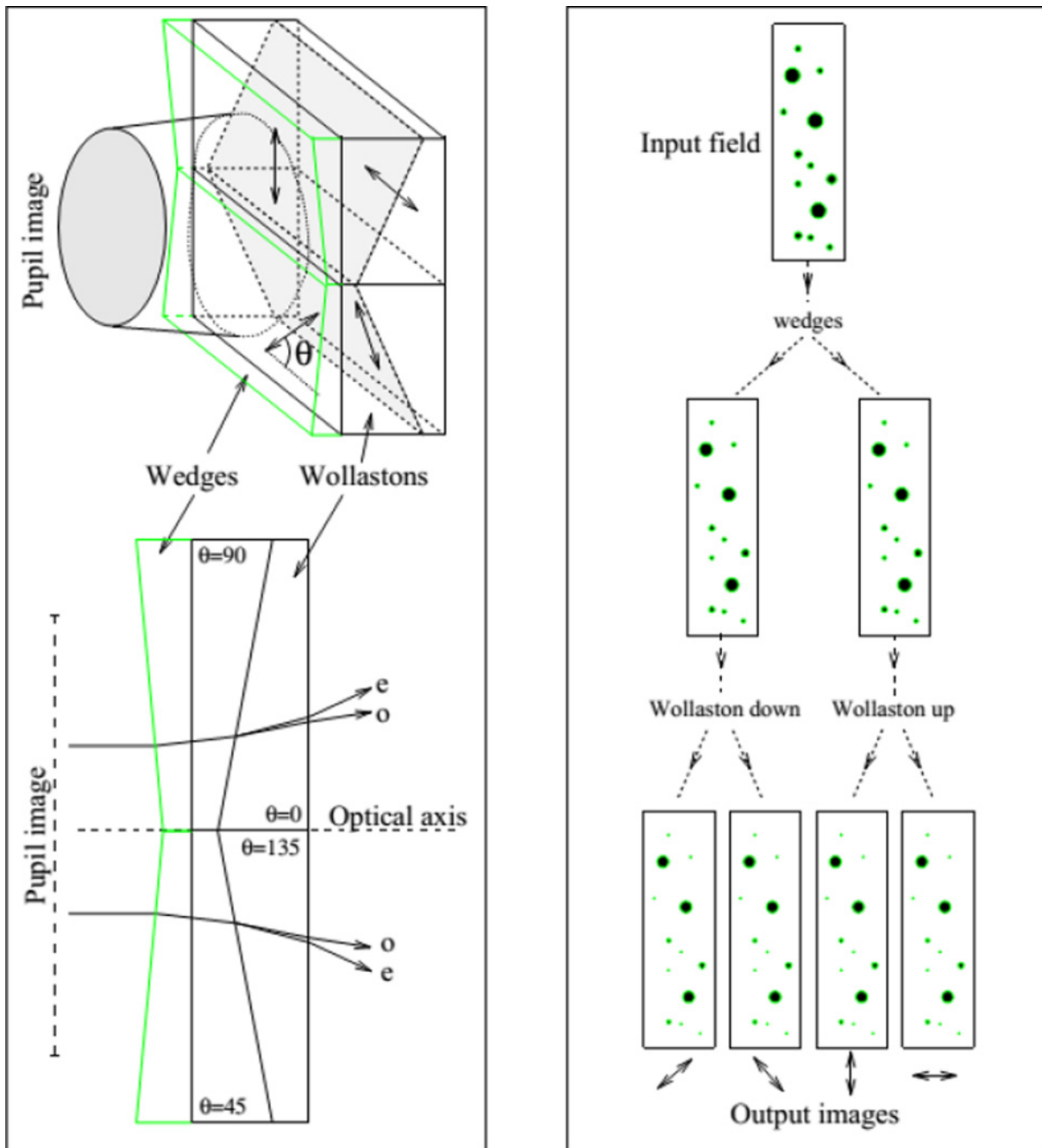


Figure 6.2: *Left:* The schematic design of WeDoWo showing the pupil plane beam being split into the components from up and down Wollastons. *Right:* Work concept of WeDoWo. The image is from [Oliva \(1997\)](#).

this design, the optical axis of both the Wollastons are at 45° to each other. The angles required for the proper implementation of the design are also determined from a small calculation based upon the width of projected sky required and other parameters. The

formula as presented by Oliva is applied with the presented outline in Figure 6.3,

$$\left(\frac{\theta}{\text{degrees}}\right) = 2.78 \left(\frac{\theta_{\text{sky}}}{100''}\right) \left(\frac{D_{\text{tel}}}{1\text{m}}\right) \left(\frac{D_p}{1\text{cm}}\right)^{-1} \quad (6.1)$$

where D_{tel} is the diameter of telescope & D_p is the pupil diameter. The required angles

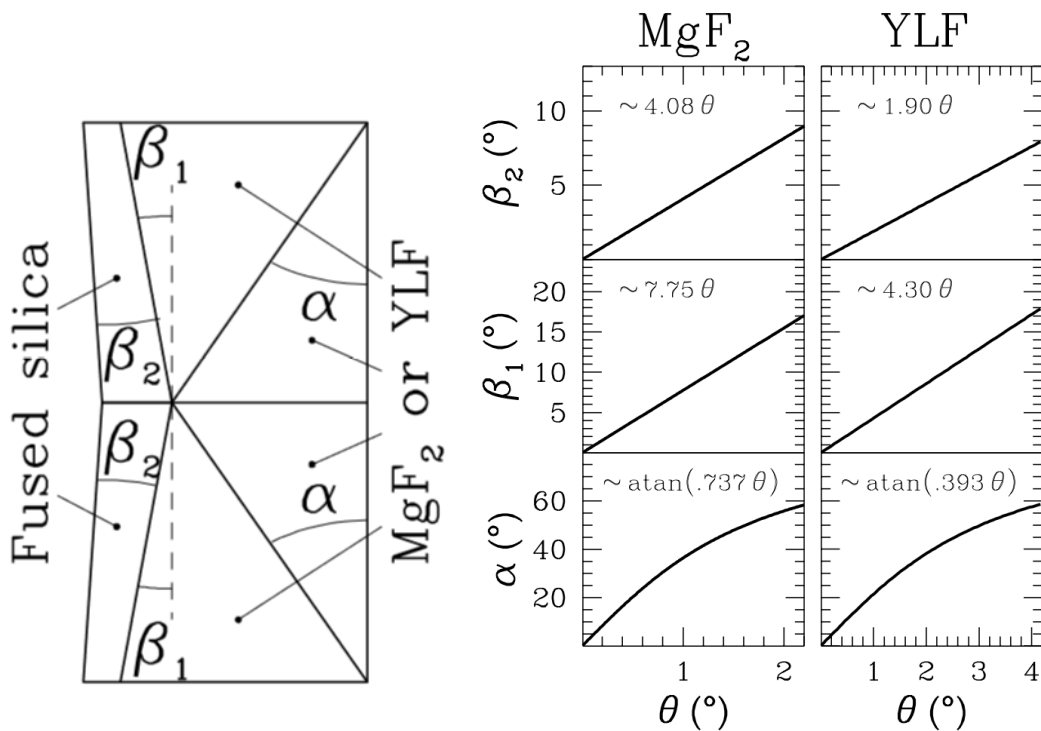


Figure 6.3: *Left* : A block diagram of the WeDoWo with different angles which comprise its design. *Right* : The dependance of the required angles on the θ factor is shown for optical (MgF₂) & infrared (YLF) materials. The image is part of (Oliva, 1997).

have been calculated to ensure 4 non-overlapping image strips for the 4 angles. A very important addition for the feasibility of image strips is a "focal plane mask". It has to be defined & placed in the aperture wheel at the Cassegrain focus. The focal plane mask will slice only the region of sky visible within its aperture and it will pass through the entire optical system.

6.3.2 Design of WeDoWo for NISP

The materials used in the design of wollastons are chosen based upon their birefringence property. A set of materials are used in the astronomical community, for eg., MgF_2 , YLF, calcite, $LiBNO_3$ etc. The major point of consideration is to maximize the separation between the two orthogonal components, so as to have non-overlapping fields. A drawback of this attempt is to cater with high lateral chromatism, with the increase in difference of refractive indices, which leads to large angle separation. Hence, the design has to later optimize to minimize the aberrations arising due to the specific requirements of it. Another major thing to ponder over is the availability of the material. A check with the companies ([Bernard Halle](#), [Karl Lambrecht](#)) involved in the fabrication of wollastons, brought us to the realisation that YLF is not available easily and it is really hard to find a large enough YLF crystal for our needs. So, the design has to be compromised and completed with MgF_2 material. Several infrared polarimetric instruments have used MgF_2 for this purpose; one example is ([Covino et al., 2014](#)).

Using YLF (Yttrium lithium fluoride, LiYF4) :

The design step for the polarimetric component for NISP included firstly the determination of θ as per our requirement. This is calculated from Equation 6.1 by plugging in our numbers. The fixed input parameters are:

$$D_{tel} = 2.5 \text{ m}$$

$$D_p = 38 \text{ mm}$$

The birefringence of the crystal & the Wollaston angle α cause the separation between the two orthogonal beams from each Wollaston. The value of θ_{sky} is defined in a way that the 4 image strips cover the maximum FOV of the detector without overlap between them, and with an optimum separation between the o- & e-ray. Keeping this in mind, we started the design of WeDoWo with $\theta_{sky} = 2.45'$ width with $0.05'$ separation between each strip, to finally $\theta_{sky} = 1.4'$ width, in order to avoid overlaps. This number was input in the Equation 6.1, and the θ obtained was $= 1.536^\circ$. From the dependance of the angles on the calculated value for θ for WeDoWo design using YLF material (see Figure 6.3 left panel), we estimate the three angles :

$$\alpha = \text{atan}(0.393\theta) = 31^\circ$$

$$\beta_1 = 4.30\theta = 6.6^\circ$$

$$\beta_2 = 1.90\theta = 2.9^\circ$$

With these already estimated numbers based upon our requirements, we designed the WeDoWo in zemax (refer to Fig. 6.4).

Using MgF_2 (Magnesium Fluoride) :

The value of θ is first step for the design of WeDoWo, and stays the same for our requirement. Referring to Fig. 6.3, the dependance of other design angles on θ varies from material to material, to maintain a proper separation between the beams from both orthogonal components. The calculated θ is 1.536° . The angle dependance for MgF_2 is as described :

$$\alpha = \text{atan}(0.737\theta) = 48.5^\circ$$

$$\beta_1 = 7.75\theta = 12^\circ$$

$$\beta_2 = 4.08\theta = 6^\circ$$

The WeDoWo has been designed using these parameters. As is evident from the calculated α angle which is large as compared to the case of YLF material, it will lead to an increase in the size of the wollaston (refer Fig. 6.4).

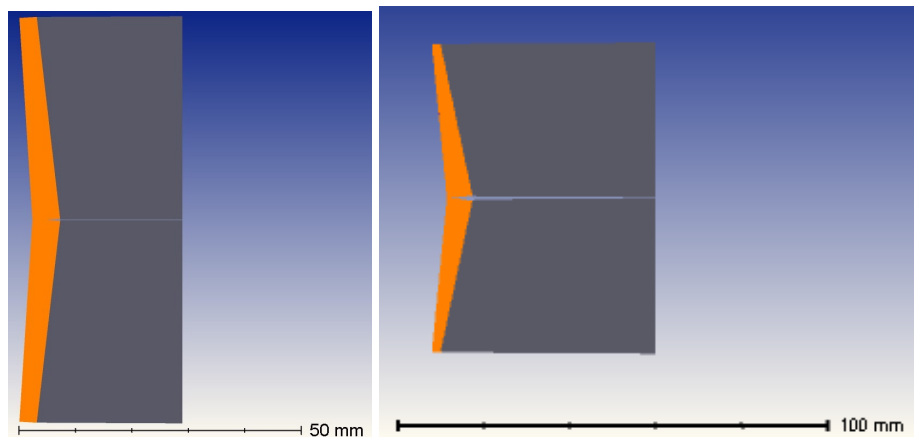


Figure 6.4: Shaded design of YLF (left) & MgF_2 (right) WeDoWo for NISP designed with angle definition as mentioned in section 6.3.2. The orange color is the wedge and dark grey color are the Wollaston.

6.3.2.1 Zemax design of WeDoWo

Table 6.1: The surface definition for the WeDoWo design in Zemax, with the parameter values for different surfaces.

Surface	Comment	Material	Mode	Decenter	Tilt
Coordinate Break	Element decenter			17.8	
Coordinate Break	Element tilt				-3.7
Standard		Fused Silica			
Coordinate Break	Element tilt : return				3.7
Coordinate Break	Element tilt				-6.6
Standard					
Coordinate Break	Element tilt : return				6.6
Coordinate Break	Element tilt				-6.6
Birefringent In	Up Wollaston	LiYF4	0	0	1
Coordinate Break	Element tilt : return				6.6
Coordinate Break	Element tilt				31
Birefringent Out		LiYF4			
Birefringent In		LiYF4	1	1	
Coordinate Break	Element tilt : return				-31
Birefringent Out					
Coordinate Break	Element decenter : return			-17.8	

The design of a single Wollaston in zemax is done by making use of the “Birefringent” surface definition. This particular surface type has a few parameters within its definition, to be utilised for its correct configuration. One of the important parameters is the **mode** i.e. ‘Par 1’. The mode is used to trace the ordinary (mode = 0) and extra-ordinary (mode = 1) ray within the optical system. The two modes are defined using ‘multi-configuration’ editor in zemax. Another important feature to be defined is the value of ‘Y-cosine’ for the 2nd Wollaston. This value will place the optical axis of the down Wollaston at 45° with the up Wollaston. The need for it has been explained before, so as to get the image at 45° & 135° from the down Wollaston.

The material defined for wedge is 'fused silica' and Wollaston is 'LiYF4'. The steps to define a Wollaston in zemax are mentioned below :

1. The pupil diameter is ~ 38 mm for our design. To include two Wollastons with the configuration as shown in Figure 6.4 in the sequential optical chain, the very first step is to 'decenter' the system by around half pupil width in the positive Y-direction (vertical). This part will see half of the beam passing through the pupil plane.
2. After the surface has been decentered, we need to define the wedge surface. Since the entrance surface of the wedge needs to be at an angle, which is not the β_2 angle, we need to determine it. From the geometry, it is visible that the entrance angle is equal to $\beta_1 - \beta_2$. This hence forms the premise for our wedge surface placement with an angle of 3.5° to the X-axis, as defined under 'Tilt about X' parameter. The surface following this tilt is the wedge with the definition of material too in it. Subsequent to it, the tilt in the coordinate plane is reverted back by a pickup surface. The exitance surface of the wedge has to be matched to the entrance surface of the Wollaston. Therefore, another tilt with angle equal to β_1 is defined in zemax. This completes the wedge surface.
3. The wedge placement is done, which now allows us to define the Wollaston surfaces. The next surface starts with defining the entrance face of the Wollaston with an angle of 6.6° to X-axis. This surface is followed by another surface 'Birefringent In' with the material definition as LiYF4. And the surface is reverted back with the entrance face completed.
4. The next is to define the Wollaston angle α . Within the coordinate shift, we define two surfaces before reverting back the coordinate plane here. The surfaces are 'Birefringent Out and In' respectively. This defines the crystal plane of the Wollaston at an angle equal to α i.e. 31° .
5. The last step is to revert back the applied decenter to continue back at optical axis.

This is the designing step followed for one Wollaston of the WeDoWo. The other Wollaston has to follow the same steps but in reverse manner. The first decenter for

it will be below the optical plane by the same amount as for the up Wollaston. This particular part is completed by making use of the ‘multi-configuration’ editor, and define the values for each of these parameters for both the o- and e-ray. The surface tilts & decenters are included within the design using ‘coordinate breaks’. As the YLF material has a low birefringence, the proper image separation requires a large Wollaston angle α . Hence, the size of the WeDoWo component comes to ~ 30 mm. The Table 6.1 mentions the sequential entering of the surfaces for the WeDoWo design for the o-ray (config 1 in Table 6.2), and similarly the multi configuration Table 6.2 modifies the values of few parameters within the surfaces to realise the tracing of other beams for polarization.

Note: Similar steps have been followed with changes in the numbers for defining the different parameters for MgF_2 based WeDoWo.

Table 6.2: The multi configuration editor data used to input the values for all the 4 beams in the polarization design using YLF.

Surface/Parameter	Config 1	Config 2	Config 3	Config 4
Decenter	17.8	17.8	-17.8	-17.8
Tilt 1	-3.7	-3.7	3.7	3.7
Tilt 2	-6.6	-6.6	6.6	6.6
Tilt 3	-6.6	-6.6	6.6	6.6
Mode	0	1	0	1
Tilt 4	31	31	-31	-31
Mode	1	0	1	0
Decenter	-17.8	-17.8	17.8	17.8

6.4 Polarimetric Analysis

6.4.1 Design of Polarisation optics

The layout for the polarimetric mode of the NISP instrument is seen in Figure 6.5. At the location of the pupil area, we have focal plane mask and WeDoWo placed in the 1st and 3rd filter wheel, respectively. The image is formed at the final detector plane. This layout is a combination of all the 4 configurations defined for designing the WeDoWo. The space between the WeDoWo and first camera lens is ~ 25 mm.

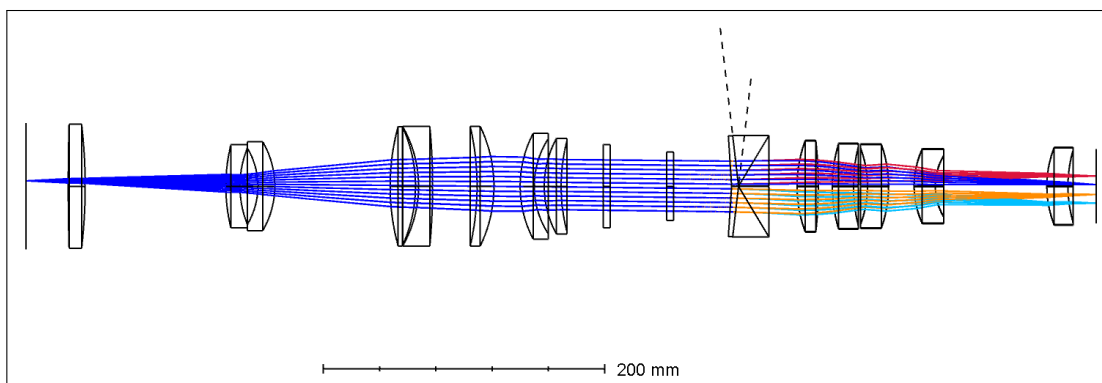


Figure 6.5: Layout of the imaging polarimetric mode of the NISP instrument. The different colors at the image plane are for the 4 angles consisting of two o-rays and e-rays respectively.

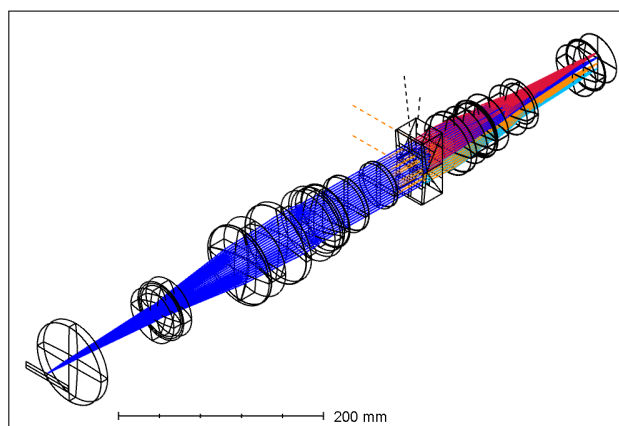


Figure 6.6: An isometric layout of the NISP polarimetric design. The starting is from the left side, where the rectangular aperture seen is the focal plane mask.

6.4.2 Focal plane mask

A focal plane mask is defined at the Cassegrain focus of the telescope. The dimensions of the mask are calculated from the idea of plate scale = 16.6"/mm. Hence, the focal plane mask defined to cover a rectangular FOV of 10' x 1.4', in linear scale is sized as 58.2 mm x 8 mm. The focal plane mask assembly in the instrument is shown in Figure 6.7. Its placement is in the aperture wheel at the Cassegrain focus.

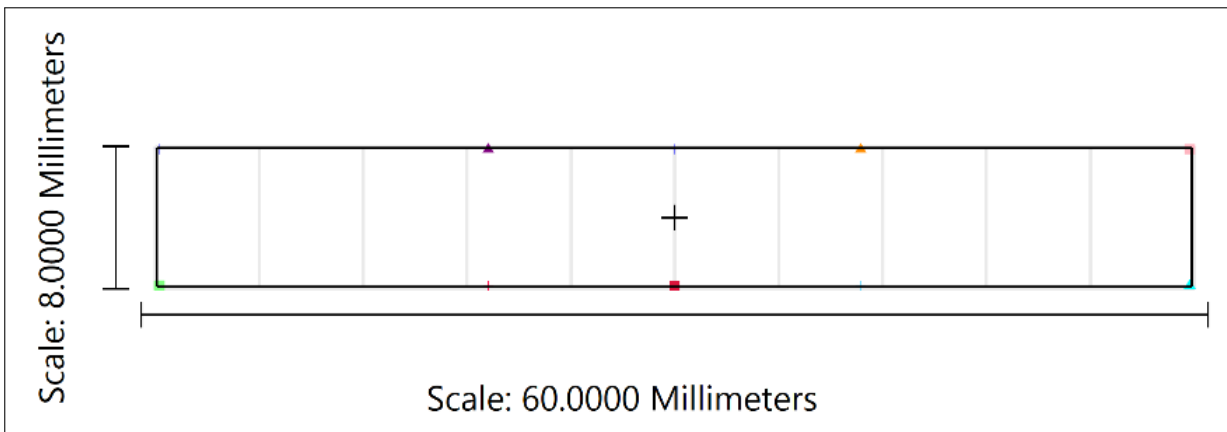


Figure 6.7: The focal plane mask to display 4 non-overlapping images.

6.4.3 Image plane

The imaging mode of the NISP instrument has a FOV of 10' x 10'. Since, imaging polarimetry will employ an extra component to record the intensity variations based upon the angles on those imaging field, we need to ensure an effective use of the full field of the detector. As can be seen from the footprint diagram in Figure 6.8, the full 36.8 mm square area is marked, and the horizontal strips define the images at the various angles of the Wollaston. The FOV in the imaging polarization mode is 10' x 1.4'. As is seen that with only half of the beam utilised from one Wollaston, the vignetting plot shown in Figure 6.9 conveys it for just one Wollaston out of the combination in WeDoWo. The fraction of unvignetted rays is 0.36, denoting the FOV of the Up Wollaston from the double Wollaston system.

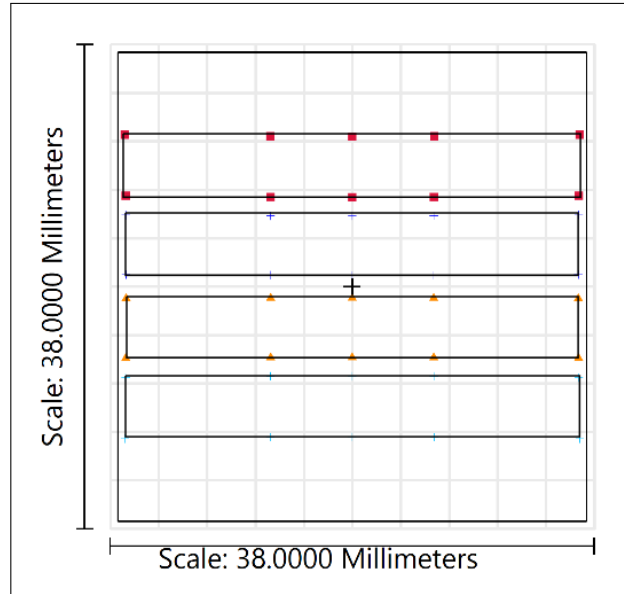


Figure 6.8: The image plane of the NISP imaging polarization mode showcasing the 4 strips as imaged by the system.

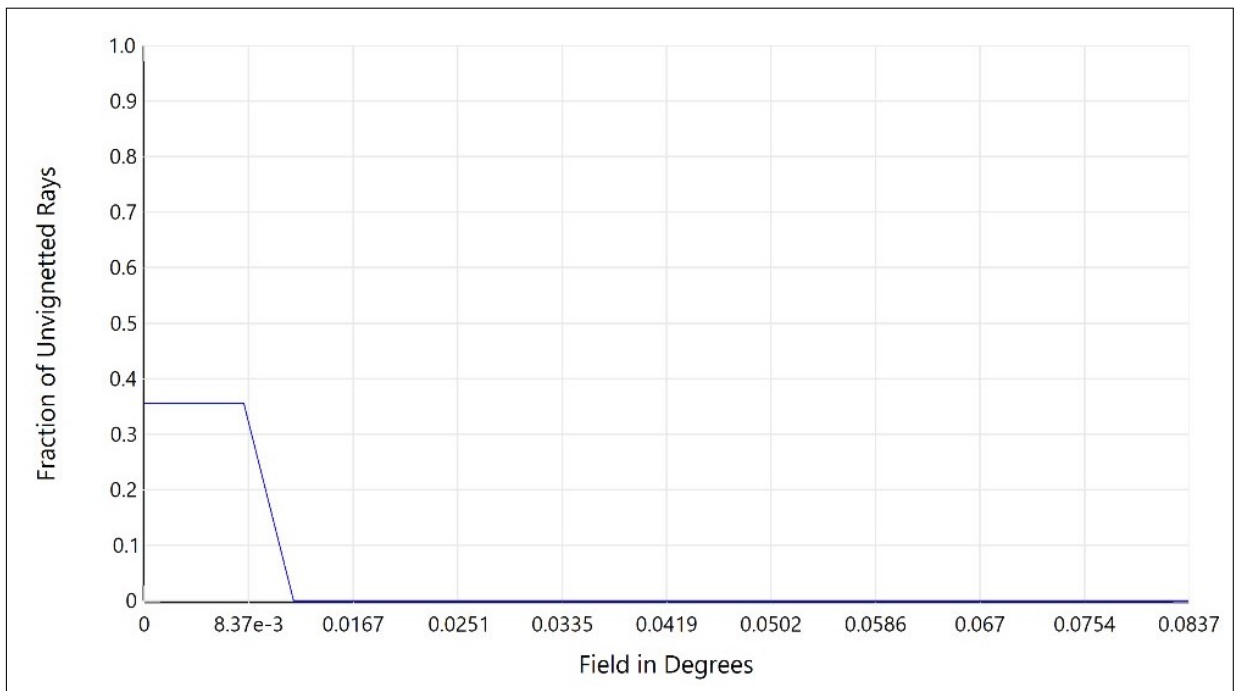


Figure 6.9: Vignetting plot for NISP imaging polarization mode. The plot for the imaging mode is shown in Figure 4.12

6.4.4 Spot diagram

Spot diagrams are important to understand the performance of the optical system designed at the detector plane. This varies depending upon the components placed

at the pupil plane for executing a set of job. In the case of imaging design, we had seen that the spot sizes were achieved well within 1 pixel size. On the employment of Wollaston in the optical chain, there is an addition in the lateral chromatism aberration in the spots formed from it. The spot sizes are therefore, seeing limited with maximum spot radius size $\sim 24 \mu m$ i.e. covering 3 pixels. This lateral chromatism is seen as the different wavelengths being focused at different points on the transverse axis of the final image plane. It is very important to take into account the lateral chromatism in imaging polarimetry to enable the maximum width of the field to be utilised without any image elongation. There were few steps we undertook to reduce the contribution

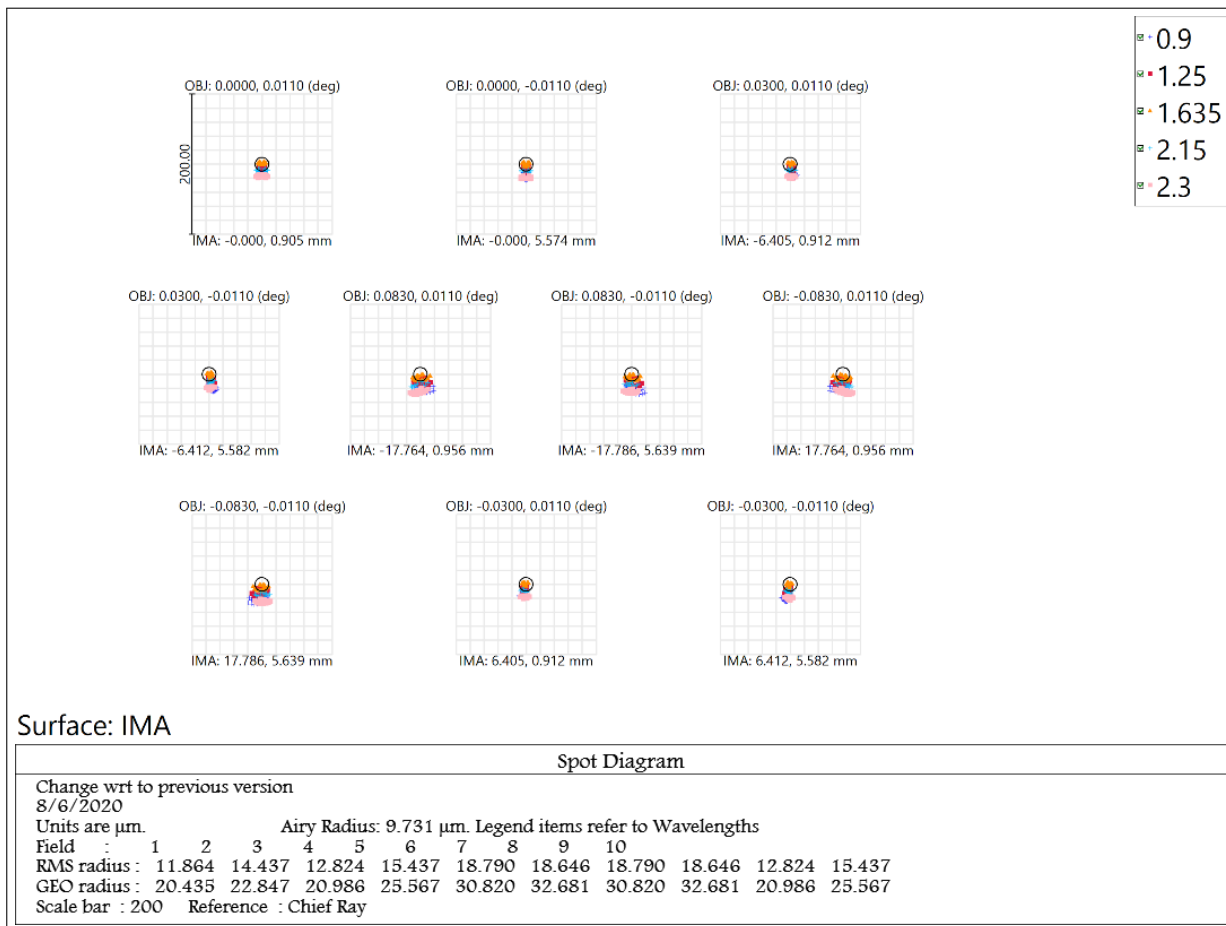


Figure 6.10: Spot diagram of o-ray showing the variation in spot pattern as a function of field angles. The colors denote the wavelengths defined for the system.

of lateral chromatism as seen in our spot diagram in Figure 6.10. To point them as,

1. The birefringence variation of the crystal with wavelength should be low. The materials well suited for this application are MgF2 & LiYF4 (YLF) for the optical

and infrared wavelength bands respectively (Oliva, 1997). The properties of the YLF material are listed in Oliva (1997) as having a low refractive index, $n_o \sim 1.45$. Its thermo-optic coefficient are also small, $\frac{dn_o}{dT} \sim -1 \times 10^{-6}$ and $\frac{dn_e}{dT} \sim -3 \times 10^{-6} \text{ K}^{-1}$. It is also seen from Fig. 6.11 that YLF is twice less chromatic than MgF₂ in the NIR wavebands.

2. To further reduce any presence of lateral chromatism from the design of the WeDoWo, the value of it for the wedge has to be small. Since, YLF is low dispersion material, coupling it with a high dispersion material (fused silica in our case), will form a combination having less chromatism.
3. After the design considerations in choice of material has been done, if small chromatism is still present, then the optimization of the design by changing the wedge angle is utilised. This helps in reducing the effect of lateral chromatism seen in the design spot diagram.

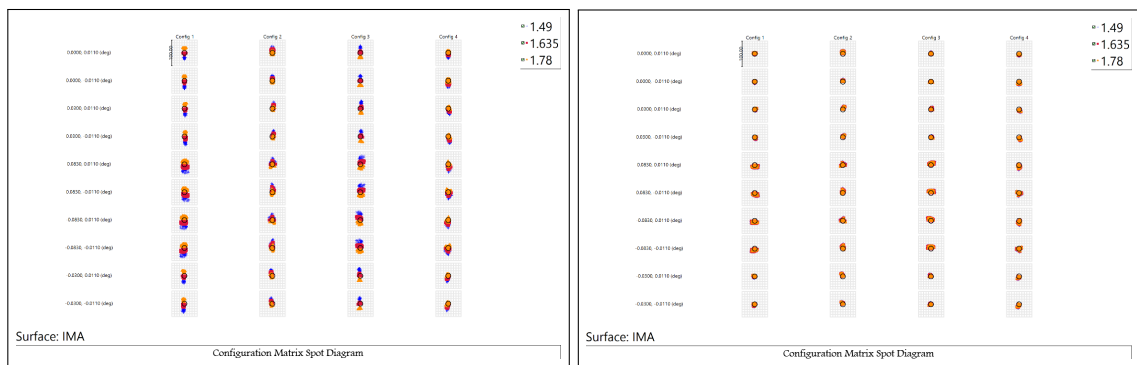


Figure 6.11: Matrix spot diagram for NISP imaging polarimetric mode with MgF₂ (left) & YLF (right) material. It shows a full matrix of individual spots for all the configurations.

The matrix spot diagram demonstrates the spots for all the individual configurations (as columns) defined for the WeDoWo at each field location (as rows). These configurations are for analysing the 2 o-rays and 2 e-rays individually from the combined Wollastons used. It is shown in the Figure 6.11. Its seen that the performance of the o-rays of both the Wollastons have lesser chromatism than present in the e-rays.

6.4.5 Polarization pupil map

The polarization pupil map defines the output orientations for the different input orientations at the polarizer defined by J_x & J_y . For the NISP WeDoWo design, we have made the pupil maps at the image plane for the central field at H band central wavelength. The maps for all the 4 configurations are shown in the Figure 6.12. The inset shows the combinations of input angles to the polarizer. As the 1st Wollaston has its optical axis defined at 0° & 90° for the o-ray & e-ray respectively, the pupil map shows full transmission & zero transmission for the crossed polarization states. The direction of the output polarization for these case shows that our output state is P-polarized, since the output beams are parallel to the input polarization. In the case of 45° & 135° , a mixture of S- & P- states is seen in all the 4 configurations. We can also see the transmission fraction at the image plane from this technique $\sim 1\%$. This is because of the total transmission from the imaging system is 35%. The imaging polarimetry divides it into 4 more beams (due to WeDoWo), hence giving the final transmission $\sim 0.25 \times 35\%$ for each beam of the different configurations. The transmission fraction could be increased by using anti-reflective (AR) coatings on the entrance face of the lenses & other optical components.

6.5 Statistics of polarization measurements

The value of polarization measured for most of the astronomical sources is very small, which makes the presence of noise in it a very important parameter to quote the result with proper accuracy. We know that polarimetry is referred to as a photon-hungry technique. The significance of the measurement depends upon the accumulation of many counts to form a signal. The polarimetric accuracy depends only on the statistical behavior of photons detected. The different sources of noise which lead to uncertainties in polarisation measurements are: Earth's atmosphere, telescope optics, variable sky background, photon noise, telescope tracking errors, detector pixel-to-pixel variations. The major source of noise affecting the polarization result is the photon shot noise. Shot



Figure 6.12: The polarization pupil map for all the 4 configurations of NISP imaging polarization design. The maps are for the central field at $1.635 \mu\text{m}$. The first row defines the 0° input polarization state & the outputs for the 4 combinations from 2 Wollastons. Similarly the 2nd, 3rd & 4th row define the 90° , 45° & 135° input polarization respectively.

noise is dominant in the case when the photon counts are relatively small, which causes the uncertainties due to Poisson distribution to become significant.

The mechanism in which photon shot noise is affecting the determinations of normalized Stokes parameters is dependant on the modulation technique. In one of the papers by Serkowski (1962) it is impressed that due to the complicated statistical properties of p & θ , it will be good if the Stokes parameters are used for their discussions. The determination of Stokes parameters requires intensity determination at a pair of orthogonal polarizations. The smaller the Stokes parameters, the smaller is the difference in intensity between the orthogonal angles, and larger is the photon count required to

quote a value of polarization with statistical significance (Clarke, 2010). In most of the stellar measurements for polarization, a photon count $> 10^6$ is good for an accurate estimation.

A very useful discussion about the statistical behavior of Stokes parameters is provided in Clarke et al. (1983). The major conclusion they arrive at from their discussion in the paper is that the probability function for normalized stokes parameters has a slight deviation from the mean of a perfect normal curve. This deviation in the tail side of a normal curve is defined by the kurtosis coefficient whose value goes to smaller number and approaching that of a perfect normal curve at a high photon count. Taking this into consideration, it is clear that increasing the SNR by accumulation of photon counts will allow for an accurate determination of polarization.

As an estimation for the S/N requirement for a WeDoWo system, the description from ALFOOSC polarimetry¹ is found quite useful. Deriving an understanding from the reference,

Let us consider σ_p to be 1- σ error in the degree of polarization, S/N required to obtain accuracy of σ_p is,

$$S/N_{F_o+F_e} = \frac{\sqrt{2}}{\sigma_p * \sqrt{n}} \quad (6.2)$$

where, $S/N_{F_o+F_e}$ is the signal-to-noise ratio of the combined flux of the combined components.

n is the number of rotations/positions used, which in our case is $n = 4$. Considering the case for low polarizations, F_o equals F_e , and hence the above equation can be modified to refer the signal-to-noise of each of the dual beam component as,

$$S/N = \frac{0.5}{\sigma_p} \quad (6.3)$$

Giving an estimate of the large SNR required for a polarization data as opposed to imaging, if we consider our accuracy to be $\pm 0.3\%$, the $S/N = 167$ is needed.

¹<http://www.not.iac.es/instruments/alfosc/polarimetry/signaltonoise.html>

6.6 Summary

The chapter describes the design of the polarization components of the NISP instrument. The implementation of polarization optics at cryo temperature makes the instrument unique. A wedged double Wollaston (WeDoWo) has been used for the execution of the polarization mode of NISP. Two materials have been explored for the design of WeDoWo, i.e., YLF & MgF_2 , and both match the required performance specifications with the design. The chapter demonstrates the design achievements using a single shot polarimeter and analysis to ensure its successful use.

Chapter 7

Summary & Future Work

7.1 Summary

The PhD study comprises of a combination of observations, scientific analysis & the development of astronomical instrumentation. The study of a dark cloud using imaging polarimetry has been found very promising & involved a lot of re-runs during the analysis procedure. The results from the use of a wire-grid polarizer (WGP) at multiple modulating angles gave us a strong impetus to consider a polarimetric component with simultaneous measurements of the Stokes' parameters which would minimise the contribution of sky variations in the measured values. This resulted in our taking up the design of a WeDoWo based polarization mode as a part of the near-IR imager, spectrometer & polarimeter (NISP). The design process included the basics of optics revisited and lot of iterations over the design process to finalise the NISP optical design. It is a very versatile instrument & the design process has been challenging in the sense that all the multiple functions in the design have been optimized from the beginning & all components are maintained at cryo temperature in a vacuum dewar. Few near-

IR instruments have such capabilities with polarization measurement enabled in cold optics. This work has provided with immense experience in the optical design of multimode instruments.

Specific results from observations and the instrument design with *OpticStudio Zemax* presented in the thesis are summarized below:

1. *Polarization study of dark clouds* : The polarization study of Lynds 1340 has been completed with very interesting results being achieved. We had carried out near infrared observations in the J, H & K_s wavelength bands using the NICSPol instrument. The polarization values for 56, 76 & 33 stars have been reported in the respective bands with Gaia & 2MASS counterparts. The magnetic field strength for the RNO8 region within the L1340 cloud was estimated to be 42 μG .
2. *Imaging design of NISP*: The imaging design of NISP consists of a reimager combination of collimator & camera lenses to focus the incident light at various field positions covering the full FOV on the detector plane. An F/5 camera system is designed for the sampling of 1'' on 3 pixels of the detector. The specifications for the imaging design of NISP achieve the targets set for the instrument. The total length of the instrument is 740 mm.
3. *Spectroscopic design of NISP*: The spectroscopic design uses a 'grism' as the main component to disperse the different wavelength bands. Separate grisms for each of the 4 bands Y, J, H, K_s had been designed using the KRS-5 material in the 1st order with a spectral resolving power of 2150. A slit of length 1.4' & width ~ 1'' is placed in the aperture wheel at the Cassegrain focal plane. A low resolution grism, R ~ 560, has also been designed to enable mixed mode in the instrument.
4. *Polarization design of NISP*: The polarization design uses a WeDoWo component to ensure single shot simultaneous polarization measurements at 4 position angles. A focal plane mask of 10' x 1.4', has been designed to create 4 non-overlapping images corresponding to each of the angles. The accuracy in polarization measurements from the use of WeDoWo will be better than 1%. The design of the WeDoWo component along with its implementation in the instrument is successfully completed.

The Table 7.1 gives a comparison of the specifications targetted for the NISP instrument, and the design achievements using different components designed for enabling the multiple modes.

PARAMETER	TARGET	ACHIEVED
Required spot size at detector	$54\mu m$	$\ll 54\mu m$
FOV	$10' \times 10'$	✓
Encircled Energy	EE80 ~ 2pixels	EE90 ~ 2 pixels
Resolution	2000-3000	~2150
Polarisation	HWP + Wollaston (modulator)	WeDoWo (single-shot)

Figure 7.1: The design goals and achievements for NISP

7.2 Future work

The future work will be to build upon the current work that has already been done in the scientific & instrumentation aspects. The eventual goal is the completion of the instrument and its regular use on the 2.5 m telescope of PRL in the foreseeable future.

Specific ideas are listed below :

1. The optical design for the multiple modes of NISP is complete in one front with full optimization of the design. The second part which will be taken up will be the 'full tolerancing' of the design. This will provide a margin to the opto-mechanical engineer to fabricate the components.
2. A baffle design for the optics will also be carried out to check for the stray light.
3. A slit viewer design is to be added to the optical system, to enable real time guiding of the objects on the slit. This is important for the pointing and tracking of solar system objects for which the off-axis (telescope's built-in) guider cannot be used.
4. A cross-dispersor design is needed in conjunction to the low resolution grism in the spectroscopic optics, to separate the mixed-mode spectrum and also remove higher order components from other wavelength bands.
5. A pupil viewer will be designed for NISP. We have not considered a pupil viewer in the current design since we are restricting ourselves to the K_s band with an upper limit of $2.31\mu\text{m}$. Going up to the edge of the detector sensitivity at $2.5\mu\text{m}$ may require a cold stop at the pupil along with a pupil viewer. This will be taken up if there is enough interest after confirming the observing conditions at the telescope.
6. Optical polarization of dark clouds : EMCCD based polarimeter (EMPOL) is an indigenously built focal plane polarimeter using an EMCCD camera for PRL's 1.2 m telescope. The EMPOL instrument was used in the season during April-June 2019. A wide range of objects including LDN 455, 416, 698, 677, 530 were observed in the optical bands. The analysis & complete scientific interpretation of the optical polarization will be completed. The results will be combined with H band polarization data from GIPS survey (which has already observed these nebulae) to see the trend from optical to near-IR interstellar polarization.
7. As an additional academic exercise with the aim of possible future implementation, I shall work on the zemax design of a collimator+camera combination to increase the FOV of EMPOL with the same set of polarization optics.

References

- Aarthy E., Rai A., Ganesh S., Vadawale S. V., 2019, [Journal of Astronomical Telescopes, Instruments, and Systems](#), 5, 035006 [Cited on pages 14, 15, 16, 23, 57, and 61.]
- Abayaratne C., Wickramarathna A., Rodrigo D., Mannathunga K., 2016, [Journal of the National Science Foundation of Sri Lanka](#), 44, 95 [Cited on pages xv and 2.]
- Anandarao B., Richardson E. H., Chakraborty A., Epps H., 2008, in McLean I. S., Casali M. M., eds, Vol. 7014, Ground-based and Airborne Instrumentation for Astronomy II. SPIE, pp 1053 – 1060, doi:10.1117/12.788246, <https://doi.org/10.1117/12.788246> [Cited on pages 14, 15, and 16.]
- Andersen T. B., 2015, [Appl. Opt.](#), 54, 7525 [Cited on page 100.]
- Andersson B. G., Potter S. B., 2007, [ApJ](#), 665, 369 [Cited on pages 9 and 12.]
- Andersson B.-G., Lazarian A., Vaillancourt J. E., 2015, [Annual Review of Astronomy and Astrophysics](#), 53, 501 [Cited on page 8.]
- Bagnulo S., et al., 2017, [Astronomy & Astrophysics](#), 608, A146 [Cited on page 14.]
- Bailer-Jones C. A. L., Rybizki J., Fouesneau M., Mantelet G., Andrae R., 2018, [AJ](#), 156, 58 [Cited on pages 26 and 28.]
- Barnard E. E., 1927, Catalogue of 349 dark objects in the sky [Cited on page 21.]
- Barnett S. J., 1915, [Physical Review](#), 6, 239 [Cited on page 9.]
- Baug T., et al., 2018, [Journal of Astronomical Instrumentation](#), 07, 1850003 [Cited on page 16.]
- Chandrasekhar S., 1946, [ApJ](#), 103, 351 [Cited on page 2.]
- Chandrasekhar S., Fermi E., 1953, [ApJ](#), 118, 113 [Cited on pages 10, 15, and 41.]
- Clarke D., 2010, Stellar Polarimetry [Cited on pages 131, 133, 135, and 152.]

Clarke D., Stewart B. G., Schwarz H. E., Brooks A., 1983, *A&A* , [126, 260](#) [Cited on page [152](#).]

Clemens D. P., Pinnick A. F., Pavel M. D., Taylor B. W., 2012a, *ApJS*, [200, 19](#) [Cited on page [14](#).]

Clemens D. P., Pinnick A. F., Pavel M. D., 2012b, *ApJS*, [200, 20](#) [Cited on page [14](#).]

Clemens D. P., Pavel M. D., Cashman L. R., 2012c, *ApJS*, [200, 21](#) [Cited on page [14](#).]

Clemens D. P., et al., 2020a, arXiv e-prints, p. [arXiv:2006.15203](#) [Cited on pages [14](#) and [27](#).]

Clemens D. P., et al., 2020b, *ApJS*, [249, 23](#) [Cited on page [14](#).]

Cohen M., 1980, *AJ*, [85, 29](#) [Cited on page [22](#).]

Covino S., et al., 2014, *Astronomische Nachrichten*, [335, 117](#) [Cited on pages [137](#) and [140](#).]

Cutri R. M., et al., 2003, VizieR Online Data Catalog, p. [II/246](#) [Cited on page [28](#).]

Davis Leverett J., Greenstein J. L., 1951, *ApJ*, [114, 206](#) [Cited on pages [9, 12](#), and [15](#).]

Deen C. P., Gully-Santiago M., Wang W., Pozderac J., Mar D. J., Jaffe D. T., 2017, *PASP*, [129, 065004](#) [Cited on pages [xviii, 116, 117, 119](#), and [120](#).]

Deshpande M. R., Joshi V. C., Kulshrestha A. K., Banshidhar Vadher N. M., Mazumdar H. S., Pradhan S. N., Shah C. R., 1985, *Bulletin of the Astronomical Society of India*, [13, 157](#) [Cited on page [16](#).]

Dolginov A. Z., Mitrofanov I. G., 1976, *Ap&SS*, [43, 291](#) [Cited on page [9](#).]

Draine B. T., Lazarian A., 1998, *ApJ*, [508, 157](#) [Cited on page [8](#).]

Eswaraiah C., et al., 2019, *ApJ*, [875, 64](#) [Cited on pages [8, 12](#), and [38](#).]

Ganesh S., et al., 2020, in Society of Photo-Optical Instrumentation Engineers (SPIE) Conference Series. p. 114479E ([arXiv:2012.08768](#)), [doi:10.1117/12.2560949](#) [Cited on page [16](#).]

- Geary J., 2002, Introduction to Lens Design: With Practical ZEMAX Examples. Willmann-Bell, <https://books.google.co.in/books?id=dPWAPQAACAAJ> [Cited on page 73.]
- Gold T., 1952a, *MNRAS*, **112**, 215 [Cited on page 9.]
- Gold T., 1952b, *Nature*, **169**, 322 [Cited on page 9.]
- Gorosabel J., García Muñoz A., Sánchez-Lavega A., Hueso R., Pérez Hoyos S., 2014, in European Planetary Science Congress. pp EPSC2014–300 [Cited on page 137.]
- Gupta R., Burse M., Das H. K., Kohok A., Ramaprakash A. N., Engineer S., Tandon S. N., 2002, *Bulletin of the Astronomical Society of India*, **30**, 785 [Cited on page 16.]
- Hall J. S., 1958, *Publications of the U.S. Naval Observatory Second Series*, **17**, 275 [Cited on page 3.]
- Hatano H., et al., 2013, *AJ*, **145**, 105 [Cited on pages 8 and 27.]
- Helhel S., Khamitov I., Kahya G., Bayar C., Kaynar S., Gumerov R., 2015, *Experimental Astronomy*, **39**, 595 [Cited on page 137.]
- Hiltner W. A., 1951, *ApJ*, **114**, 241 [Cited on page 3.]
- Hiltner W. A., 1954, *ApJ*, **120**, 454 [Cited on page 3.]
- Jones T. J., 1989, *ApJ*, **346**, 728 [Cited on pages 12 and 27.]
- Jones T. J., 2011, in Bastien P., Manset N., Clemens D. P., St-Louis N., eds, *Astronomical Society of the Pacific Conference Series Vol. 449, Astronomical Polarimetry 2008: Science from Small to Large Telescopes*. p. 3 [Cited on page 11.]
- Joshi U. C., Kulkarni P. V., Bhatt H. C., Kulshrestha A. K., Deshpande M. R., 1985, *Monthly Notices of the Royal Astronomical Society*, **215**, 275 [Cited on page 12.]
- Kandori R., et al., 2006, in *Society of Photo-Optical Instrumentation Engineers (SPIE) Conference Series*. p. 626951, [doi:10.1117/12.670967](https://doi.org/10.1117/12.670967) [Cited on page 14.]
- Kawabata K. S., et al., 2003, in Iye M., Moorwood A. F. M., eds, *Society of Photo-Optical Instrumentation Engineers (SPIE) Conference Series Vol. 4841, Instrument*

- Design and Performance for Optical/Infrared Ground-based Telescopes. pp 1219–1228, [doi:10.1117/12.461923](https://doi.org/10.1117/12.461923) [Cited on page 137.]
- Kawabata K. S., et al., 2010, in Kawai N., Nagataki S., eds, American Institute of Physics Conference Series Vol. 1279, American Institute of Physics Conference Series. pp 355–356, [doi:10.1063/1.3509309](https://doi.org/10.1063/1.3509309) [Cited on page 137.]
- Kun M., et al., 1994, *A&A*, **292**, 249 [Cited on pages 12 and 42.]
- Kun M., Wolf-Chase G., Moór A., Apai D., Balog Z., O’Linger-Luscusk J., Moriarty-Schieven G. H., 2016a, *ApJS*, **224**, 22 [Cited on pages xv, 12, 13, 33, 34, 39, and 40.]
- Kun M., Moór A., Szegedi-Elek E., Reipurth B., 2016b, *ApJ*, **822**, 79 [Cited on pages 12, 13, and 22.]
- Kwon J., Tamura M., Hough J. H., Nagata T., Kusakabe N., Saito H., 2016, *The Astrophysical Journal*, **824**, 95 [Cited on pages 8, 12, and 42.]
- Larionov G. M., Val’tts I. E., Winnberg A., Johansson L. E., Booth R. S., Golubev V. V., 1999, *Astronomy and Astrophysics Supplement Series*, **139**, 257 [Cited on page 22.]
- Lazarian A., 2007, *J. Quant. Spec. Radiat. Transf.*, **106**, 225 [Cited on page 12.]
- Lundmark K., 1926, *Arkiv for Matematik, Astronomi och Fysik*, **19**, 1 [Cited on page 21.]
- Lynds B. T., 1962, *ApJS*, **7**, 1 [Cited on pages 12 and 21.]
- Mar D. J., Marsh J. P., Deen C. P., Ling H., Choo H., Jaffe D. T., 2009, *Appl. Opt.*, **48**, 1016 [Cited on pages 116, 121, 123, and 124.]
- Martin P. G., Clayton G. C., Wolff M. J., 1999, *ApJ*, **510**, 905 [Cited on page 8.]
- Mathewson D. S., Ford V. L., 1970, *MmRAS*, **74**, 139 [Cited on pages xv and 3.]
- Messinger D. W., Whittet D. C. B., Roberge W. G., 1997, *ApJ*, **487**, 314 [Cited on page 8.]
- Mondal S., Yadav R., Singh M. B., 2009. [Cited on page 119.]
- Myers P. C., Goodman A. A., 1991, *ApJ*, **373**, 509 [Cited on page 12.]

- Ninan J. P., et al., 2014, [Journal of Astronomical Instrumentation](#), **3**, 1450006 [Cited on pages 14 and 16.]
- Oliva E., 1997, [A&AS](#) , **123**, 589 [Cited on pages xix, 17, 137, 138, 139, and 149.]
- Omar A., Kumar T. S., Krishna Reddy B., Pant J., Mahto M., 2019, arXiv e-prints, p. [arXiv:1902.05857](#) [Cited on page 16.]
- Ostriker E. C., Stone J. M., Gammie C. F., 2001, [ApJ](#), **546**, 980 [Cited on pages 10, 42, and 43.]
- Pancharatnam S., 1955, [Proceedings of the Indian Academy of Sciences - Section A](#), **41**, 130 [Cited on page 11.]
- Papoular R., 2018, [MNRAS](#) , **479**, 1685 [Cited on page 8.]
- Patat F., Romaniello M., 2006, [PASP](#), **118**, 146 [Cited on page 137.]
- Pernechele C., Giro E., Fantinel D., 2003, in Fineschi S., ed., Society of Photo-Optical Instrumentation Engineers (SPIE) Conference Series Vol. 4843, Polarimetry in Astronomy. pp 156–163, [doi:10.1117/12.466129](#) [Cited on page 137.]
- Ramaprakash A. N., Gupta R., Sen A. K., Tandon S. N., 1998, [A&AS](#) , **128**, 369 [Cited on page 16.]
- Rautela B. S., Joshi G. C., Pandey J. C., 2004, Bulletin of the Astronomical Society of India, **32**, 159 [Cited on page 16.]
- Schwartz K., Burge J., 2012, Field Guide to Optomechanical Design and Analysis. SPIE, [doi:10.1117/3.934930](#), <https://doi.org/10.1117/3.934930> [Cited on page 111.]
- Serkowski K., Mathewson D. S., Ford V. L., 1975, [ApJ](#), **196**, 261 [Cited on pages 3 and 7.]
- Simmons J. F. L., Stewart B. G., 1985, [A&A](#) , **142**, 100 [Cited on page 27.]
- Snik F., Keller C. U., 2013, Astronomical Polarimetry: Polarized Views of Stars and Planets. Springer Netherlands, Dordrecht, pp 175–221, [doi:10.1007/978-94-007-5618-2_4](#) [Cited on page 132.]

- Srivastava M. K., Kumar V., Dixit V., Patel A., Jangra M., Rajpurohit A. S., Mathur S. N., 2021, [Experimental Astronomy](#), [Cited on page 16.]
- Stetson P. B., 1987, [PASP](#), **99**, 191 [Cited on page 24.]
- Struve O., Zeberg V., 1962, *Astronomy of the 20th century* [Cited on page 2.]
- Tassis K., et al., 2018, arXiv e-prints, p. [arXiv:1810.05652](#) [Cited on page 14.]
- Wang J.-W., Lai S.-P., Eswaraiah C., Clemens D. P., Chen W.-P., Pandey A. K., 2017, [ApJ](#), **849**, 157 [Cited on page 8.]
- Watanabe M., et al., 2005, [PASP](#), **117**, 870 [Cited on page 14.]
- Waxler R. M., Cleek G., 1973, [Journal of Research of the National Bureau of Standards Section A: Physics and Chemistry](#), **77A**, 755 [Cited on page 72.]
- Whittet D. C. B., 1992, *Dust in the galactic environment* [Cited on pages 4, 6, and 7.]
- Whittet D. C. B., 2005, in Adamson A., Aspin C., Davis C., Fujiyoshi T., eds, *Astronomical Society of the Pacific Conference Series Vol. 343, Astronomical Polarimetry: Current Status and Future Directions*. p. 321 [Cited on page 37.]
- Whittet D. C. B., Martin P. G., Hough J. H., Rouse M. F., Bailey J. A., Axon D. J., 1992, [ApJ](#), **386**, 562 [Cited on page 8.]
- Wiersema K., Higgins A. B., Covino S., Starling R. L. C., 2018, [PASA](#), **35**, e012 [Cited on page 14.]
- Willey R. L., 1992, [PASP](#), **104**, 285 [Cited on page 93.]
- Wilking B. A., Lebofsky M. J., Rieke G. H., Kemp J. C., 1979, [AJ](#), **84**, 199 [Cited on pages 7 and 12.]
- Wolf E., 2003, [Physics Letters A](#), **312**, 263 [Cited on page 132.]
- Wright E. L., et al., 2010, [AJ](#), **140**, 1868 [Cited on page 28.]